ION BOMBARDMENT EFFECTS ON MATERIAL COMPOSITIONS
— PREFERENTIAL SPUTTERING AND ATOMIC MIXING

Thesis by

Zong-Long Liau

In Partial Fulfillment of the Requirements

for the Degree of

Doctor of Philosophy

California Institute of Technology

Pasadena, California

1979

(Submitted November 6, 1978)

ACKNOWLEDGMENTS

It gives me great pleasure to express my appreciation and gratitude to my research advisor Prof. J. W. Mayer and to Prof. M.-A. Nicolet, Dr. W. L. Brown, Dr. S. S. Lau and Dr. J. M. Poate for their guidance, interest, discussions and encouragement, which have made my five and a half years of graduate study a much enjoyed and unforgettable experience. For the last year, I appreciate the collaboration with my colleague B. Y. Tsaur.

I am indebted to all my colleagues with whom I have collaborated and have learned much from: W. M. Augustyniak, S. U. Campisano, C. Canali, G. E. Chapman, W. K. Chu, C. J. Doherty, C. A. Evans, Jr., R. Gorris, J. K. Hirvonen, R. Homer, J. J. Mallory, S. E. Matteson, C. M. Melliar-Smith, G. L. Miller, D. M. Pepper, R. Pretorius, J. W. Rodgers, N. Schwartz, D. M. Scott, T. T. Sheng and W. F. Tseng. The excellent secretarial works of M. Parks, C. Norris, E. Nitchie and V. Snell are very much appreciated. Besides scientific work, I very much enjoyed the friendship from all of them and the surrounding people.

The financial supports of the California Institute of Technology, Bell Laboratories, National Science Foundation and the Office of Naval Research are gratefully acknowledged. I would also like to thank Bell Laboratories for their generosity of allowing my access to their technical staff and research facilities.

Finally, I wish to thank all members of my family for their spiritual support and patience.

ABSTRACT

This thesis reports a study of the effects of ion bombardment on material composition and their implications in material modification and analysis. First, composition changes in binary alloys and compounds as a result of rare-gas sputtering were observed by using Rutherford backscattering techniques. The heavier components were generally found to become enriched in a surface layer whose thickness corresponded to the ion range. After an amount of material comparable to this thickness had been sputter-removed, the surface layer reached a steady-state. The steady-state surface composition was independent of the mass and energy of the sputtering ion. (Chapters 2 and 3)

The results were interpreted in terms of a preferential sputtering, which generated enrichment of the heavy species at surface, in combination with an ion-induced atomic mixing effect, which propagated the composition change over a depth comparable to the ion range. A model based on this interpretation seemed to combine all experimental results into a consistent picture. (Chapter 4)

The model was then extended to study the phenomena of high-dose ion implantation. The idea of preferential sputtering was used to predict the limits of compositions achievable by implanting ion species A into material B,

or by implanting A^+ into material AB. The formation kinetics of the implanted surface layer was determined by both sputtering and atomic mixing effects. The model yielded results in good agreement with preliminary experimental results. (Chapter 5)

One of the important implications of sputter-induced surface layer composition changes has been their effects on the use of sputtering in surface-cleaning and in depth-profiling techniques. In this respect, we also studied the effect of atomic mixing and preferential sputtering on the evolution of very thin surface layers during sputter-etching. We observed that, for low ion doses, the atomic mixing effect first produced a uniformly alloyed surface layer with a thickness comparable to the ion range. Then, during the successive steps of sputter-etching, the surface layer maintained a constant thickness, but with a decreasing alloy (or impurity) concentration. Again, the previously developed model was extended for the present case. It also combined the results into a consistent picture. Based on these studies, we then extended the model further to predict the effect of atomic mixing and preferential sputtering on the depth-profiling techniques. A simple equation was obtained, which related the "apparent" depth profiles to the true ones. (Chapter 6)

Finally, the effect of atomic mixing has been studied

in the cases where the ion range penetrated through the interface between a surface metal film and an underlying Si-substrate. Silicide formation at the interface was observed for ion doses $\lesssim 10^{14}cm^{-2}$. For higher doses, more Si-atoms were incorporated into the surface layer and the system appeared to be amorphized. After being thermally annealed, the samples showed formation of metastable phases which had not been reported previously. The present results suggest that the ion-induced atomic mixing effect has the potential of producing thin-film materials with any desirable compositions or with compositions and structures unachievable by conventional metallurgical means. (Chapter 7)

TABLE OF CONTENTS

ACKNOWLEDGMENTS ii

ABSTRACT iv

Chapter 1: INTRODUCTION 1

1.1 An Overview 1

1.2 Background on Sputtering 4

1.3 Background on High-Dose Ion Implantation 8

1.4 Other Research Topics 10

1.4.1 Solid-Phase Epitaxial Growth of Si 10

1.4.2 Laser Annealing 14

References 19

Chapter 2: SURFACE-LAYER COMPOSITION CHANGES IN SPUTTERED ALLOYS AND COMPOUNDS 23

2.1 Introduction 23

2.2 Experimental Procedures 23

2.3 Results 27

2.4 Interpretations and Implications 33

References 36

Chapter 3: SPUTTERING OF PtSi 38

3.1 Introduction 38

3.2 Depth Profiles of the Sputter-Induced Pt-Enrichment 39

3.3 Yields of Pt and Si 50

3.4 Observation of Argon Bubble Formation 57

References 66

Chapter 4: PHENOMENOLOGICAL MODEL OF ALLOY SPUTTERING 67

4.1 The Simple Model 67

4.2 Calculation of Composition Profiles 75

4.2.1 Formulation 75

4.2.2 Solutions 80

4.2.3 Discussions 89

References 93

Chapter 5: HIGH-DOSE ION IMPLANTATION 94

5.1 Introduction 94

5.2 Maximum Attainable Concentrations 94

5.3 Evolution of the Implanted Concentration 98

5.4 Examples 103

5.5 Prediction of Steady-State Concentration 108

5.6 Other Effects Which Influence High-Dose Ion Implantation 114

5.7 Conclusion 116

References 117

Chapter 6: EVOLUTION OF SURFACE LAYERS DURING SPUTTER-ETCHING 119

6.1 Introduction 119

6.2 Experimental Procedures 121

6.3 Results 122

6.4 The Simple Model 126

6.5 Discussions 129

6.6 Influence of Atomic Mixing and Preferential Sputtering on Depth-Profiling Techniques 132

References 139

Chapter 7: FURTHER EXPERIMENTS AND CONCLUSION 141

7.1 Introduction 141

7.2 Ion-Induced Silicide Formation 141

7.3 Depth-Dependence of Ion-Induced Atomic Mixing 146

7.4 Gas Bubble Formation at Interfaces 147

7.5 Formation of Metastable Phases Using Ion Implantation and Post Thermal Annealing 148

7.6 Conclusion 150

References 152

Appendix A: DERIVATION OF THE EQUATION FOR g(t) 153

Appendix B: SOLUTION OF EQ.(4.20) FOR g(t) 155

Chapter 1
INTRODUCTION

1.1 An Overview

In this work, we have studied effects of heavy-ion bombardment on material compositions. Motivated by the problem of sputtering-induced surface composition changes, which is interesting in understanding alloy sputtering and is also important in many applications of sputtering, we started out by measuring the surface-layer compositions in various alloys and compounds after being sputtered by rare-gas ions. The results turned out to be rather fruitful. We not only found that the preferential sputtering was a general phenomenon, but also observed that the intermixing of atomic species due to the atomic collisions (triggered by the incident ions) was significant. A model was developed to account for the formation kinetics of the altered surface layers. We then explored the effect of atomic mixing and preferential sputtering in other related experiments such as in high-dose ion implantation and in sputter-depth profiling techniques. The alloy sputtering model was generalized and yielded good agreements with these experiments. Finally, we investigated the possibility of using ion beams to mix thin-film structures to produce alloy or compound layers. We found that the ion bombardment was able not only to mix thin-film systems to desirable compositions,

but also to produce special materials which had not been achieved by conventional metallurgical means.

Part of this work has already been written up as papers which have been or will be published in technical journals:

1. "Surface Layer Composition Changes in Sputtered Alloys and Compounds", Z. L. Liau, W. L. Brown, R. Homer and J. M. Poate, Appl. Phys. Lett. 30, 626 (1977).
2. "Sputtering of PtSi", Z. L. Liau, J. W. Mayer, W. L. Brown and J. M. Poate, J. Appl. Phys. 49, 5295 (1978) .
3. "Surface Layer Composition Changes in Sputtered Thin-Film Alloys and Compounds", Z. L. Liau, in Thin-Film Phenomena - Interfaces and Interactions, J. E. E. Baglin and J. M. Poate, eds., (Electrochem. Soc., Princeton, New Jersey 1978) p. 361.
4. "Argon Bubble Formation in the Sputtering of PtSi", Z. L. Liau and T. T. Sheng, Appl. Phys. Lett. 32, 716 (1978).
5. "The Use of Novel PtSi Thin-Film Structures in Preferential Sputtering Measurements", Z. L. Liau, C. J. Doherty, C. M. Melliar-Smith and J. M. Poate, Thin Solid Films (in press).
6. "Structural and Compositional Changes in Ion-Bombarded Ta_2O_5", D. K. Murti, R. Kelly, Z. L. Liau and J. M. Poate (in preparation) .

7. "Limits of Composition Achievable by Ion Implantation", Z. L. Liau and J. W. Mayer, J. Vac. Sci. Technol. Sept-Oct. (1978).

8. "Ion Bombardment Effects on Material Compositions", Z. L. Liau and J. W. Mayer, in Treatise on Materials Science and Technology - Ion Implantation, J. K. Hirvonen ed., (Academic Press, New York 1979) Chapter 2.

9. "Sputtering Limitations for High-Dose Implantations", J. K. Hirvonen, J. M. Poate, Z. L. Liau and J. W. Mayer, paper presented at the International Conference on Ion Beam Modification of Materials, Budapest, Hungary, September, 1978.

10. "Effect of Ion-Induced Atomic Mixing on Sputter-Etching", Z. L. Liau, B. Y. Tsaur and J. W. Mayer (will be submitted to J. Appl. Phys.).

11. "Ion-Induced Silicide Formation", B. Y. Tsaur, Z. L. Liau and J. W. Mayer (submitted to Appl. Phys. Lett.).

12. "Bubble Formation in the Rare-Gas Implanted Metal/Si Systems", B. Y. Tsaur, Z. L. Liau, J. W. Mayer and T. T. Sheng (Submitted to J. Appl. Phys.) .

13. "Formation of New Metastable Phases Using Ion Implantation and Post Thermal Annealing in Metal/Si Systems", B. Y. Tsaur, Z. L. Liau and J. W. Mayer (in preparation).

14. "Depth Profiles of Ion-Induced Atomic Mixing", B. Y. Tsaur, G. E. Chapman, Z. L. Liau and J. W. Mayer (in preparation).

1.2 Background on Sputtering

Sputtering is the removal of material from a target due to bombardment of energetic particles[1-5]. For example, an Ar^+ ion of 60 keV incident normally on a Cu-sample can sputter off ∿ 7 Cu-atoms. There have been extensive measurements on the sputtering of elemental materials. Generally speaking, heavier ions or heavier target materials give higher sputtering yields. Binding energies also play a role and, in general, the sputtering yield is inversely proportional to the binding energy.

The generally accepted theory[4] which explains most sputtering phenomena in elemental materials is based on the collision cascade picture: The incident ion initiates collisions in a volume (the collision cascade) surrounding the ion track. The energy of the incident ion is shared among those atoms within that volume and then dissipated. Because energy is shared among a large number of atoms, only those collisions which take place near the surface of the material are directly effective in knocking atoms out of the material. In other words, the majority of sputtered atoms emerge only from the first few atomic layers. The more collisions taking place in the near surface region, the higher the sputtering yield will be. Therefore, sputtering yield is proportional to the nuclear stopping power of the incident ion in the near surface region.

The main features remain the same for composite materials such as a binary alloy. But, there are additional complications due to the fact that there are two kinds of atoms in the material. The two species may not be sputtered at an equal rate because of differences in energy sharing (in the collision cascade), ejection probabilities or binding energies. Indeed preferential sputtering of one species over the other has been observed in many alloys and compounds[6-20].

With keV gas ions for bombardment, sputtering is now being widely used in solid-state science and technology for *in situ* surface cleaning, material sectioning and thin-film depositions[3]. The sputtering phenomenon is also important in high-dose ion implantations; it eventually sets a limit to the achievable implanted concentration.

The sputter-induced composition change in compounds and alloys is interesting not only because of its importance in the applications of sputtering, but also because of new insights into atomic collisions and interdiffusion in composite materials[3, 21-23].

To elucidate the underlying mechanisms, it is desirable to know the surface and near surface composition under various sputtering conditions. With Auger electron spectroscopy numerous investigators have consistently found Ni-enrichment in Ar^+-sputtered Cu-Ni alloys[8-10]. The Ni-Cu concentration ratio increased by a factor of $\sim$ 1.7. The

thickness of the Ni-enriched surface layer was estimated to be ∿ 30 Å for 2 keV Ar^+ sputtering. Other techniques such as electron diffraction and low energy ion scattering spectroscopy have also been used to study the composition changes in sputtered oxides and alloys. However, it is quite difficult to obtain quantitative informations using these techniques.

Theories and models have been developed by several authors to deal with the mechanism of the composition changes and the formation kinetics of the surface layers[21-23]. More quantitative measurements on surface compositions and composition depth profiles are clearly needed to test these theories.

More recently, the sputter-induced surface layer composition changes have been observed by using Rutherford backscattering techniques[12,13]. Figure 1.1 shows the first observation of this kind[13]. The PtSi sample becomes Pt-enriched in a surface layer of ∿ 200 Å thick, as a result of 20 keV Ar^+ sputtering. This observation is interesting because Rutherford backscattering is a technique for direct measurement of material compositions and is capable of providing quantitative information .

In the present work, we concentrate on using the backscattering techniques for studying the sputter-induced composition changes in various materials[14,15] as well as

the formation kinetics of the altered surface layer [16,17]. We also emphasize the implications of these results, such as in sputter-depth-profiling techniques [18] and in high-dose ion implantation for material modifications [19].

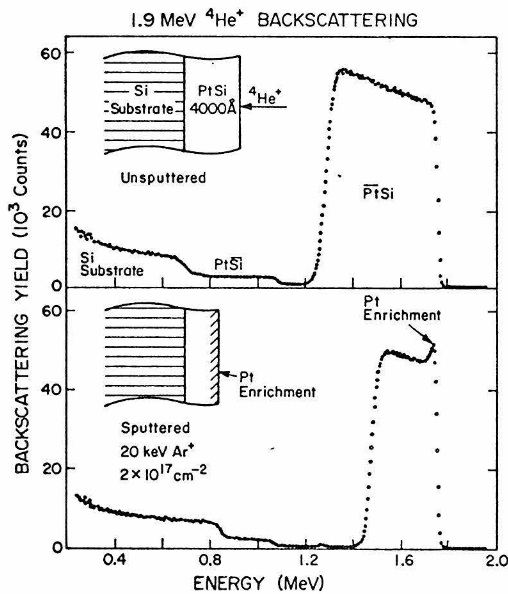

Fig. 1.1 Rutherford backscattering spectra of a PtSi film before and after being sputtered by 20 keV Ar^+.

1.3 Background on High-Dose Ion Implantation

As a microscopically violent and non-equilibrium process, ion-implantation has the capability of producing materials with compositions and structures unattainable by conventional metallurgical means. Therefore, in addition to semiconductor device fabrication , there is a growing interest in using ion-implantation as a potential method of producing materials with interesting new physical properties [24,25].

The use of ion-implantation for metallurgical purposes calls for implanted concentrations of a few atomic %. This requires ion doses around 10^{17} ions per cm^2. At such high doses, sputtering, atomic mixing and chemical effects will become important in determining the states of the implanted materials. First of all, with a common sputtering yield, say 3, a thickness comparable to the ion range will have been sputter-eroded by the time a dose of $\sim 10^{17}$ ions per cm^2 is implanted. Thus, sputtering will not only affect the implanted profile, but also limit the amount of impurities that can be implanted into the material. Secondly, since a monolayer in the solid surface contains $\sim 10^{15}$ atoms per cm^2, each average atom in the implanted layer will have been directly passed by an incident ion at least 100 times and the total number of displacements of each atom will be perhaps two orders of magnitude more.

Therefore, atomic mixing in the implanted layer will be very significant. Furthermore, the introduction of a few atomic % of a foreign species in the material sometimes represents a strong chemical driving force. With the assistance of ion-induced atomic mixing, the chemical driving force can result in compound (or phase) and precipitate formation.

The fields of ion bombardment and sputtering extend back over one hundred years. There are books[1,2] and review articles[3,5] covering the topics. The fact that the ultimate limit to the concentration is set by sputtering was discussed in 1962[26] and since then it has been established that there is a saturation level to the number/ cm^2 of ions that can be introduced in a target[27-36]. In this work we emphasize the role of the preferential sputtering of light elements from a target and show how this effect alters the concentration limit. We also place emphasis on atomic mixing initiated in the collision cascade around the track of the bombarding ion[19].

1.4 Other Research Topics

This section is a digression from the main stream of this thesis. For a more complete record of my graduate research, I would like to briefly mention in this section the work which I have participated in but will not be reported in detail in the rest of this thesis.

1.4.1 Solid-Phase Epitaxial Growth of Si

The first research topic was the solid-phase epitaxial growth (SPEG) of silicon, which was motivated by the technological significance of being able to grow very thin single-crystal semiconductor layers using a solid-phase process at relatively low temperatures. Previous workers have demonstrated the possibility of the SPEG of Si and Ge at ~500°C using metal layers as growth media [37]. However, difficulties were experienced in getting a continuous epitaxial film for Si, probably due to the fact that the Si-substrate surface always has some native oxide which should be removed by some suitable etching technique. Therefore, we decided to use a silicide-forming metal layer (to first create a clean interface) as the growth medium.

Samples consisting of a Pd-layer (~1000 Å) sandwiched between an underlying Si single-crystal substrate and a surface layer of amorphous Si ($\lesssim$1 μm) were prepared by vacuum evaporations. After being annealed at ~300°C, the Pd-layer reacted with Si on both sides to form a layer of Pd_2Si [38]. The SPEG phenomena (i.e., the growth

of the underlying single crystal Si at the expense of the surface amorphous layer) were observed after annealing between ~430°C and 550°C. We then investigated the kinetics of the growth process, the crystalline qualities of the epitaxial layers and the possibility of doping these layers to become electrically active.

With Rutherford backscattering techniques and scanning electron microscopy, we found that the growth of the epi-layer started with nucleation of islands on the substrate. The islands first grew to heights comparable to the thickness of the original Pd-silicide layer, then grew laterally and joined each other to form a uniform layer, whose thickness was nearly equal to the thickness of the original Pd-silicide layer. Upon the formation of this uniform layer, a new generation of islands started to nucleate and then also developed into a uniform layer (on top of the first one). After the completion of this second stage of island growth, a similar third stage started to take place. While the process seemed to occur in a repetitive manner, the second and third stages were observed to proceed at much slower (~ a factor of 8) rates than that of the first one. The crystal qualities of the second and third layers were also much worse than that of the first one, as shown by the ion-channeling effect measurements and the transmission electron microscopic (TEM) studies.

More work has been concentrated on the first stage. In general, the first layer was found to be a very good single crystal (which showed Kikuchi band in electron diffraction pattern) grown epitaxially

on the substrate. The rate of consumption of the amorphous Si was measured for temperatures between 430 and 550°C. The consumption rate behaved like a thermally activated quantity (i.e., having a temperature dependence of $e^{-Ea/kT}$) corresponding to an activation energy E_a = 4.0 eV, which was very high. Besides the growth rate, the density of the nucleated islands was also found to be temperature dependent with an activation energy of 1.8 eV. We further found that island growth significantly influenced the structures of the resulting uniform layer. For example, some Pd-silicide can get trapped at the intersection of two or three islands when the uniform epitaxial layer is formed. (There is also a possibility of forming stacking faults at the intersections of islands.) This was confirmed by backscattering and TEM studies. Backscattering measurements showed that the amount of residual Pd-silicide in the Si epitaxial layer had the same temperature-dependence as that of the island density. TEM observations showed discrete Pd-containing particles (which appeared opaque) embedded in the Si epitaxial layer (which appeared semi-transparent in the micrographs). Again the density of these particles was found to have a temperature dependence corresponding to 1.8 eV. TEM observations further showed that the sizes and densities of the stacking faults were consistent with those expected from the present mechanism (i.e., the formation of stacking fault was related to the number of intersections of the islands).

While the temperature-dependence of the growth rate was found to be the same for various sets of samples, the growth rate at a

given temperature varied over a wide range (2-3 orders of magnitude) from sample to sample. After extensive investigations, the cause of such a large variation was traced to the contamination of the amorphous Si layer by the carbon crucible used for holding the Si-charge during the electron-gun evaporation. Measurements of carbon concentration (usually 1~2 atomic %) in the amorphous Si layer by the depth-profiling technique of Auger electron spectroscopy (AES) showed that the growth (SPEG) rate was indeed very sensitively dependent on the carbon concentration. The carbon-doping seemed to have stabilized the amorphous Si layer and greatly slowed down the SPEG rate. Experiments using "carbon-free" amorphous Si layer showed results which indicated that some recrystallization also took place in the amorphous Si layer. Apparently this recrystallization competes with the desired growth on the underlying single-crystal substrate. To clearly demonstrate the effect of carbon, we proposed an experiment using "carbon-free" amorphous Si layer and a controlled carbon-doping by ion implantation. Such an experiment has not been done.

Besides the kinetic aspects of SPEG, we also investigated the possibility of doping the SPEG layer to form an electrically active layer. For this purpose a very thin (≲10 Å) Sb-layer was deposited between the Pd and the amorphous Si layers during sample preparation. After SPEG, we found (both by AES and by differential Hall effect measurements) that the Sb-atoms stayed in a very narrow region near the original Sb-layer position and became electrically active.

Despite much of the effort, we still do not know where SPEG will eventually find applications in solid-state technology. Related to this subject, there are recent developments on the pulsed annealing of amorphous semiconductor layers, which show promising features. We also did some work in this area.

1.4.2 Laser Annealing

It has been demonstrated that a high-power Q-switched laser pulse can cause surface-layer melting and result in very good regrowth of ion-implanted or deposited amorphous semiconductor layers [39,40]. Motivated by better understanding of the melting process and the impurity redistributions, we have been using Rutherford backscattering techniques to study the redistribution of very thin ($\lesssim$ 10 Å) Sb-layers as a result of laser annealing.

Electron-gun evaporation was used to deposit amorphous Si layers (~ 3000 Å) onto a set of Si (100) single-crystal wafers. A very thin Sb-layer was interposed into each amorphous Si layer at a certain depth. The samples were then annealed by a Q-switched ruby laser. Significant redistributions (extending over ~1000 Å) of the Sb-atoms were observed after the laser annealing. (Some of the redistribution profiles were very close to Gaussian distributions.) The same samples were also used for pulsed electron-beam annealing. Channeling effect measurement showed the Sb-atoms to be in substitutional sites. We have been studying the redistribution as a

function of the depth of the original Sb-layer and also as a function of the annealing condition. We believe that this study can provide valuable insight into the surface-layer melting process and the important problems of doping the epitaxial layers.

Our second subject about laser annealing is on the solid-phase thin-film reactions, such as the reaction of a Pd-film with Si-substrate to form a Pd_2Si layer. This is of interest because solid-phase reactions of thin films are technologically important and have been extensively studied using thermal (furnace) annealing. We first carried out a calculation in order to predict the laser-annealing results using the existing furnace annealing data.

The calculation is simplified by the fact that energy is absorbed only in a very thin surface layer because of the metal film at surface. Under ideal conditions, the problem can be treated as a one-dimensional heat conduction problem with a source at surface. Thus, simple analytical solutions are obtained for reaction temperature T(t), if the absorbed power density P(t) is a step, linear or polynomial function of t. The thickness of the reacted film is equivalent to that of a thermal annealing at an effective temperature T_{eff}, for an effective annealing time Δt_{eff}, i.e., (reacted thickness)$^{\gamma} = A\Delta t_{eff} e^{-Ea/kT_{eff}}$, with $\gamma = 1$ for reaction-controlled process and $\gamma = 2$ for diffusion-controlled process. T_{eff} is the peak value of T(t) and $\Delta t_{eff} \cong (kT_{eff}/E_a)^m \Delta t$, where m = 1 or $\frac{1}{2}$ (determined by the function form of T(t) near T_{eff}), E_a is the activation energy of

the process, and Δt is the duration of the laser irradiation. Calculations show that irradiation times longer than 1 μsec are required for appreciable metal-silicide formation ($\gtrsim$ 100 Å) at temperature below the melting point. For short pulse irradiation ($\Delta t \lesssim 10^{-7}$ sec), measurable silicide formation thicknesses or silicon epitaxial growth will not occur unless the melting point is exceeded. Since the temperature rise is proportional to the absorbed power, we conclude that laser annealing (for solid-phase reactions) will be very sensitive to the thickness of antireflective coatings, such as SiO_2 on Si.

Experiment using scanning cw Ar^+-laser beam showed Pd_2Si and PdSi formations at power levels and irradiation times close to those predicted from the present calculations. More experiments in this area are still in progress.

The SPEG work and part of the laser annealing work have been written up for publications:

(I) SPEG

1. "Solid-Phase Epitaxial Growth of Si through Palladium Silicide Layers", C. Canali, S. U. Campisano, S. S. Lau, Z. L. Liau and J. W. Mayer, J. Appl. Phys. 46, 2831 (1975).

2. "Kinetics of the Initial Stage of Si Transport through Pd-Silicide for Epitaxial Growth", Z. L. Liau, S. U. Campisano, C. Canali, S. S. Lau and J. W. Mayer, J. Electrochem. Soc. 122, 1696 (1975).

3. "Repetitive Growth Stages in the Solid-Phase Epitaxy of Silicon", Z. L. Liau, S. S. Lau, M.-A. Nicolet and J. W. Mayer, Thin Solid Films, 44, 149 (1977).

4. "Effects of Temperature on the Solid-Phase Epitaxy of Silicon", Z. L. Liau, S. S. Lau, M.-A. Nicolet and J. W. Mayer, Thin Solid Films, 46, 93 (1977).

5. "The Crystalline Qualities of Silicon Layers Formed by Solid-Phase Epitaxial Growth", W. F. Tseng, Z. L. Liau, S. S. Lau, M.-A. Nicolet and J. W. Mayer, Thin Solid Films, 46, 99 (1977).

6. "Solid Phase Epitaxy in Silicide-Forming Systems", S. S. Lau, Z. L. Liau and M.-A. Nicolet, Thin Solid Films, 47, 313 (1977).

7. "Heterostructure by Solid-Phase Epitaxy in the Si <111>|Pd|Si (amorphous) System", S. S. Lau, Z. L. Liau, M.-A. Nicolet and J. W. Mayer, J. Appl. Phys., 48, 917 (1977).

8. "Kinetic Aspects of Solid-Phase Epitaxial Growth of Amorphous Si", Z. L. Liau, S. S. Lau, M.-A. Nicolet, J. W. Mayer, R. J. Blattner, P. Williams and C. A. Evans, Jr., Nucl. Inst. Meth. 149, 623 (1978).

9. "Antimony Doping of Si Layers Grown by Solid-Phase Epitaxy", S. S. Lau, C. Canali, Z. L. Liau, K. Nakamura, M.-A. Nicolet, J. W. Mayer, R. J. Blattner and C. A. Evans, Jr., Appl. Phys. Lett. 28, 148 (1976).

(II) Laser Annealing

1. "Redistribution of Very Thin Sb-Layers in Si After Laser Annealing", Z. L. Liau, B. Y. Tsaur, S. S. Lau, I. Golecki, and J. W. Mayer, Paper submitted to the Symposium of Laser-solid Interactions and Laser Processing, Nov. 1978, Boston, Mass.
2. "Laser Annealing for Solid-Phase Thin-Film Reactions", Z. L. Liau, B. Y. Tsaur and J. W. Mayer, Appl. Phys. Lett. (in press) .

References

1. G. Carter and J. S. Colligon, Ion Bombardment of Solids, (Elsevier, New York, 1968).
2. P. D. Townsend, J. C. Kelly and N.E.W. Hartley, Ion Implantation, Sputtering and Their Applications, (Academic Press, London, 1976).
3. G. K. Wehner, in Methods of Surface Analysis, A. W. Czanderna, ed., (Elsevier, New York, 1975).
4. P. Sigmund, Phys. Rev. 184, 383 (1969).
5. H. H. Andersen, in Physics of Ionized Gases, V. Vujnović, ed., (Inst. of Phys., Univ. Zagreb, Yugoslavia, 1974).
6. E. Gillam, J. Phys. Chem. Solids 11, 55 (1959).
7. R. Kelly and N. Q. Lam, Rad. Eff. 19, 39 (1973).
8. M. L. Tarng and G. K. Wehner, J. Appl. Phys. 42, 2449 (1971).
9. H. Shimizu, M. Ono and K. Nakayama, Surf. Sci. 36, 817 (1973).
10. P. S. Ho, J. E. Lewis, H. S. Wildman and J. K. Howard, Surf. Sci. 57, 393 (1976).
    P. S. Ho, J. E. Lewis and J. K. Howard, J. Vac. Sci. Technol. 14, 322 (1977).
11. W. Faber, G. Betz and P. Braun, Nucl. Inst. Meth. 132, 351 (1976).
12. W. K. Chu, J. K. Howard and R. F. Lever, J. Appl. Phys. 47, 4500 (1976).

References (cont'd)

13. J. M. Poate, W. L. Brown, R. Homer, W. M. Augustyniak, J. W. Mayer, K. N. Tu and W. F. van der Weg, Nucl. Inst. Meth. 132, 345 (1976).

14. Z. L. Liau, W. L. Brown, R. Homer and J. M. Poate, Appl. Phys. Lett. 30, 626 (1977).

15. D. K. Murti, R. Kelly, Z. L. Liau and J. M. Poate, (to be published).

16. Z. L. Liau, J. W. Mayer, W. L. Brown and J. M. Poate, (in press).

17. Z. L. Liau, C. J. Doherty, C. M. Mellior-Smith and J. M. Poate, Thin Solid Films (in press).

18. Z. L. Liau, B. Y. Tsaur, G. E. Chapman, S. E. Matteson and J. W. Mayer (to be published).

19. Z. L. Liau and J. W. Mayer, (to be published in J. Vac. Sci. Tech.)

Z. L. Liau and J. W. Mayer, in Treatise on Materials Science and Technology - Ion Implantation, J. K. Hirvonen, ed., (Academic Press, New York, 1979) Chapter 2.

20. H. von Seefeld, R. Behrisch, B. M. U. Scherzer, Ph. Staib and H. Schmidl, Int. Conf. on Atomic Collisions in Solids, Moscow, September, 1977.

21. H. F. Winters and J. W. Coburn, Appl. Phys. Lett. 28, 176 (1976).

22. P. K. Haff, Appl. Phys. Lett. 31, 259 (1977).

References (cont'd)

23. P. K. Haff and Z. E. Switkowski, J. Appl. Phys. 48, 3383 (1977).

24. See, for example, G. Dearnaley, J. H. Freeman, R. S. Nelson and J. Stephen, Ion Implantation, (North-Holland, Amsterdam, 1973).

25. Treatise on Materials Science and Technology-Ion Implantation. J. K. Hirvonen, ed., (Academic Press N.Y. 1979).

26. G. Carter, J. S. Colligon and J. H. Lesk, Proc. Phys. Soc. 79, 299 (1962).

27. O. Almen and G. Bruce, Nucl. Inst. Meth. 11, 257 (1961).

28. A. W. Tinsley, W. A. Grant, G. Carter and M. J. Nobes, in Ion Implantation in Semiconductors, I. Ruge and J. Graul, eds., (Springer-Verlag, Berlin-Heidelberg, 1971).

29. E. Arminen and A. Fontell, Ann. Acad. Sci. Fennical, Series A, 357 (1971).

30. E. Arminen, A. Fontell and V. K. Lindroos, Phys. Stat. Sol. (a) 4, 663 (1971).

31. J. L. Whitton, G. Carter, J. N. Baruah and W. A. Grant, Rad. Eff. 16, 101 (1972).

32. G. Carter, J. N. Baruah and W. A. Grant, Rad. Eff. 16, 107 (1972).

33. H. Kraütle, A. Feuerstein, H. Grahmann and S. Kalbitzer, in Ion Implantation in Semiconductors, S. Namba, ed., (Plenum Press, New York, 1975).

References (cont'd)

34. F. Schulz and K. Wittmaack, Rad. Eff. 29, 31 (1976).

35. P. Blank, K. Wittmaack and F. Schulz, Nucl. Ins. Meth. 132, 387 (1976).

36. B. D. Sartwell, A. B. Campbell and P. B. Needham, Jr., in Ion Implantation in Semiconductors, F. Chernow, J. A. Borders and D. K. Brice, eds., (Plenum Press, New York, 1977).

37. See, for example, V. Marrello, Ph. D. Thesis, Caltech, 1975, and references therein.

38. R. W. Bower, D. Sigurd and R. E. Scott, Solid State Electron. 16, 1461 (1973).

39. See, for example, R. T. Young, C. W. White, G. J. Clark, J. Narayan, W. H. Christie, M. Murakami, P. W. King and S. D. Kramer, Appl. Phys. Lett. 32, 139 (1978) and references therein.

40. S. S. Lau, W. F. Tseng, M.-A. Nicolet, J. W. Mayer, R. C. Eckardt and R. J. Wagner, Appl. Phys. Lett. 33, 130 (1978) and references therein.

Chapter 2

SURFACE-LAYER COMPOSITION CHANGES IN SPUTTERED ALLOYS AND COMPOUNDS

2.1 Introduction

In this Chapter, we report Rutherford backscattering measurements of the sputtered surface layer of a variety of thin-film alloys[1]. Alloys and compounds were chosen with widely ranging bonding conditions: solid solutions (Ag-Au, Cu-Au), metallic compound phases (Au_2Al, $AuAl_2$), intermetallic silicides (PtSi, Pt_2Si, NiSi), semiconductor (GaP) and oxides (Ta_2O_5 and SiO_2). We found that heavier components generally became enriched in the surface layers of the sputtered samples.

2.2 Experimental Procedures

Films of the binary alloys (Au_2Al, $AuAl_2$, $Au_{0.2}Ag$, and Cu_3Au) were prepared by vacuum evaporation. For a given alloy, two elemental metal films were deposited sequentially onto a sapphire substrate with relative film thicknesses adjusted for the desired alloy phase. The total thickness was around 3000 Å. Typical pressures during evaporation were 1×10^{-6} Torr with evaporation rates of 5 Å/sec. Film couples were alloyed by vacuum annealing at pressures better than 1×10^{-6} Torr. For Au-Al alloys, 1 h at 250°C was sufficient[2]. For Au-Ag and Au-Cu alloys,

0.5 h at 500°C was used. The composition and uniformities of the resulting alloys were determined by backscattering of 1.9-MeV $^{4}He^{+}$. Silicide films (PtSi, Pt_2Si and NiSi) were prepared by vacuum evaporation of metal films onto <100> Si single-crystal substrates and subsequent annealing[3,4]. The evaporation and annealing conditions were similar to those of the metal alloys stated above. For the study of compound semiconductor, bulk material of single-crystal GaP was used. Ta_2O_5 films ∿ 6000 Å thick were prepared by anodic oxidation of sputter-deposited Ta films; a Ta layer under the Ta_2O_5 was always retained for electrical conduction during sputtering and backscattering analysis.

Sputtering was carried out in an ion implantation accelerator. The samples were loaded in a target chamber with a liquid-nitrogen cold can of 10 cm diameter surrounding the sample holder. The pressure in the target chamber was ∿ 1×10^{-7} Torr before sputtering. Ar^+, Kr^+, Xe^+ and Ne^+ beams of 10-80 keV were generally used for sputtering. In some cases, 160 and 80 keV Ar^{++} beams were used. There was no detectable Ne^+ in the Ar^{++} beam. The pressure in the target chamber was ∿ 3×10^{-7} Torr during sputtering. The ion beam was swept across a rectangular tantalum aperture of 2.3 mm x 3.0 mm, which was placed ∿ 1 cm in front of the sample. Average beam current densities between 10 and 50 $\mu A/cm^2$ were used. The dimensions of sputtered craters were

2.3 mm x 3.0 mm, as defined by the rectangular aperture. Some ten craters were sputtered on a sample with distances of 3-4 mm between craters. An example of the lateral profile across sputtered craters is shown in Fig. 2.1 for two different Ar doses.

The sputtered samples were analyzed using 1.9-MeV $^4He^+$ backscattering with a beam spot diameter of 0.5 mm. The film thicknesses within the sputtered craters were measured by Rutherford backscattering to be uniform within 5%. The backscattering depth resolution is $\sim$ 200 Å for normal incidence. This was improved by a factor of 2, where necessary, by tilting the samples 60°.

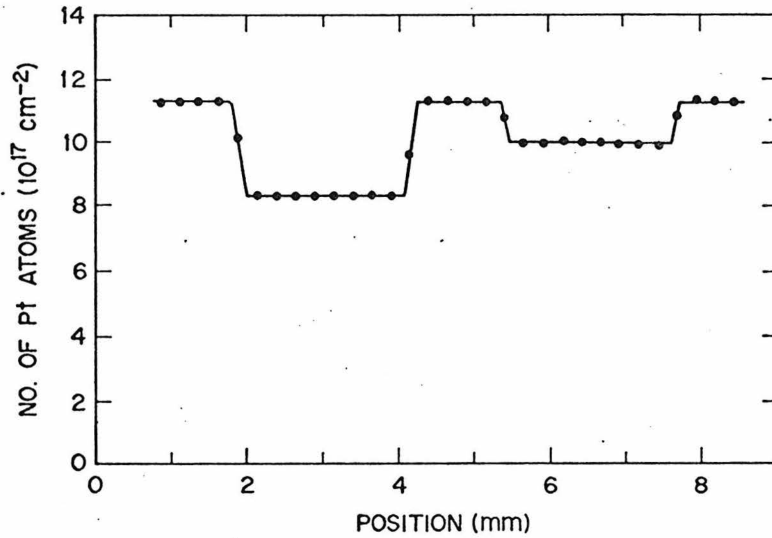

Fig. 2.1 An example of the lateral profile of sputtered craters as measured by Rutherford backscattering in which a beam spot of 0.38 mm diameter was used to scan across the craters step by step (0.25 mm each step). In each step, the same $^4He^+$ dose was used to obtain the integrated Pt counts, which was then converted into the number of Pt atoms/cm^2. These craters were produced by 80 keV Ar^+ sputtering of doses of 2.1 and 1.0 x 10^{17}cm^{-2}, respectively.

2.3 Results

Figure 2.2 shows the result for a Pt_2Si film. A surface enrichment of Pt on the sputtered sample can be seen both from the increase of the Pt signal height and the decrease of the corresponding Si signal height. The thickness of the Pt-enriched layer (about 450 Å for the shaded region in Fig. 2.2) is comparable to the width of the implanted Ar distribution (about 350 Å in Fig. 2.2). The surface composition can be calculated from the relative signal heights of Pt and Si. Most compositions were obtained from tilted target measurements. The surface composition thus calculated was $Pt_{3.5}Si$.

Ion doses between 0.5×10^{16} and $1.5 \times 10^{17} cm^{-2}$ were used for the sputtering. The surface layer became progressively Pt-enriched with increasing dose until a certain steady-state composition was attained. In Pt_2Si this steady-state composition was reached after a dose of 0.7×10^{17} ions cm^{-2}, which corresponds to the sputtering away of approximately 500 Å of the film. Similar behavior was observed in other materials.

One example with a Au-Ag alloy is shown in Fig. 2.3. The sputtered sample becomes Au-enriched ($\sim$ 20% increase in Au/Ag concentration ratio) in a surface layer of $\sim$ 350 Å. Figure 2.4 shows the result on GaP. After being sputtered by 80 keV Xe^+, the sample becomes Ga-enriched in a surface

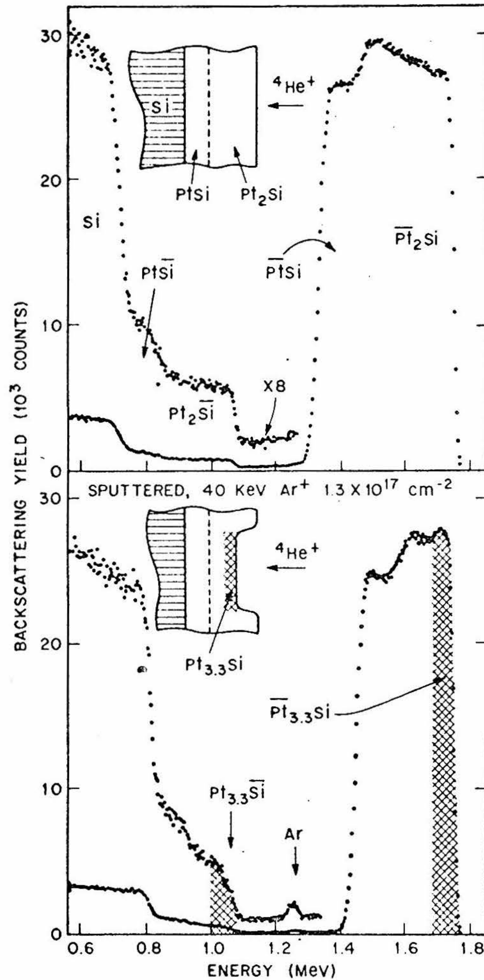

Fig. 2.2 Backscattering spectra of a Pt_2Si film before and after sputtering. The unsputtered sample has a 2500 Å layer of Pt_2Si on the surface and a 1350 Å layer of PtSi between the Si substrate and the Pt_2Si. Inside the crater, a layer of Pt_2Si of ∿ 1000 Å has been sputtered away. A Pt-enriched layer of ∿ 450 Å (shaded region) on the surface is indicated. The Si and Ar signals are magnified (x8) to reveal the layer structures. The fact that the thickness of the underlying PtSi layer does not increase after sputtering is an indication that the temperature rise during Ar^+ bombardment was < 300°C. (Ref. 3).

layer of ∿ 500 Å. The near surface composition was found to be ∿ $Ga_{1.5}P$. An example with the sputtering of Ta_2O_5 is shown in Fig. 2.5. After being sputtered by 80 keV Kr^+, a Ta-enriched layer is found over a depth of ∿ 600 Å with

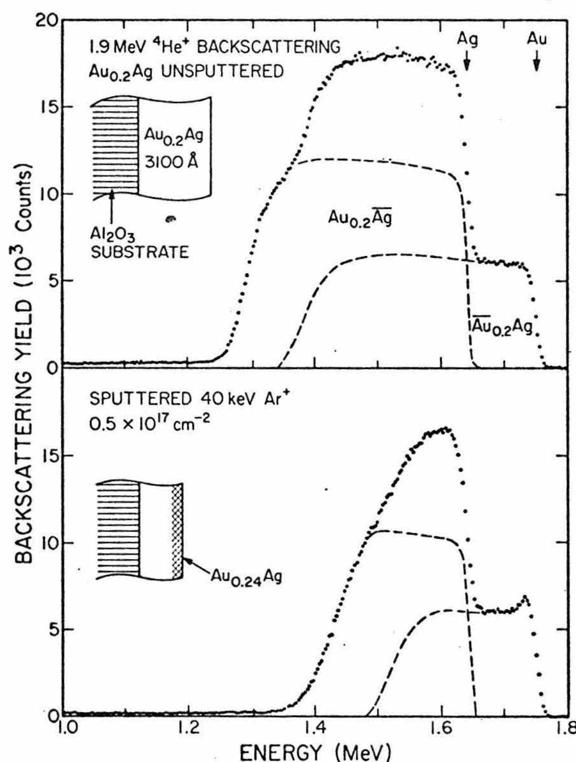

Fig. 2.3 Backscattering spectra of a Au-Ag thin-film alloy before and after being sputtered by 40 keV Ar^+. The dashed lines indicate the contributions from the Au and Ag signals. In the sputtered sample, an extra Au peak shows up near the Au signal edge, indicating a Au enrichment in a surface layer of ∿ 350 Å. From the Au peak height, the surface composition was calculated to be $Au_{0.24}Ag$.

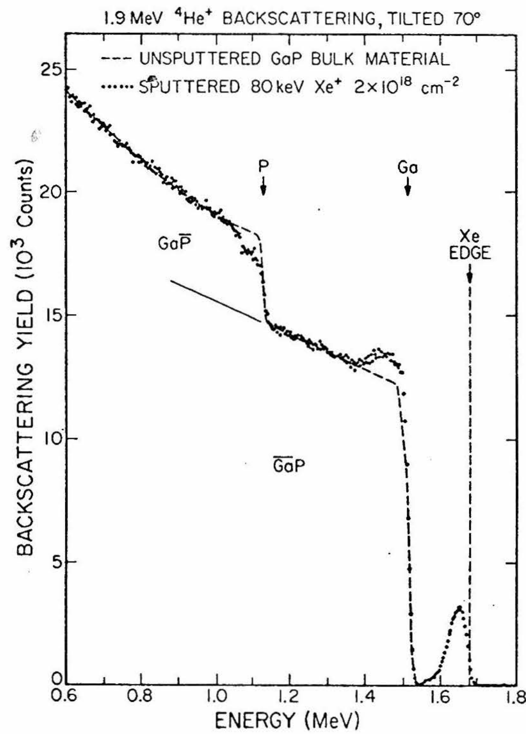

Fig. 2.4 Backscattering spectrum of a GaP sample after being sputtered by 80 keV Xe^+ and that of an unsputtered one. The sputtered sample shows a Ga-enrichment in a surface layer of $\sim$ 500 Å.

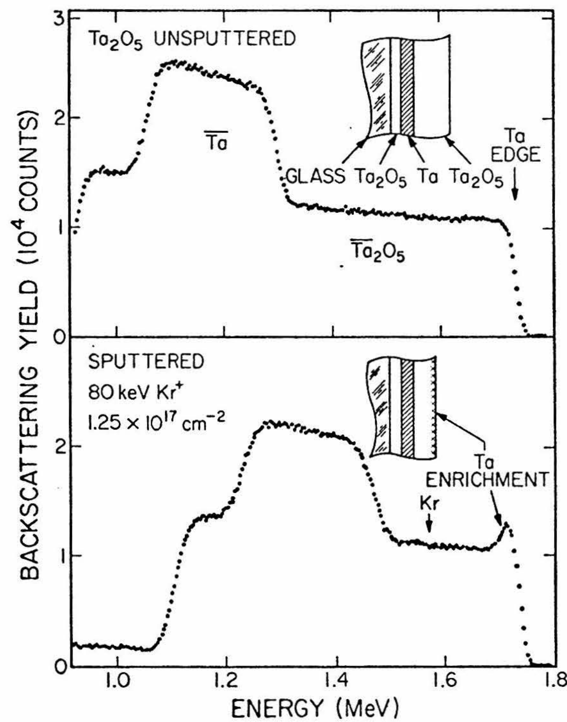

Fig. 2.5 Backscattering spectra of a Ta_2O_5 film before and after being sputtered by 80 keV Kr^+. The unsputtered Ta_2O_5 was ∿ 6000 Å thick. After sputtering, a Ta-peak appears near the Ta signal edge, indicating a Ta-enrichment in a surface layer of ∿ 600 Å thick.

TABLE 2.1

Steady-State Surface Compositions
In Sputtered Alloys and Compounds

Materials Studied	Enriched Component	Surface Composition
$Au_{0.2}Ag$	Au	$Au_{0.24}Ag$
$Au_{0.3}Cu$	Au	$Au_{0.33}Cu$
$Au_2\ Al$	Au	$Au_{3.8}Al$
$AuAl_2$	Au	$Au_{1.3}Al_2$
Pt_2Si	Pt	$Pt_{3.5}Si$
PtSi	Pt	$Pt_{2.1}Si$
NiSi	Ni	$Ni_{1.6}Si$
GaP	Ga	$Ga_{1.5}P$
Ta_2O_5	Ta	$Ta_{4.6}O_5$

a surface composition of $\sim Ta_{4.6}O_5$. Table 2.1 summarizes the results.

The composition and thickness of the altered surface layers were investigated for Ne^+, Ar^+, Kr^+ and Xe^+ sputtering of 20-80 keV. For a given material, the steady-state surface composition was independent of the mass and energy of the sputtering ion. The thickness of the surface layer was proportional to the range of the implanted ion.

2.4 Interpretations and Implications

These results are suggestive of a general rule that, for a given material, it is always the heavier component that becomes enriched after sputtering. Indeed other workers have observed enrichment of the heavier element in the sputtering of oxides[6,7] and Ag-Au[8], Cu-Au[8,9] and Al-Cu[10] alloys. A Ta-enrichment in light-ion sputtered Ta_2O_5 has recently been reported by Seefeld et al.[11]. The exception appears to be the Cu-Ni system where Ni enrichment is observed[12-14].

Based on the collision cascade picture of sputtering, a calculation has been carried out which indicates preferred energy partition for the light species[15]. This would lead to preferential sputtering. Even without preferential energy partition, there are other possible mechanisms for the light component to be preferentially sputtered. For example, the

light atoms can be preferentially sputtered because of reflections from heavy atoms[16]. It may also be easier for light atoms to escape from the material because of smaller energy loss they suffer when moving through the material[1, 17,18]. Therefore, the light atoms could emerge from a greater depth than that of the heavy atoms. Difference in surface binding energies for the two components may also be one important factor for preferential sputtering. The influence of surface binding energies has been noted in the sputtering of oxides and alloys[19].

The fact that the steady-state composition is independent of the mass and energy of the bombarding ion indicates that the steady-state composition is indeed determined by the underlying alloy composition. At steady-state, the material sputtered off must have the same composition as the underlying alloy. The surface layer will therefore adjust in composition to compensate for the preferential sputtering.

Another important question is the observed thicknesses of the altered surface layer. It is known that the majority of sputtered atoms emerge only from the outmost few atomic layers near the surface. Therefore, with preferential sputtering, one can only expect a composition change in the outmost few atomic layers rather than in a depth comparable to the ion range. The observed thickness of the altered layer requires some atomic mixing or interdiffusion which can propagate the composition change from the surface to the

deeper region. Either the enriched heavy atoms can move inward to dilute the surface enrichment, or the light atoms can move outward to replenish the depletion of light atoms at the surface. So, finally, the composition over the whole layer is changed.

References

1. Z. L. Liau, W. L. Brown, R. Homer and J. M. Poate, Appl. Phys. Lett. 30, 626 (1977).

2. S. U. Campisano, G. Foti, E. Rimini, S. S. Lau and J. W. Mayer, Philos. Mag. 31, 903 (1975).

3. J. M. Poate and T. C. Tisone, Appl. Phys. Lett. 24, 391 (1974).

   C. Canali, C. Catellani, M. Prudenziati, W. H. Wadlin and C. A. Evans, Jr., Appl. Phys. Lett. 31, 43 (1977).

4. K. N. Tu, E. I. Allessandrini, W. K. Chu, H. Kräutle and J. W. Mayer, Jpn. J. Appl. Phys. Suppl. 2, 669 (1974).

5. W. K. Chu, J. W. Mayer, M-A. Nicolet, T. M. Buck, G. Amsel and F. Eisen, Thin Solid Films 17, 1 (1973).

6. R. Kelly and N. Q. Lam, Rad. Eff. 19, 39 (1973).

7. H. M. Naguib and R. Kelly, Rad. Eff. 25, 1 (1975).

8. W. Färber, G. Betz and P. Braun, Nucl. Inst. Meth. 132, 351 (1976).

9. E. Gillam, J. Phys. Chem. Solids 11, 55 (1959).

10. W. K. Chu, J. K. Howard and R. F. Lever, J. Appl. Phys. 47, 4500 (1976).

11. H. von Seefeld, R. Behrisch, B. M. U. Scherzer, Ph. Staib and H. Schmidl, Int. Conf. on Atomic Collisions in Solids, Moscow, September, 1977.

12. M. L. Tarng and G. K. Wehner, J. Appl. Phys. 42, 2449 (1971).

References (cont'd)

13. H. Shimizu, M. Ono and K. Nakayama, Surf. Sci. 36, 817 (1973).

14. P. S. Ho , J. E. Lewis, H. S. Wildman and J. K. Howard, Surf. Sci. 57, 393 (1976).

15. N. Andersen and P. Sigmund, K. Dan, Viden. Selskab. Matt.-Fys. Medd. 39, No. 3 (1974).

16. H. F. Winters and P. Sigmund, J. Appl. Phys. 45, 4760 (1974).

17. Z. L. Liau, J. W. Mayer, W. L. Brown and J. M. Poate, J. Appl. Phys. (in press).

18. P. K. Haff, Appl. Phys. Lett. 31, 259 (1977).

19. R. Kelly, Nucl. Inst. Meth. 149, 553 (1978).
E. Giani, D. K. Murti and R. Kelly, in Thin Film Phenomena - Interfaces and Interactions, J. E. E. Baglin and J. M. Poate, eds., (Electrochemical Society, Princeton, 1978) p. 443.

Chapter 3

SPUTTERING OF PtSi

3.1 Introduction

In Chapter 2, we reported the surface layer composition changes in various alloys and compounds as a result of sputtering by rare-gas ions of 20-80 keV. The compositions and thicknesses of the layers were determined by backscattering technique. However, since the layer thicknesses were generally comparable to the depth resolution (∿ 200 Å) of the backscattering technique, very little has been learned about the composition depth profiles and the formation kinetics of the altered surface layers. Other experimental problems, such as signal overlap, background noise and interference from the implanted species also added to uncertainties.

In this Chapter, we introduce techniques which have been developed to overcome these difficulties[1,2]. The work has concentrated on the Ar-sputtering of PtSi. Glancing angles have been used to improve the backscattering depth resolution from 200 Å at normal incidence to ∿ 40 Å at 80° incidence. For some experiments, the sample configuration was designed to allow simultaneous measurements of both Pt and Si as well as the implanted Ar. Thus, composition profiles and sputtering yields of Pt and Si can be measured as

a function of Ar dose and energy.

3.2 Depth Profiles of Pt-Enrichment

Figure 3.1 shows a backscattering spectrum of a PtSi film sputtered by 1.56×10^{17} 80 keV Ar^{++}/cm^2. For comparison, an unsputtered sample is also shown in Fig. 3.1.

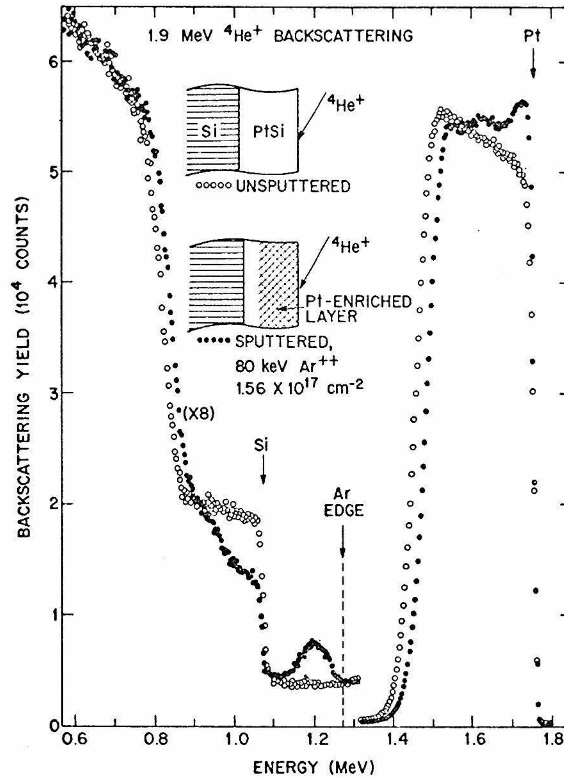

Fig. 3.1 Backscattering spectra of an 80 keV Ar^{++} sputtered and unsputtered PtSi sample. The incident angle (with the surface normal) of $^4He^+$ beam was 60° in both cases. In the sputtered sample, some 960 Å of material has been sputtered off from an originally 2200 Å thick PtSi film. The unsputtered sample shown in this figure is from a 1460 Å PtSi film. (The reason for choosing a thinner unsputtered sample was to avoid signal overlap and high background on the Si signals.) The Ar edge (the energy position of Ar at the surface) is calculated from Pt and Si edges and by a Ni edge (not shown in the figure) from a Ni sample.

In the sputtered sample, the Pt signals near the Pt-edge (the energy of ^{4}He particles scattered from the Pt atoms at the surface) become higher than in the unsputtered sample, while the corresponding Si signals become lower. This indicates that the sputtered sample is Pt-enriched in a layer starting from the surface. In the spectrum, the Pt-enriched layer extends to an energy width of $\sim$ 200 keV which corresponds to a depth of $\sim$ 750 Å.

The implanted Ar in the sputtered sample can also be seen in Fig. 3.1. The peak of the Ar distribution corresponds to an Ar concentration of $0.4 \times 10^{22} cm^{-3}$ and is located $\sim$ 70 keV below the Ar edge which corresponds to a depth of $\sim$ 370 Å from the surface. Due to its contribution to the energy loss of the analyzing helium ions, the presence of this Ar distribution will cause a $\sim$ 5% depression in Pt signals at $\sim$ 70 keV below the Pt edge. The observed dip in the enriched Pt signals of the sputtered sample in Fig. 3.1 is caused by the presence of the Ar. Similarly, there should also be an extra $\sim$ 5% depression of Si signals at $\sim$ 70 keV below the Si edge, although this is hard to discern in the already depressed Si signal because of Si depletion.

To obtain the depth profile of the Pt/Si concentration ratio, the corresponding Pt and Si signal heights should be taken from energy positions that correspond to the same depth below the surface[3]. For this purpose, the Pt signal

height $H_{Pt}(E)$ was taken for a given energy E measured below the Pt edge. The Si signal height $H_{Si}(E')$ was also taken for the corresponding energy E' (below the Si edge). ($E \simeq 1.17\ E'$ in the present case). The Pt/Si concentration ratio $\frac{n_{Pt}}{n_{Si}}(E)$ was then directly calculated from $\frac{H_{Pt}(E)}{H_{Si}(E')}$ using Rutherford scattering cross sections and the backscattering kinematics[3]. To convert $\frac{n_{Pt}}{n_{Si}}(E)$ into $\frac{n_{Pt}}{n_{Si}}(z)$, (where z is the depth from the surface of the sample), $\frac{dE}{dz}$ was evaluated for each E, using the elemental values of $\frac{dE}{dz}$'s for Pt and Si, $\frac{n_{Pt}}{n_{Si}}(E)$ and Bragg's rule[4]. Assuming an atomic density of $6 \times 10^{22} cm^{-3}$, $\frac{dE}{dz} \simeq 52$ eV/Å is obtained for unsputtered PtSi. This value is nearly constant throughout the thickness of the sample[4]. In the sputtered sample, the Pt-enrichment causes $\lesssim 10\%$ increase in $\frac{dE}{dz}$, while the presence of Ar causes a few percent decrease.

The $\frac{n_{Pt}}{n_{Si}}(z)$ thus calculated for the sputtered sample in Fig. 3.1 is shown in Fig. 3.2. As a test of the analytical method stated above, the same analysis was also carried out for the unsputtered sample in Fig. 3.1. It yielded a constant $\frac{n_{Pt}}{n_{Si}}$ to within 1% over the thickness of the PtSi film. (Fig. 3.2)

Figure 3.2 also shows $\frac{n_{Pt}}{n_{Si}}(z)$ for samples sputtered with 80 keV Ar^{++} at lower doses. In all cases, the region of Pt-enrichment extended to depths of ~ 750 Å. In Fig. 3.2 the Pt-enrichment was observed to increase with Ar dose.

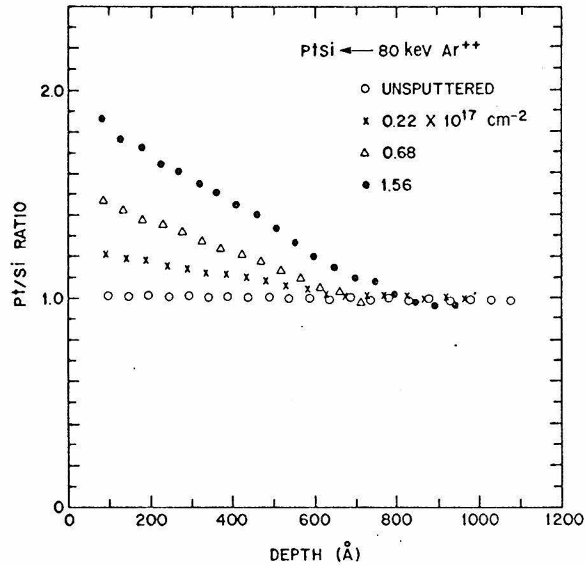

Fig. 3.2 Depth profiles of Pt/Si concentration ratio for 80 keV Ar^{++} sputtered samples.

Due to the limitation of energy resolution, the Pt/Si concentration ratios within the first few atomic layers of the surface region cannot be directly measured with the present technique. However, assuming smooth depth profiles, the surface Pt/Si ratios can be obtained by extrapolating from the measured profiles.

Figure 3.3 shows the surface Pt/Si ratios determined in this way for 80 keV Ar^{++} sputtered samples. The surface Pt/Si ratio increases with increasing Ar dose approaching a steady-state value ($\sim$ 1.94 in Fig. 3.3) for doses $\gtrsim$ 1.5 x $10^{17} cm^{-2}$.

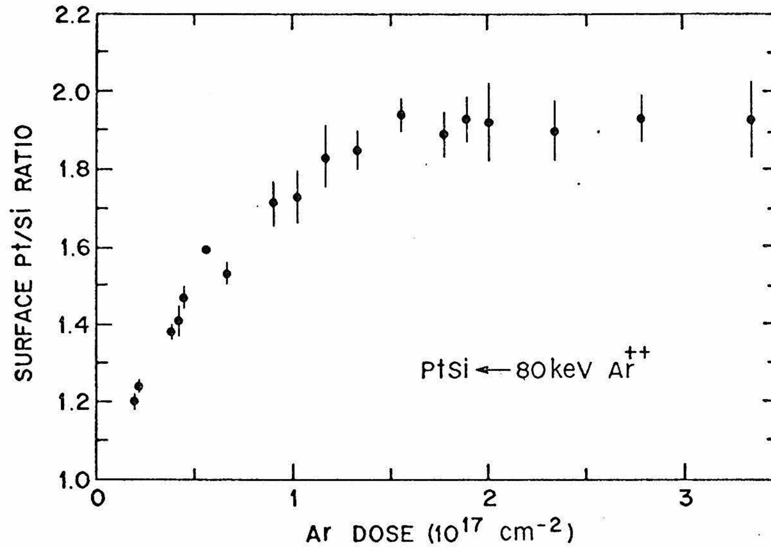

Fig. 3.3 The surface Pt/Si concentration ratio, N_{Pt}/N_{Si}, as a function of Ar dose ϕ, in the 80 keV Ar^{++} sputtering of PtSi.

The surface layer Pt-enrichment was also observed for Ar energies between 10 and 160 keV. For a given energy, the Pt-enrichment extended to approximately the same depth, with its amplitude increasing until attainment of steady-state. The thickness of the Pt-enriched layer was related to the Ar range. It was also found that less sputtering was required to reach steady-state when lower Ar energy was used. Sputtering of an amount of material comparable to the thickness of the altered layer was required to reach steady-state.

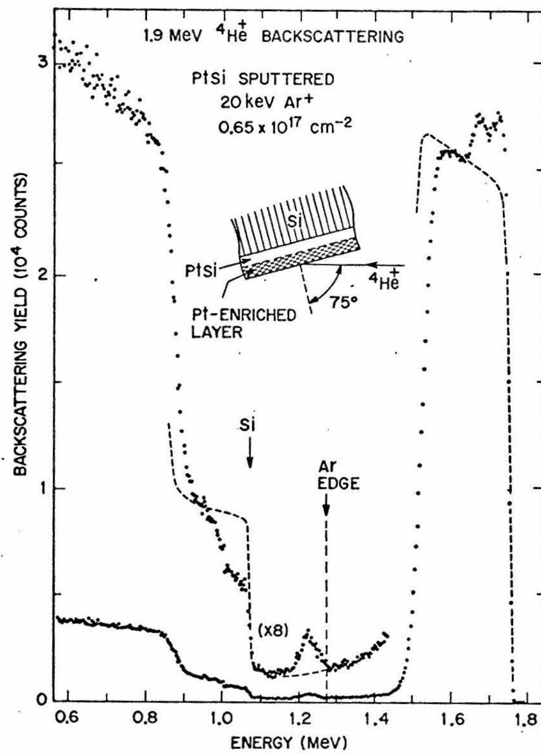

Fig. 3.5 The backscattering spectrum of a 20 keV Ar^+ sputtered PtSi sample. The surface Pt-enriched layer is ∿ 240 Å. Some 500 Å of material has been sputtered off.

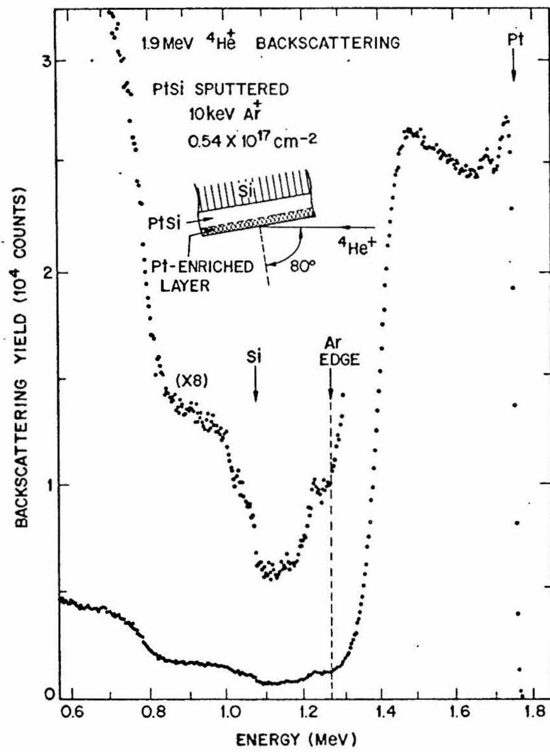

Fig. 3.6 The backscattering spectrum of a 10 keV Ar^+ sputtered PtSi sample. The surface Pt-enriched layer is ∿ 130 Å.

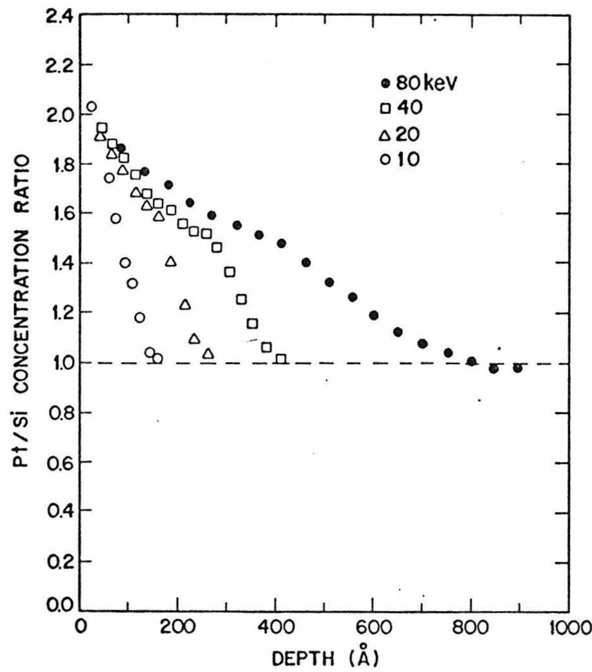

Fig. 3.7 Steady-state Pt/Si profiles of 10, 20, 40 and 80 keV Ar sputtered PtSi samples.

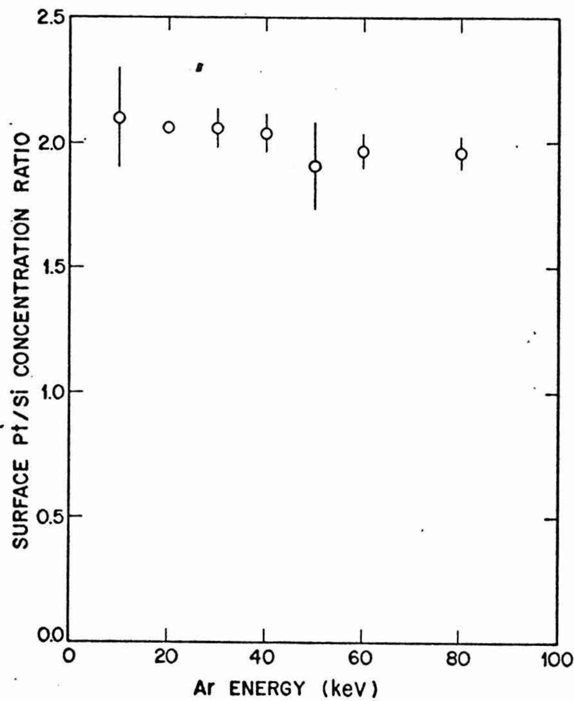

Fig. 3.8 Steady-state surface Pt/Si concentration ratios of 10-80 keV Ar sputtered PtSi samples.

Figures 3.4, 3.5 and 3.6 show backscattering spectra of samples sputtered at 40, 20 and 10 keV, respectively. In each case, a dose was chosen such that the Pt-enrichment reached the steady-state. In each spectrum, the implanted Ar is seen to distribute to a depth almost identical to the Pt-enrichment. This is reflected from the dip on the Pt signals as well as from the position of the Ar signals.

Figure 3.7 shows concentration ratios $\frac{n_{Pt}}{n_{Si}}(z)$ calculated from data in Figs. 3.1, 3.4, 3.5 and 3.6. In addition to a monotonic decrease of $\frac{n_{Pt}}{n_{Si}}$ from its surface value, there is a well-resolved knee in the 20 and 40 keV profiles. Such a knee is less well-defined in the 80 keV profile and is not resolved in the 10 keV profile.

Figure 3.7 also shows that the surface Pt/Si ratio was nearly the same for various energies. The steady-state surface Pt/Si ratio was measured for a series of samples sputtered at different Ar energies. The results are plotted in Fig. 3.8. There might be a slight energy dependence ($\sim$ 10% variation from 10 to 80 keV). However, it could be due to the data extrapolation, since higher angle tilting was used in the backscattering analysis of lower energy Ar sputtered samples.

Experiments were also carried out for samples kept at high and low temperatures during sputtering with 80 keV Ar^+. No appreciable differences were observed in the profiles

between samples sputtered at liquid nitrogen temperature and those shown in Fig. 3.1. One sputtering run was made with a sample heated at 275°C; the data showed substantial flattening of the Pt-enrichment profile (i.e. the magnitude of $\frac{n_{Pt}}{n_{Si}}(z)$ was smaller, but penetrated deeper into the sample). This can be explained as an annealing effect due to the replenishment of Si from the Si substrate. (Since 275°C was close to Pt-silicide formation temperatures.) One single experiment was done using 500 keV Ar^+ (from a van de Graaff generator) for sputtering. Pt-enrichment to a composition similar to that of lower Ar energy sputtering was observed.

3.3 Yields of Pt and Si in PtSi Sputtering

The backscattering technique was also used to measure the yields of Pt and Si in the sputtering of PtSi samples. For this purpose, differences of integrated Pt (or Si) counts between unsputtered and sputtered samples were taken. In doing so, special samples (see Figs. 3.9 and 3.10) were made to reduce experimental uncertainties. To avoid the problems associated with extracting the Si signal in PtSi from that of the substrate, the PtSi was formed on sapphire [(2)]. The backscattering spectrum from such a sample is shown in Fig. 3.9. Clean sapphire (Al_2O_3) slabs of 1 cm x 2 cm dimension were used as substrates. Layers of W, Pt and Si of 19, 190 and 28 $\mu g/cm^2$, which corresponded to 100, 900

and 1200 Å thicknesses, respectively, were deposited sequentially by electron gun evaporation. The W layer served two purposes: (1) to improve the adhesion between Pt and the substrate, and (2) to increase the energy separation of the backscattering signals from Si and Al. The samples were vacuum annealed to form PtSi. The conditions of evaporation, annealing and backscattering analysis were similar to those for PtSi on Si substrates. The relative thicknesses of the Pt and Si layers had to be adjusted for exact PtSi stoichiometry. For this purpose, several trial runs were carried out to correct the thickness calibration.

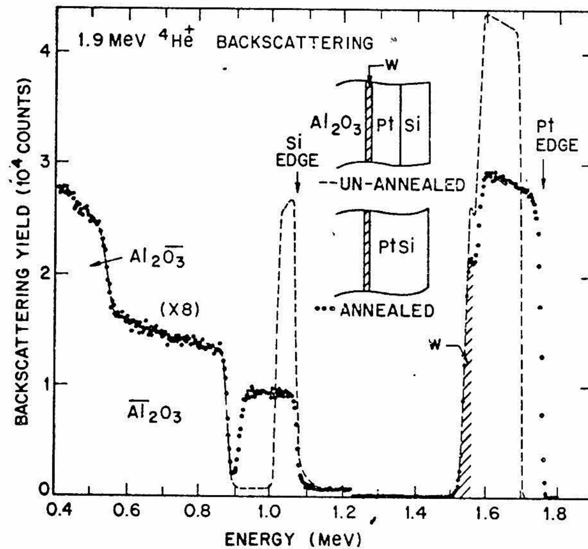

Fig. 3.9 The specially prepared thin-film PtSi sample in which the Si signals are essentially isolated from the signals from the substrate. The Si, Al and O signals have been magnified a factor of 8.

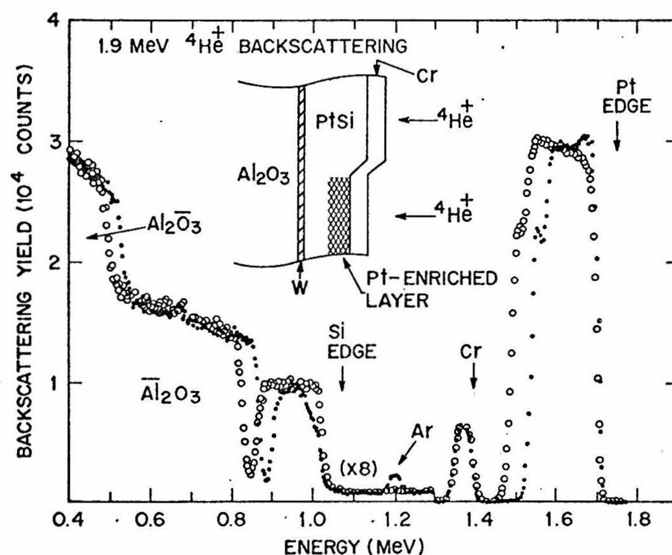

Fig. 3.10 Backscattering spectra from the thin-film structure used to measure yields of Pt and Si in the sputtering of PtSi. The unsputtered area has a PtSi film thickness of ∿ 1800 Å. In the crater, about 450 Å of material have been sputtered off by 40 keV Ar^+ ($0.62 \times 10^{17} cm^{-2}$) and a Pt-enriched layer of ∿ 400 Å appears at the surface. The subsequently deposited Cr film (∿ 500 Å) serves as a monitor for $^4He^+$ dose.

A uniform Cr layer of ∿ 500 Å was evaporated onto the sputtered sample as a monitor for $^4He^+$ doses, because the total backscattering yields of this Cr layer are proportional to the $^4He^+$ dose. By this technique, $^4He^+$ dose normalization was checked to better than 1%. To eliminate errors due to possible non-uniformity of the starting PtSi film, a backscattering measurement was always made on the unsputtered area just next to each sputtered crater (Fig. 3.10). To avoid errors due to possible non-uniformities of the sputtered craters, the samples were positioned so that the $^4He^+$ beam hit the center of each sputtered crater. Also, the PtSi films to be sputtered were made as thin as possible; the thickness exceeded the amount of material sputtered to reach steady-state at 40 keV. This was to reduce errors in taking differences of total Pt (or Si) backscattering yields, and to reduce the background on Si signals. Flat backgrounds were assumed in extracting Si backscattering yields.

The results are shown in Fig. 3.11. In the 40 keV case, some Ar doses were higher than that required for reaching steady-state. The Si and Pt data points tend to fall on a pair of parallel lines which is in agreement with the equal sputtering rates of Si and Pt in the steady-state. The separation between these two parallel lines, which is the excess Si atoms sputtered off the material, is $(0.62 \pm 0.05) \times 10^{17}$ cm^{-2}. This is in agreement with the excess Pt in the

Pt-enrichment profile, which is $(0.55 \pm 0.05) \times 10^{17} cm^{-2}$ as estimated from Fig. 3.7. In the 80 keV case, the doses were not high enough to reach the steady-state. Nevertheless, the separation between the Si and Pt data points was already larger than in the 40 keV case, as expected from the Pt-enrichment profiles in Fig. 3.7.

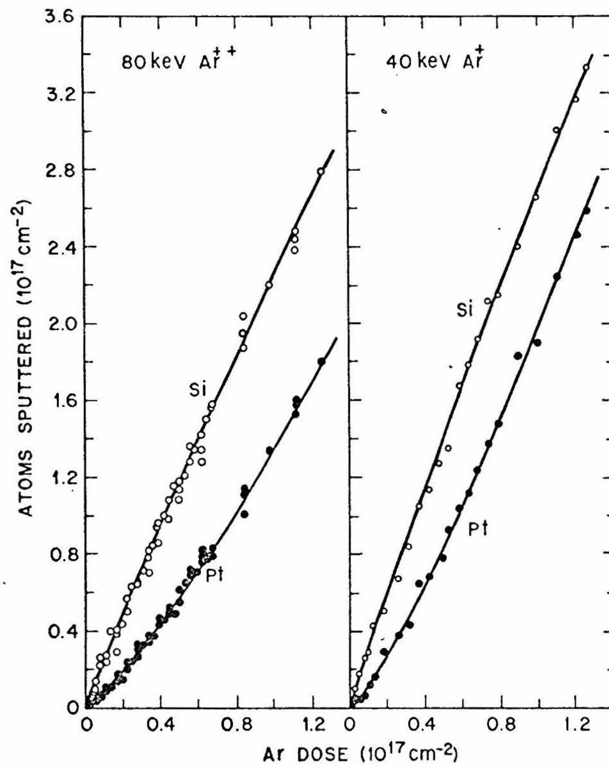

Fig. 3.11 Numbers of sputtered Si and Pt atoms as a function of Ar dose. The smooth curves were drawn to fit the data.

Define the yields of Si and Pt as:

$$S_{Si} \equiv \frac{\Delta N_{Si}}{\Delta N_{Ar}}$$

and

$$S_{Pt} \equiv \frac{\Delta N_{Pt}}{\Delta N_{Ar}}$$

where N_{Si} and N_{Pt} are numbers of Si and Pt atoms sputtered off the material, and N_{Ar} is the number of incident Ar ions. Thus, S_{Si} and S_{Pt} can be determined as the derivatives of the data in Fig. 3.11. Because of experimental errors in N_{Si} and N_{Pt}, there were more uncertainties in the determination of S_{Si} and S_{Pt}. To eliminate random errors, pairs of smooth curves were drawn to fit data in Fig. 3.11. Derivatives of these curves were then taken as S_{Si} and S_{Pt}.

The results are shown in Fig. 3.12. In the low dose region, $S_{Si} \gtrsim 2.4\ S_{Pt}$ for both energies. The values of S_{Pt} and S_{Si} then approach each other and finally merge into an equal value. In the 80 keV case, the Ar dose at which S_{Si} equals S_{Pt} is estimated to be $\sim 2 \times 10^{17} cm^{-2}$. This is in agreement with the dose required to reach the steady-state Pt-enrichment, which is $\sim 2 \times 10^{17} cm^{-2}$ as estimated from Fig. 3.3.

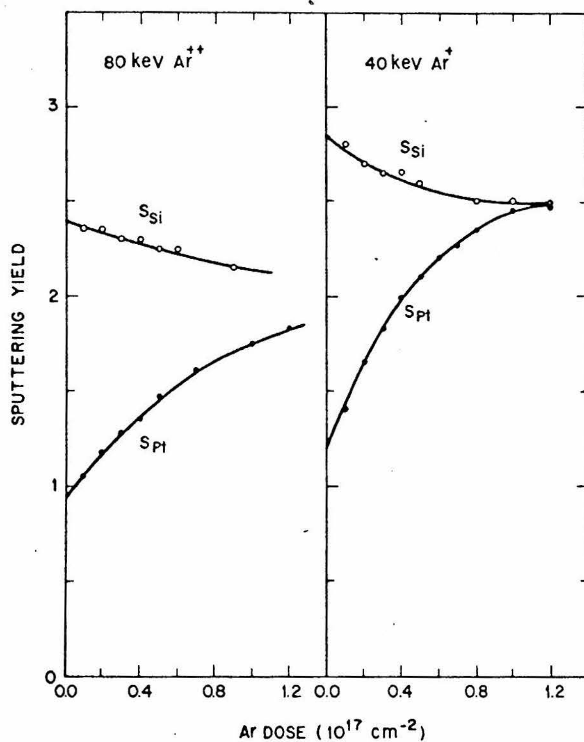

Fig. 3.12 Yields of Si and Pt atoms per incident Ar atom as functions of Ar dose. These values are derivatives of the curves in Fig. 3.11.

3.4 Observation of Ar Bubble Formation

In the previous sections, it has been noticed that the implanted Ar is distributed over depths comparable to those of Pt-enrichment. Measurement of Ar distribution as a function of Ar dose actually showed evidence of Ar bubble formation in the material[5].

Figure 3.13 shows a series of backscattering spectra of a sample which has been sputtered by 160-keV Ar^{++}. Starting with a PtSi film 4200 Å thick (spectrum 0 in Fig. 3.13), the Ar dose was incremented equal steps with 0.16 x $10^{17} cm^{-2}$ per step. Some 100 Å of Pt-silicide was sputtered off after each step. In Fig. 3.13, the indicated Ar edge was calculated from Pt, Si and Ni signal edges. (A nickel sample was used to obtain the Ni signal edge.) In all sputtered samples, signals of implanted Ar can be seen, above from a background which was mainly due to the Pt signals.

An interesting feature is the evolution of the Ar distribution. It developed into a sharp peak (spectra 1-3). The peak then grew bigger and appeared closer to the surface of the sample (spectrum 4). Finally it disappeared at the surface (spectrum 5). The process then repeated itself (spectra 6-9).

The formation of a sharp Ar peak is an indication of condensation of Ar into a narrower region, even the formation of large Ar bubbles. Thus, Fig. 3.13 suggests a repetitive process for Ar bubble formation. Because the sputtering causes the sample surface to recede, when the front face of

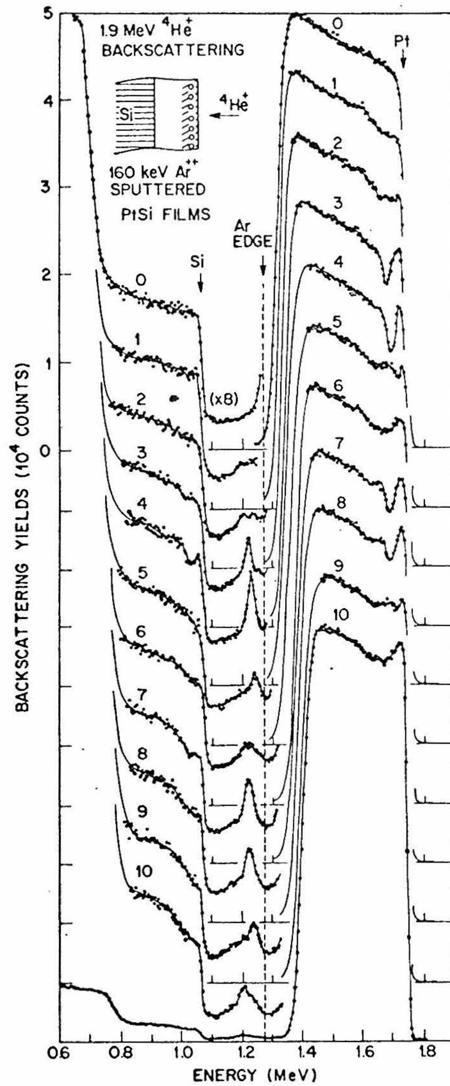

Fig.3.13 Backscattering spectra of a sequence of Ar-sputtered PtSi samples which indicate a repetitive Ar bubble formation process. The Si and Ar signals have been magnified a factor of 8. The number labeled on each spectrum corresponds to its Ar doses ($1.65 \times 10^{16} cm^{-2}$ x number).

the bubble is exposed, Ar can escape from the material. Upon this release of the previously implanted Ar, new bubbles can start to form due to the newly implanted Ar.

To further investigate this phenomenon, cross sections of the samples were studied by TEM[6]. For comparison, samples with and without a strong indication of bubbles (spectra 4 and 10 of Fig. 3.13) were chosen for the TEM observation.

The results are shown in Fig. 3.14. Some circular and more transparent regions appeared near the surface of the sample for which backscattering suggested bubbles. Since their depths and sizes are in good agreement with backscattering data, these circular objects are, therefore, identified as due to Ar bubbles. Such objects were not observed in the sample for which backscattering showed no indication of bubbles.

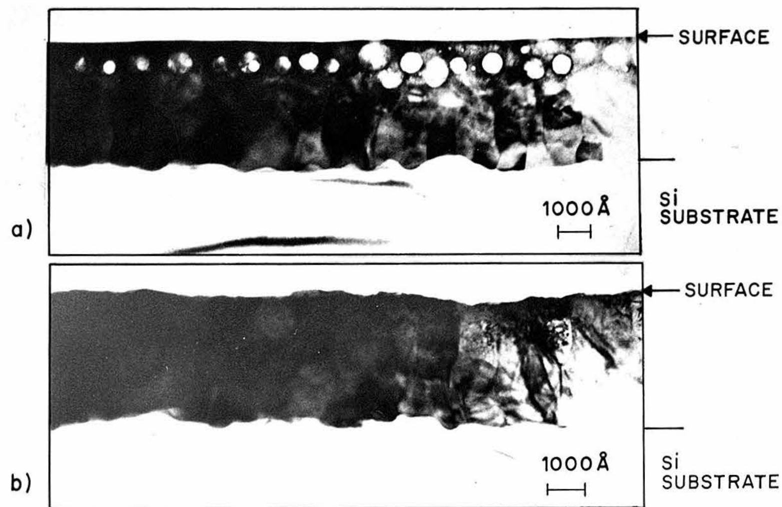

Fig. 3.14 TEM pictures of the cross sections of two Ar-sputtered PtSi samples. (a) and (b) are from samples of spectra 4 and 10 of Fig. 3.13, respectively. The circular objects in (a) are evidence of bubble formation. The surface roughness in (b) is probably due to the exposure of bubbles to the surface.

From the TEM picture, the average diameter and depth (of the front face) of the bubbles are measured to be 700 and 400 Å, respectively. Assuming a sample thickness of $\sim$ 1000 Å (in the direction normal to the paper), the density of bubbles (viewed in the direction normal to the sample surface) is calculated to be $\sim 1 \times 10^{10}$ bubbles/cm^2. On the other hand, the amount of Ar atoms in the sample as calculated from the backscattering data (spectrum 4 of Fig. 3.13) is $\sim 3.3 \times 10^{16}$ Ar atoms/cm^2. Therefore, the average number of Ar atoms in one bubble is estimated to be $\sim 3 \times 10^6$, which corresponds to a density of $\sim 2 \times 10^{22}$ Ar atoms/cm^3.

It is interesting to point out that the bubble formation can indeed affect the shape of Ar signals in the backscattering spectra. This is illustrated in Fig. 3.15. Suppose there are equal numbers of Ar atoms distributed in the depth regions from x to $x + \Delta x$ in PtSi samples A and B. The shapes of the Ar signals in the backscattering spectra will, however, look rather different if, in case A, the Ar atoms are uniformly embedded in PtSi, while in case B the Ar atoms condense to form bubbles of diameter Δx. This is because, in backscattering analysis, the He ions suffer much less energy loss traveling through the Ar atmosphere than through PtSi. Therefore, with bubble formation, the Ar signals will appear in a narrower region (and, hence, larger signal height) in the backscattering spectrum. Taking the

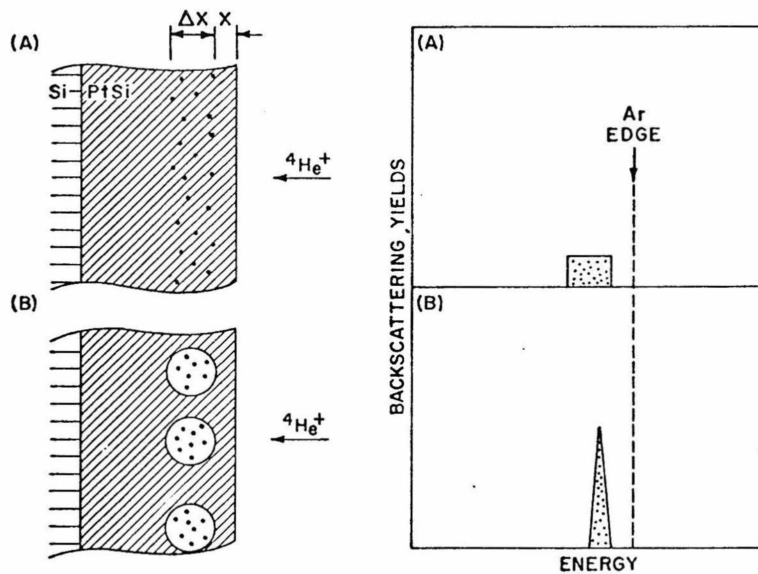

Fig. 3.15 A schematic picture which illustrates the effect of bubble formation on the backscattering spectrum. The dots represent Ar atoms in the PtSi samples. For equal numbers of Ar atoms in samples A and B, the areas under the Ar spectra of A and B should be approximately equal. The bubble formation causes the Ar spectrum to sharpen up. The Pt and Si signals are not shown in the spectra.

dE/dx and the spherical shape of bubbles into consideration, the shapes of Ar signals should appear approximately as those shown in Fig. 3.15. Thus, the present argument is quite consistent with the observed Ar peak formation in Fig. 3.14.

To further investigate the bubble formation picture, it is desirable to have TEM observations of bubbles at various Ar doses. However, such observations are not available at the present time (mainly due to difficulties in preparing TEM samples). On the other hand, backscattering data showing effect similar to that in Fig. 3.13 were obtained for sputtering using lower-energy Ar^+ (80-20 keV). It was also noted that, for lower Ar^+ energy, less sputtering was required to complete one cycle of the bubble formation. This seems to be consistent with the present picture. Because, for lower Ar^+ energy, the bubbles form at a shallower depth from the surface, therefore, less sputtering is needed for the bubbles to intersect the surface. Backscattering data also indicated that the sizes of the bubbles were smaller at lower Ar energies. The critical size of bubbles is probably related to the ion range and sputtering rate.

In Fig. 3.13, two cycles of bubble formation were observed. We do not know whether the process will continue to the third cycle or even more. Ideally, it is expected from the present picture that the system will continue to form bubbles repetitively. However, while the sample had a flat surface to begin with, the surface becomes rougher as the bubbles reach the surface (as seen in Fig. 3.14). Therefore, if the bubbles continue to form, they may no longer be formed in coherent fashion. This will gradually smear out the effect in the backscattering observation.

As mentioned earlier, the sputtered PtSi generally becomes Pt-enriched in a surface layer with its thickness comparable to the ion range. This Pt-enrichment was also observed in the present case. In Fig. 3.13, the Pt signal heights near the Pt edge increase with Ar dose, with corresponding decreases in Si signal heights near the Si edge. Furthermore, this Pt-enrichment extends to a depth comparable to that of the Ar distributions. We have previously suggested that this Pt-enriched layer is due to preferential sputtering at the surface in combination with enhanced diffusion over the ion range. The formation of Ar bubbles does indeed indicate a certain mobility of atomic species in the layer during ion bombardment. This mobility or enhanced diffusion seems to be necessary in explaining the Pt-enrichment to a depth comparable to the ion range.

The present results also provide insights into other roblems associated with sputtering. An immediate example ould be the surface roughening. As sputtering proceeds, he surface roughness will increase as subsequent generations f bubbles are exposed to the surface. The related quantities, uch as critical bubble size, bubble density per unit area, nd amount of sputtering required to complete one cycle of ubble formation, would be important parameters in consider- ng this surface-roughening process.

References

1. Z. L. Liau, J. W. Mayer, W. L. Brown and J. M. Poate, J. Appl. Phys. (in press).
2. Z. L. Liau, C. J. Doherty, C. M. Melliar-Smith and J. M. Poate, Thin Solid Film (in press).
3. W. K. Chu, J. W. Mayer, M-A. Nicolet, T. M. Buck, G. Amsel and F. Eisen, Thin Solid Film, 17, 1 (1973).
4. J. F. Ziegler and W. K. Chu, At. Data Nucl. Data Tables, 13, 463 (1974).
5. Z. L. Liau and T. T. Sheng, Appl. Phys. Lett. 32, 716 (1978).
6. T. T. Sheng and C. C. Chang, IEEE Trans. Electron. Devices ED-23, 531 (1976).

Chapter 4

PHENOMENOLOGICAL MODEL FOR ALLOY SPUTTERING

4.1 The Simple Model

In order to evaluate the experimental results in Chapter 3, we have developed a simple mathematical model to trace the formation kinetics of the Pt-enriched layer [1]. Similar models have been developed by several investigators [2,3].

The phenomenon of Pt-enrichment in the sputtered PtSi requires that:

Excess Pt atoms in the altered layer
= Excess Si atoms that have been sputtered off (4.1)

This can be expressed in mathematical terms as:

$$\int_0^\infty [n_{Pt}(\Phi, z) - n_{Si}(\Phi, z)]dz = \int_0^\Phi [S_{Si}(\Phi') - S_{Pt}(\Phi')]d\Phi' \qquad (4.1a)$$

where ϕ is the Ar dose per unit area; $n_{Si}(\phi,z)$ (or $n_{Pt}(\phi,z)$) is the density of Si (or Pt) atoms per unit volume as a function of the depth z; and $S_{Si}(\phi)$ (or $S_{Pt}(\phi)$) is the number of Si (or Pt) atoms being sputtered per incident Ar ion. The Pt/Si concentration ratio $n_{Pt}(\phi,z)/n_{Si}(\phi,z)$ has been measured for 80 keV Ar^{++} for three difference ϕ's (Fig. 3.2). We approximate the Pt-enrichment profiles, $n_{Pt}(\phi,z) - n_{Si}(\phi,z)$, by simple linear functions with a depth parameter, W, where $n_{Pt}(\phi,w) - n_{Si}(\phi,W) = 0$. Thus,

$$\int_0^\infty [n_{Pt}(\Phi,z) - n_{Si}(\Phi,z)]dz \cong \frac{1}{2}W[n_{Pt}(\Phi,0) - n_{Si}(\Phi,0)] \qquad (4.2)$$

$W \cong 750$ Å for 80 keV Ar^{++}. Smaller W's must be used for lower Ar energies (Fig. 3.7).

Substituting the righthand-side of Eq. (4.2) into the lefthand-side of Eq. (4.1a) and differentiating with respect to ϕ, we get

$$\frac{1}{2}W\frac{d}{d\Phi}[n_{Pt}(\Phi,0) - n_{Si}(\Phi,0)] = S_{Si}(\Phi) - S_{Pt}(\Phi) \qquad (4.1b)$$

This equation relates the change of surface composition to the preferential sputtering.

To deal with preferential sputtering, a parameter r is now introduced:

$$r \equiv \frac{\text{Si ejection probability}}{\text{Pt ejection probability}} \qquad (4.3)$$

Thus, preferential sputtering of Si over Pt implies $r > 1$. Since it is known that the sputtered atoms only emerge from the first few atomic layers, S_{Si} (or S_{Pt}) should be proportional to the surface concentration $n_{Si}(\phi,0)$ (or $n_{Pt}(\phi,0)$). Therefore, by the definition of r,

$$\frac{S_{Si}(\Phi)}{S_{Pt}(\Phi)} = r \cdot \frac{n_{Si}(\Phi,0)}{n_{Pt}(\Phi,0)} \qquad (4.3a)$$

In the beginning, more Si atoms are sputtered ($S_{Si} > S_{Pt}$). As the surface becomes Pt-enriched, the sputtering rate of Pt approaches that of Si. Finally, when the steady-state is approached, the Si and Pt atoms are sputtered at an equal rate, i.e., $S_{Pt}(\infty)=S_{Si}(\infty)$. Thus, Eq. (4.3a) gives

$$r = \frac{n_{Pt}(\infty,0)}{n_{Si}(\infty,0)} \qquad (4.3b)$$

which means that r can be determined from the steady-state surface composition. Specifically, $r \cong 1.94$ from Fig. 3.3.

The value of r is likely to be a function of the surface composition, i.e., $r = r\left(\frac{n_{Pt}(\phi,0)}{n_{Si}(\phi,0)}\right)$. However, experimental evidence indicates that r is only a slow-varying function of the surface composition. First of all, the data in Figs. 12 and 13 give $S_{Si}(0) = 2.4\ S_{Pt}(0)$, which implies $r\left(\frac{n_{Pt}(0,0)}{n_{Si}(0,0)} = 1\right) \cong 2.4$, by Eq. (4.3a). This is close to the previously determined saturation value, $r\left(\frac{n_{Pt}(\infty,0)}{n_{Si}(\infty,0)} = 2\right) = 1.94$. Furthermore, it was found that $r\left(\frac{n_{Pt}}{n_{Si}} = 3.3\right) = 1.7$ from sputtered Pt_2Si [4]. The fact that r is quite constant over a large range of surface compositions has also been reported by other investigators [3,5,6].

For convenience, we now define the following variables x and S:

$$x \equiv \frac{n_{Pt}(\Phi, 0)}{n_{Si}(\Phi, 0)} \tag{4.4}$$

$$S \equiv S_{Pt}(\Phi) + S_{Si}(\Phi) \tag{4.5}$$

Combining Eqs. (4.3a), (4.4) and (4.5), we get

$$S_{Si}(\Phi) = \frac{r}{r+x} S \tag{4.5a}$$

$$S_{Pt}(\Phi) = \frac{x}{r+x} S \tag{4.5b}$$

Similarly,

$$n_{Si}(\Phi, 0) = \frac{1}{1+x} n_o \tag{4.4a}$$

$$n_{Pt}(\Phi, 0) = \frac{x}{1+x} n_o \tag{4.4b}$$

where $n_0 \equiv n_{Si}(\phi,0) + n_{Pt}(\phi,0)$ is the total atomic concentration

which is nearly a constant, independent of ϕ.

With these new variables, Eq. (4.1b) becomes

$$\frac{1}{2} W n_0 \frac{d}{d\Phi}\left(\frac{x-1}{1+x}\right) = \frac{r-x}{r+x} S \tag{4.1c}$$

After differentiation, Eq. (4.1c) can be rearranged into

$$\frac{(r+x)}{(r-x)(1+x)^2} dx = \frac{1}{n_0 W} S d\Phi \tag{4.1d}$$

This differential equation relates the surface composition x to the ion dose ϕ, which can be solved by integration

$$\int_{x_0}^{x} \frac{(r+x')}{(r-x')(1+x')^2} dx' = \frac{1}{n_0 W} \int_0^{\Phi} S d\Phi' \tag{4.1e}$$

where x_0 is the initial surface composition ratio. ($x_0 = 1$ for PtSi.)

Since r was known to be a slowly varying function of x, we now approximate r as a constant, to simplify the calculation. The integration in the lefthand-side of Eq. (4.1e) can be carried out by taking partial fractions of the integrand. Thus,

$$\int_1^{x} \frac{(r+x')}{(r-x')(1+x')^2} dx' = \int_1^{x} \left[\frac{A}{(r-x')} + \frac{A}{(x'+1)} + \frac{B-A}{(x'+1)^2}\right] dx'$$

$$= A \ln \frac{x+1}{r-x} + \frac{A-B}{x+1} + C$$

where $A \equiv \frac{2r}{(r+1)^2}$, $B \equiv 1 - \frac{2}{(r+1)^2}$ and $C \equiv A\ln(\frac{r-1}{2}) + \frac{B-A}{2}$,

While the integral in the righthand-side of Eq. (4.1e) represents the total number of atoms sputtered, the calculation is simplified by approximating S as constant. (This approximation is somewhat justified by data in Figs. 3.11 and 3.12).

Hence, Eq. (4.1e) becomes

$$A \ln \frac{x+1}{r-x} + \frac{A-B}{x+1} + C = \frac{1}{n_0 W} S\Phi \qquad (4.1f)$$

With known n_0W, S and r, Eq. (4.1f) gives ϕ for each x. Upon inversion, the dependence of x on ϕ can be obtained.

To compare with experimentally measured $x(\phi)$ in Fig. 3.3, calculation of $x(\phi)$ was carried out for 80 keV Ar sputtering. The following values of n_0W, r and S (taken from Figs. 3.2, 3.3 and 3.11) were used: W = 750 Å (or $n_0W = 4.5\times10^{17}\text{cm}^{-2}$), r = 1.94, S = 4.0. The result is shown in Fig. 4.1. Good agreement with experimental values supports the present model. ($\frac{N_{Pt}}{N_{Si}}$ = x in Fig. 4.1).

To see how much sputtering is required to reach steady state, the rate of change of x near $\phi = 0$ is now considered. It follows from Eq. (4.1c) that,

$$\left(\frac{dx}{d\Phi}\right)_{\Phi=0} = \frac{S}{n_0 W} \frac{(r-x_0)(1+x_0)^2}{(r+x_0)} \qquad (4.6)$$

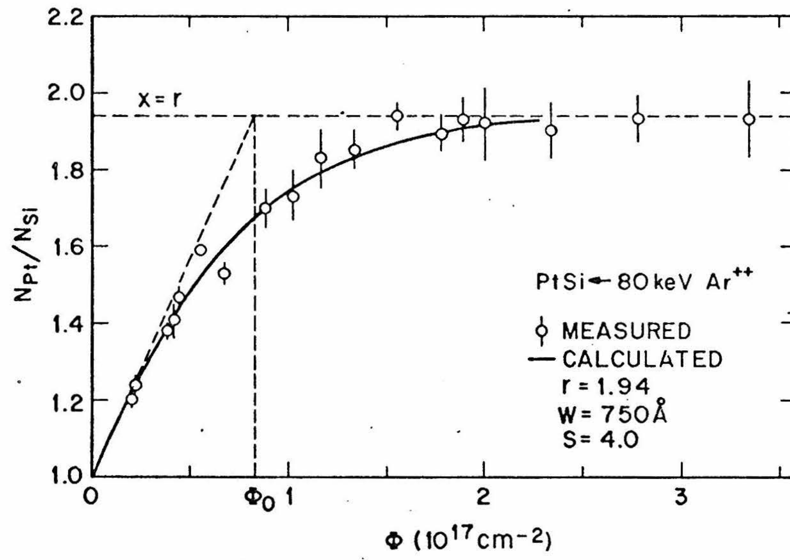

Figure 4.1 Comparison of calculated $x(\phi)$ with experiment. The data points are exactly the same as those in Fig. 3.3.

where $x_0 = 1$ for PtSi. The intersection of the initial tangent and $x = r$ defines ϕ_0 (see Fig. 4.1), which is a measure of the dose required to reach steady state. Thus,

$$\Phi \equiv \frac{r-1}{(dx/d\Phi)_{\Phi=0}} = \frac{n_0 W}{S} \cdot \frac{r+1}{4} \tag{4.7}$$

or

$$S\Phi_0 = n_0 W \frac{r+1}{4} \tag{4.7a}$$

For PtSi, $x_0 = 1.0$ and $r \cong 2.0$. Eq. (4.7a) becomes

$$S\Phi_0 = \frac{3}{4} n_0 W \tag{4.7b}$$

Since $S\phi_0$ represents the amount of material which has to be sputtered off to reach steady-state, Eq. (4.7b) implies that one has to sputter off an amount of material comparable to the thickness of the altered layer to reach the steady-state. This was indeed verified by experiment. As argon beams of lower and lower energies were used for sputtering, n_0W became smaller and smaller (Fig. 3.7). It was also found that less and less sputtering was required to reach steady-state. And the required sputtering was always to remove a thickness comparable to that of the altered layer.

So, this model seems to combine all experimental results into a

consistent picture. The main ideas in this model may also prove useful in other experiments concerning sputtering and atomic mixing. This will be the subjects of Chapters 5 and 6.

In the present model, we have approximated the profiles of Pt-enrichment as having a constant shape but with an amplitude changing with ion dose. This seems to be a fairly good approximation in the sputtering of PtSi. To have a better understanding of the composition profile, a more detailed calculation is carried out in the next section.

4.2 Calculation of Composition Profiles

In this section, the evolution of the composition profile is obtained as the solution of a partial differential equation (representing the atomic mixing process), which satisfies a boundary condition (characterizing the preferential sputtering). The applicability of this model to real problems is then discussed. This section is rather independent of other sections in this thesis and can almost be treated as an appendix.

4.2.1 Formulation

Consider a binary compound AB which is being sputtered by an incident inert-gas ion beam. Suppose the probability for a B-atom to be sputtered is greater than that for an A-atom. This preferential sputtering will cause a depletion of B-atom (or enrichment of

A-atoms) in a surface layer of thickness b, of few atomic layers, from which the sputtered atoms emerge. This composition change can propagate beyond b into a much deeper region of the sample if a diffusion mechanism is available.

Because of the sputter-etching, the sample surface is receding with a velocity v. For the convenience of mathematical description, we define a coordinate system, O, which is attached to the sample surface. Thus, O is a moving system (with velocity v) relative to the laboratory system O'. This is illustrated in Fig. 4.2. The depth profile of the composition change (or density of excess A-atoms) as measured in the moving system is defined as $n(x,t) \equiv n_A(x,t)-n_B(x,t)$. Since the sputtering process starts with a stoichiometric compound AB, we have $n(x,0) = 0$.

We further assume that the diffusion can be described by a simple diffusion equation with a constant diffusivity D, i.e.,

$$\frac{\partial}{\partial t} n(x',t) = D\frac{\partial^2}{\partial x'^2} n(x',t) \qquad (4.8)$$

in the laboratory system. Upon transformation, the equation becomes

$$\frac{\partial}{\partial t} n(x',t) = v\frac{\partial}{\partial x} n(x,t) + D\frac{\partial^2}{\partial x^2} n(x,t) \qquad (4.8a)$$

in the moving system.

Since the generation of excess A-atoms is due to the preferential

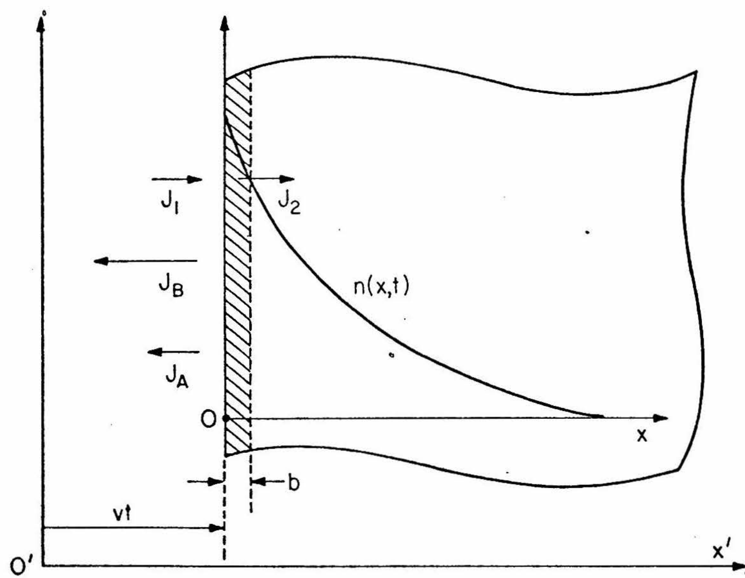

Figure 4.2 A schematic picture which shows the main ideas of the model for calculating the profile n(x,t) of the sputter-induced surface layer composition change.

sputtering which occurs in a thin surface layer, it can be considered as a boundary condition for n(x,t). To formulate the boundary condition, surface concentration, n(o,t), is now considered. Conservation of atoms requires:

$$b\frac{dn(0,t)}{dt} = \text{(Flux of excess A-atoms across the surface, at x=0, into the material)} - \text{(Flux of excess A-atoms across the interface, at x=b, into the material)}. \quad (4.9)$$

The first term on the righthand side of Eq. (4.9), which will be denoted as J_1, is due to sputtering. It can be considered as composed of two parts:

$$J_1 = (J_B - J_A) + n(0,t)\cdot v \quad (4.10)$$

The first term, (J_B-J_A), accounts for generation of excess A-atoms due to non-stoichiometric sputtering (i.e., when $J_B>J_A$). However, even when B- and A-atoms are sputtered at an equal rate (i.e., $J_B=J_A$), the existing excess A-atoms will be conserved and pushed back into the sample in accordance with the surface receding velocity. This is expressed as the second term, n(o,t) · v in Eq. (4.10).

The non-stoichiometric sputtering, (J_B-J_A), is also related to the surface composition, or n(o,t). The definition of r gives

$$\frac{J_B}{J_A} = r\cdot\frac{n_B(0,t)}{n_A(0,t)} \quad (4.11)$$

Based on this equation, the following approximation is made, to simplify the calculation,

$$J_B - J_A \cong v[\, r n_B(0,t) - n_A(0,t)\,] \qquad (4.12)$$

This equation can be re-arranged into

$$J_B - J_A \cong \frac{r+1}{2} v \left[\frac{r-1}{r+1} n_o - n(0,t) \right] \qquad (4.12a)$$

where n_o is the total atomic density.

The second term on the righthand side of Eq. (4.9), which will be denoted as J_2, is presumably due to diffusion:

$$J_2 = -D \left. \frac{\partial n(x,t)}{\partial x} \right|_{x=0^+} \qquad (4.13)$$

The derivative is taken at $x = 0^+$, based on the assumption that b is very small compared to the extent of the diffusion profile.

Combining Eqs. (4.10), (4.12a) and (4.13), one can re-write Eq. (4.9) as:

$$b \frac{dn(0,t)}{dt} = \frac{r+1}{2} v \left[\frac{r-1}{r+1} n_o - n(0,t) \right] + vn(0,t) + D \left. \frac{\partial n(x,t)}{\partial x} \right|_{x=0^+} \qquad (4.9a)$$

This equation takes the following form:

$$\frac{d}{dt} n(0,t) = A \left. \frac{\partial n(x,t)}{\partial x} \right|_{x=0^+} + Bn(0,t) + C \qquad (4.9b)$$

where $A \equiv D/b$, $B \equiv -(\frac{r-1}{2})\frac{v}{b}$ and $C \equiv (\frac{r-1}{2})\frac{n \cdot v}{b}$.

Equation (4.9b) will serve as a boundary condition for n(x,t). Therefore, the object of the present calculation is to solve the diffusion equation (Eq. (4.8a)) for n(x,t), subjected to the boundary condition (Eq. (4.9b)).

4.2.2 Solutions

(A) Steady-State

As the sputtering proceeds, n(x,t) will build up gradually because of the preferential sputtering (i.e., r>1 and $J_B > J_A$). However, as n(o,t) increases, J_A approaches J_B(cf. Eq. (4.11)). The generation of excess A-atoms will die out as $J_A = J_B$. This happens when

$$n(0,\infty) = \frac{r-1}{r+1} n_0 \tag{4.14}$$

which follows directly from Eq. (4.12a). (Equation (4.14) is equivalent to $\frac{n_A(o,\infty)}{n_B(o,\infty)} = r$, or $J_A = J_B$, by Eq. (4.11)). The fact that this happens as $t \to \infty$ will be verified later. There will, therefore, be no further changes of n(x,t). Equation (4.8a) becomes:

$$D\frac{d^2}{dx^2}n(x,\infty) + v\frac{d}{dx}n(x,\infty) = 0 \tag{4.8b}$$

For constant D throughout the material, this equation gives

$$n(x,\infty) = n(0,\infty)\, e^{-vx/D} \qquad (4.15)$$

Thus, the steady-state profile is an exponential function with its surface value given by Eq. (4.14). The profile is characterized by a length, L, defined as

$$L \equiv D/v \qquad (4.16)$$

The solution given by Eq. (4.15) is indeed consistent with the boundary condition.

(B) Solution for $o \leq t < \infty$.

To calculate n(x,t), a function, G(x,t-t'), is now introduced:

$$G(x,t-t') = \frac{e^{-[x+v(t-t')]^2/4D(t-t')}}{2\sqrt{\pi D(t-t')}} \qquad (4.17)$$

By direct substitution, it can be verified that G(x,t-t') satisfies Eq. (4.8a), i.e.,

$$\frac{\partial}{\partial t} G(x,t-t') = D\frac{\partial^2}{\partial x^2} G(x,t-t') + v\frac{\partial}{\partial x} G(x,t-t') \qquad (4.18)$$

for any t', with t'<t.

Then, a solution of n(x,t) of the following form is attempted:

$$n(x,t) = \int_0^t g(t')\,G(x,t-t')\,dt' \qquad (4.19)$$

For any given function g(t'), the corresponding n(x,t) satisfies Eq. (4.8a), because of Eq. (4.18), (and also because of the fact that Eq. (4.8a) is a linear differential equation).

For n(x,t) to satisfy the boundary condition, (Eq. (4.9b)), a special g(t') has to be chosen. By substituting n(x,t), as given by Eq. (4.19), into Eq. (4.9b), an equation for g(t') is obtained:

$$\int_0^t [g'(t')+Rg(t')]\frac{e^{-\frac{v^2}{4D}(t-t')}}{2\sqrt{\pi D(t-t')}}\,dt' + \frac{A}{2D}g(t) + g(0)\frac{e^{-\frac{v^2}{4D}t}}{2\sqrt{\pi D t}} - C = 0 \qquad (4.20)$$

where the coefficient R is defined as $R \equiv \frac{v}{2D}A-B$, and $g'(t') \equiv \frac{d}{dt'}g(t')$. Derivation of Eq. (4.20) is carried out in Appendix 4A.

Using Laplace transform, Eq. (4.19) can be solved for g(t). (See Appendix 4B.) The result is:

$$g(t)=\frac{n_0 v}{r+1}\left[r\cdot \mathrm{erf}\sqrt{\frac{v^2t}{4D}} - 1 - e^{-\frac{v^2t}{4D}}\left(A_1e^{\alpha_1 t}\,\mathrm{erfc}\sqrt{\alpha_1 t} + A_2e^{\alpha_2 t}\,\mathrm{erfc}\sqrt{\alpha_2 t}\right)\right] \qquad (4.21)$$

where $\alpha_1 \equiv \frac{v}{4L}\left[\frac{L}{b}(1+c)\right]^2$, $\quad \alpha_2 \equiv \frac{v}{4L}\left[\frac{L}{b}(1-c)\right]^2$,

$$A_1 = \frac{1+c}{c}\left[\frac{1}{2} + r\cdot\left(\frac{L}{b}\right)c\right], \qquad A_2 = \frac{1-c}{c}\left[\frac{1}{2} - r\cdot\left(\frac{L}{b}\right)c\right]$$

and $c = \sqrt{1 - 2r\cdot\left(\frac{b}{L}\right) + \left(\frac{b}{L}\right)^2}$.

Substituting g(t), as given by Eq. (4.21), into Eq. (4.19), the solution for n(x,t) is obtained.

(C) Asymptotic behavior

The function g(t), as given by Eq. (4.21), approaches a constant as t increases, i.e.,

$$\lim_{\frac{vt^2}{D}>>1} g(t) = \frac{r-1}{r+1} n_o v \tag{4.22}$$

where the asymptotic properties of error function [7] have been used, i.e., erfa $\cong$ 1 and erfca $\cong e^{-a^2}/\sqrt{\pi}a$ for a>>1. Notice that $n(o,\infty) = (\frac{r-1}{r+1})\, n_o$, by Eq. (4.14). Therefore,

$$\lim_{\frac{vt^2}{D}>>1} g(t) = n(0,\infty)\cdot v \tag{4.22a}$$

Based on Eq. (4.22a) and the property of G(x,t-t'), the asymptotic behavior of n(x,t) can be derived. Starting from Eq. (4.19), a change of variable is first carried out, i.e.,

$$\begin{aligned} n(x,t) &= \int_0^t g(t') \frac{e^{-[x+v(t-t')]^2/4D(t-t')}}{2\sqrt{\pi D(t-t')}} dt' \\ &= e^{-\frac{v}{2D}x} \int_0^t g(t-u) \frac{e^{-\left(\frac{x^2}{4Du} + \frac{v^2}{4D}u\right)}}{\sqrt{\pi D u}} du \end{aligned} \tag{4.19a}$$

where $u = t-t'$. Because we are interested in large t, (i.e., $\frac{v^2}{4D} t >> 1$), and $\frac{e^{-(\frac{x^2}{4Du} + \frac{v^2}{4D}u)}}{\sqrt{\pi D u}}$ drops to zero very fast as $\frac{v^2}{4D} \gtrsim 1$, g(t-u) in the integrand can be approximated as g(t), and can be taken out of the integral, i.e.,

$$n(x,t) \cong e^{-\frac{v}{2D}x} g(t) \int_0^t \frac{e^{-(\frac{x^2}{4Du} + \frac{v^2}{4D}u)}}{\sqrt{\pi D u}} du \qquad (4.19b)$$

Since $\frac{v^2}{4D}t >> 1$, g(t) approaches the value given by Eq. (4.22a). The upper limit of the integral can also be approximated as ∞, because the integrand drops to zero very fast for $\frac{v^2}{4D} >> 1$. Therefore, Eq. (4.19b) becomes,

$$n(x,t) \cong e^{-\frac{v}{2D}x} n(0,\infty)\cdot v \int_0^\infty \frac{e^{-(\frac{x^2}{4Du} + \frac{v^2}{4D}u)}}{\sqrt{\pi D u}} du \qquad (4.22c)$$

The integration can be carried out and yields $\frac{2}{v} e^{-\frac{v}{2D}x}$. Therefore,

$$n(x,t) \cong n(o,\infty)e^{-vx/D} \qquad (4.22d)$$

This asymptotic behavior is the same as the steady-state solution given by Eq. (4.15).

(D) Numerical values

To plot n(x,t), a computer calculation has been carried out to evaluate g(t), using Eq. (4.21). Then, n(x,t) is obtained by direct substitution of g(t) into Eq. (4.19) and by carrying out the integration numerically.

In addition to variables x and t, there are parameters v, b, r, D and L, which have to be specified. They can be re-arranged in Eqs. (4.21) and (4.19), such that n(x,t) takes the following form:

$$n(x,t) = n(\frac{x}{L}, \frac{vt}{L}, \frac{b}{L}, r)$$

where the parameter D has been eliminated by using Eq. (4.16).

Figure 4.3 shows calculated g(t) for $r = 2$ and $\frac{b}{L} = \frac{1}{50}$. The function g(t) rises from zero and reaches a maximum value, when $\frac{vt}{L} \cong \frac{b}{L}$. From then on, it decreases monotonically and, when $\frac{vt}{L} \gtrsim 2$, approaches an asymptotic value of $\frac{v}{2}n(o,\infty)$. Figure 4.4 shows the corresponding n(x,t), for a sequence of t.

The surface value of the profiles, n(o,t) is an interesting quantity. It can also be calculated from Eq. (4.21) with g(t) given by Fig. 4.3. The result is shown in Fig. 4.5. The function n(o,t) builds up nearly parabolically for small t and then approaches the steady-state value, $n(o,\infty)$, when $\frac{vt}{L} \gtrsim 2$.

The results shown in Figs. 4.3, 4.4 and 4.5 are obtained for r=2 and $\frac{b}{L} = \frac{1}{50}$. To see how the magnitude of b affects the results, calculations have been carried out for $\frac{b}{L} = \frac{1}{25}$, $\frac{1}{50}$ and $\frac{1}{100}$. It was found that the situation is rather insensitive to this variation of $\frac{b}{L}$. The results showed that the difference between the n(o,t)'s was ~10% for $0.01 < \frac{vt}{L} < 0.1$. This difference decreases further to within ~1% for $0.1 \leq \frac{vt}{L} < 1.0$.

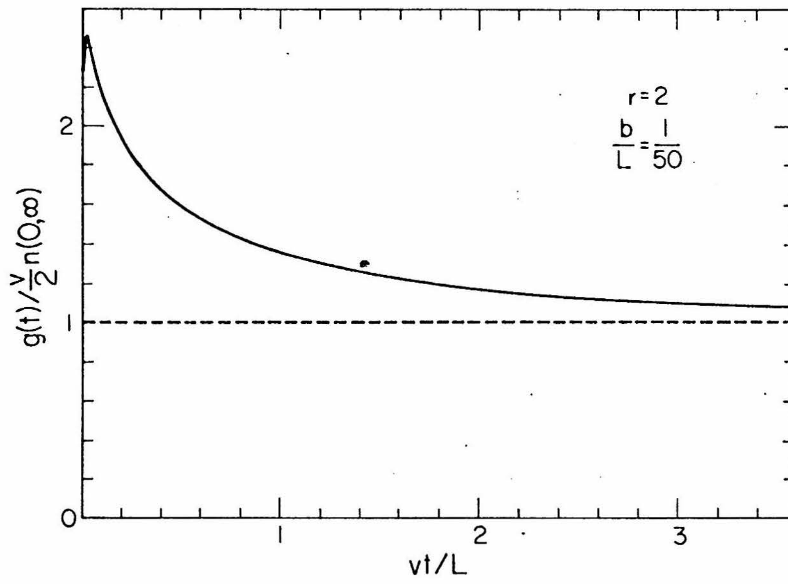

Fig. 4.3 An example of calculated g(t).

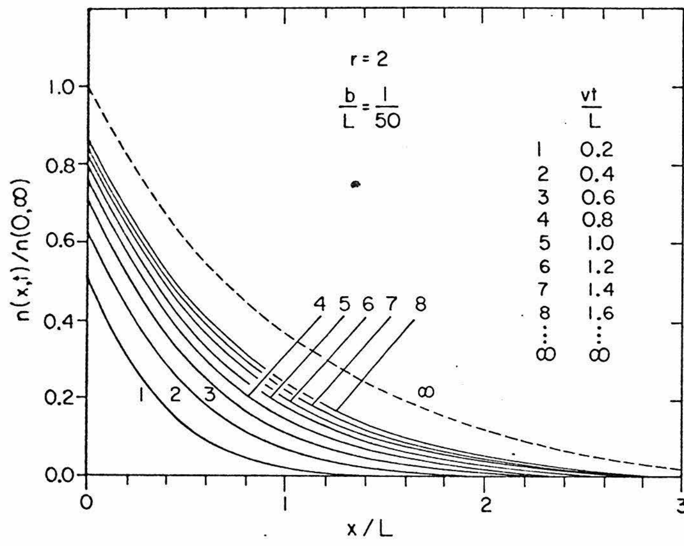

Figure 4.4 Calculated n(x,t) for r=2 and b=L/50.

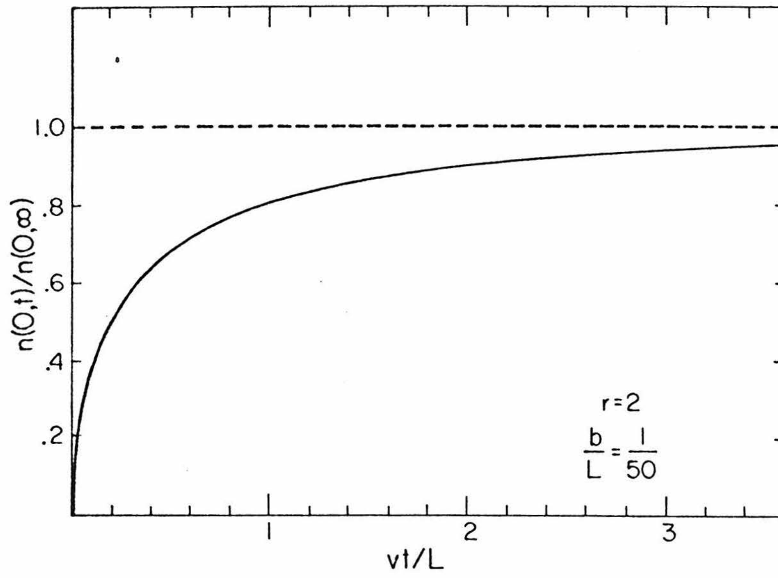

Figure 4.5 Calculated n(o,t) for r=2 and b=L/50.

4.2.3 Discussion

Based on the diffusion equation (Eq. (4.8a)) and boundary condition (Eq. 4.9a)), n(x,t) is obtained by pure mathematical deductions. Because of the number of calculation steps involved, it is desirable to check the solutions by substituting it back into the original equations (especially Eq. (4.9a)). This has been carried out numerically. Values of quantities which appeared in Eq. (4.9a) were obtained from plots like Figs. 4.4 and 4.5. Equation (4.9a) was found to be satisfied, to within computational accuracy, for all t.

In addition to assumptions that have been made in obtaining Eqs. (4.8a) and (4.9a), n(x,t) has been obtained for the idealized case of a constant diffusivity which extends to infinite depth into the material. Such an idealization can be a good approximation to the reality in some cases. There, however, can also be cases where significant deviations occur.

It has been demonstrated in some experiments that the ion-induced atomic mixing extends only to a finite depth, W, which corresponds to the range of the incident ion. The effective diffusivity is likely related to both the material properties and atomic collisions (triggered by the incident ion). If the effective diffusivity is small such that $L \lesssim W$, the assumption of a constant diffusivity (throughout the material) will be less un-realistic, because the diffusion profiles will never reach the depth where diffusivity vanishes. Experimentally, such small diffusivity may be observed for amorphous materials with

intrinsically low diffusivity (such as SiO_2) and for sputtering using light ions (therefore less collisions to promote atomic mixing).

On the other hand, if the effective diffusivity is so large that $L \gtrsim W$, the assumption of constant diffusivity extending to infinite depth will have significant deviation from the real situation. In the extreme case of $L \gg W$, the profile will penetrate all the way to W in the very beginning of the sputtering process. Therefore, instead of the picture shown in Fig. 4.4, $n(x,t)$ will always extend to constant depth W, while its amplitude (as represented by $n(o,t)$) increases with t. This will cause $n(o,t)$ to build up linearly (instead of parabolically in Fig. 4.5) in the beginning of the sputtering process. This picture seems to be in better agreement with the experimentally observed profiles in the sputtering of PtSi [1].

Attempt has not been made to calculate $n(x,t)$, taking general depth-dependence of the diffusivity into consideration. The steady-state solution is, however, much easier to obtain because only an ordinary differential equation (i.e., Eq. (4.8b)) needs to be solved. To illustrate this point, we now consider a simple case where a constant diffusivity extends to a depth W and drops abruptly to zero beyond W, as shown in Fig. (4.6a). The steady-state solution is the same as Eq. (4.15) except that $n(x,\infty) = 0$ for $x > W$, as shown in Fig. 4.6b. To check the consistency of the solution with physical consideration, the situation is observed from the laboratory coordinate system, as illustrated in Fig. 4.6c. The steady-state profile moves with

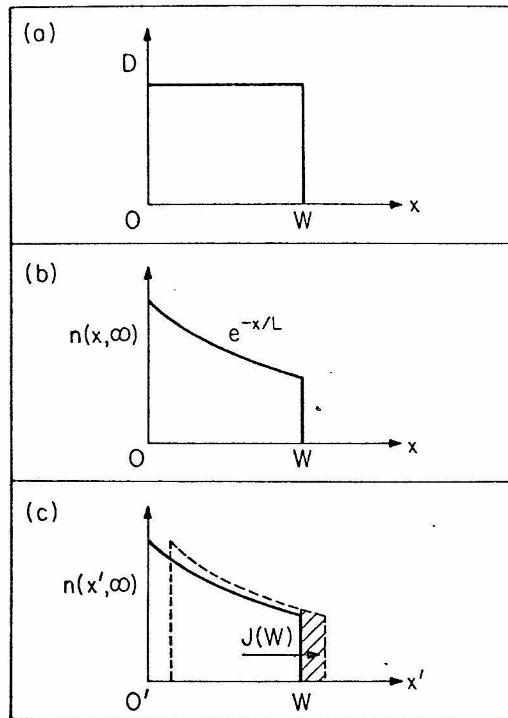

Figure 4.6 Steady-state profile $n(x,\infty)$ for a system in which diffusivity is non-zero only for $0 < x < W$.

velocity, v, without change in shape. Such a steady-state movement is, however, due to diffusion (and a moving boundary condition). New area created at the moving front (the shaded region in Fig. 4.6c) has to be supplied by diffusion flux, J(W). The rate of increase of the shaded area is $n(W) \cdot v$, while the diffusion flux is J(W) $= - D\frac{dn}{dx}\Big|_{x=W^-}$ which is then equal to $\frac{D}{L}n(W)$ or $v \cdot n(W)$. Therefore, the solution shown in Fig. 4.6(b) is consistent with the physical consideration.

The calculated n(o,t), in Fig. 4.5, shows that n(o,t) approaches within 20% of the steady-state value when $\frac{vt}{L} \gtrsim 2$. This implies that one has to sputter off roughly the thickness of the (steady-state) altered surface layer (which is characterized by L in the present case) to reach the steady state. This rule has been found to be rather generally applicable including those cases where the thickness is characterized by W rather than L.

References

1. Z. L. Liau, J. W. Mayer, W. L. Brown and J. M. Poate, J. Appl. Phys. (in press).

2. H. F. Winters and J. W. Coburn, Appl. Phys. Lett. 28, 176 (1976).

3. P. S. Ho, J. E. Lewis, H. S. Wildman and J. K. Howard, Surf. Sci. 57, 393 (1976).

4. Z. L. Liau, W. L. Brown, R. Homer and J. M. Poate, Appl. Phys. Lett. 30, 626 (1977).

5. H. Shimizu, M. Ono and K. Nakayama, Surf. Sci. 36, 817 (1973).

6. We measured r for the Au-enrichment in sputtered Au_xAg alloys. The value of r changed from 1.22 to 1.15 as x varied from 0.04 to 1.0.

7. F. Reif, Fundamentals of Statistical and Thermal Physics, (McGraw-Hill, New York, 1965) p. 610.

8. F. B. Hildebrand, Advanced Calculus for Applications, (Prentice-Hall, New Jersey, 1962) Chapter 2.

9. M. R. Spiegel, Mathematical Handbook of Formulas and Tables, (McGraw-Hill, New York, 1968) p. 167.

Chapter 5

HIGH-DOSE ION IMPLANTATION

5.1 Introduction

As mentioned in Chapter 1, sputtering phenomena become important in high-dose ion implantation. Since atoms of both kinds (i.e., the host material and the implanted species) get sputtered, preferential sputtering must be considered. The atomic mixing phenomena associated with heavy-ion bombardment will also play a decisive role in determining the formation kinetics of the implanted surface layer. Other effects such as compound formation and precipitation are often important in high-dose implantation. In this chapter, we ignore the possible precipitations and consider only the effects of preferential sputtering and atomic mixing. A model similar to that developed in Section 4.1 is invoked to predict the limits of achievable compositions and the formation kinetics of the surface layer. Some experimental results show good agreement with the predictions.

5.2 Maximum Attainable Concentrations

In general, the maximum concentration attainable by ion implantation is given by the reciprocal of the sputtering yield. This occurs because of the receding of sample surface (due to sputter-erosion) or, equivalently, the sputter-removal of the implanted species. This maximum concentration is obtained after the sputtering of a thickness comparable to the ion range.

However, more careful consideration should be given if there

is preferential sputtering between atoms of host material and those of the implanted species. There is also an interesting variation when one implants ion species A into a compound AB.

The steady-state surface concentrations are relatively easy to obtain. Let us first consider the implantation of ion species A into host material B. Let N_A and N_B be the concentrations (per unit volume) of A-atoms and B-atoms, respectively, at the surface of the sample. Therefore, $\frac{N_A}{N_B}$ represents the steady-state surface composition. Let J_A and J_B be the flux of sputtered atomic species A and B, respectively. Then, we have

$$\frac{J_B}{J_A} = r \cdot \frac{N_B}{N_A} \tag{5.1}$$

where r is the ratio of the probability for a B-atom near the surface to be sputtered to that of such an A-atom. Therefore, Eq. (5.1) has exactly the same meaning as Eq. (4.3a). Now, define the flux of incident ions of species A as J_i; and the total sputtering yield S as

$$(J_A + J_B) = S J_i \tag{5.2}$$

At steady-state, there is no change of the total number of A-atoms in the material, therefore,

$$J_A = J_i \tag{5.3}$$

Combining Eqs. (5.2) and (5.3), we get

$$J_B = (S - 1) J_i \tag{5.4}$$

Substituting J_A and J_B, as given by Eqs. (5.3) and (5.4), into Eq. (5.1), we get

$$\frac{N_A}{N_B} = r \cdot \frac{1}{S - 1} \tag{5.5}$$

This is the steady-state surface composition. Note that it is roughly inversely proportional to the total sputtering yield S, but multiplied by the preferential sputtering factor r. For r = 1, Eq. (5.5) gives $\frac{N_A}{N_B + N_A} = \frac{1}{S}$, as expected.

Since it has been demonstrated that sputtering-induced composition change is independent of ion species used for sputtering, the preferential sputtering ratio, r, which appears in Eq. (5.1) should be the same as that measured from the inert gas ion sputtering of alloy AB.

As a further illustration of this technique, let us now consider the case of implantation of atomic species A into the alloy AB. The situations are nearly the same as the previous example, except that we now have an alloy AB to begin with, which sets a different boundary condition at the steady-state. Instead of $J_A = J_i$ (Eq. (5.3)), we now have:

$$J_A - J_B = J_i \qquad (5.6)$$

at steady-state. The total sputtering yield is still defined in the same way as in Eq. (5.2). The relation expressed in Eq. (5.1) still holds. Thus, combining Eqs. (5.6) and (5.2), we have

$$J_A = \frac{S+1}{2} J_i \qquad (5.7a)$$

$$J_B = \frac{S+1}{2} J_i \qquad (5.7b)$$

Substituting J_A and J_B into Eq. (5.1), we get

$$\frac{N_A}{N_B} = r \cdot \frac{S+1}{S-1} \qquad (5.8)$$

This gives the steady-state surface composition.

When S >> 1, Eq. (5.8) reduces to $\frac{N_A}{N_B} = r$, which is the same result as inert gas ion sputtering of alloy AB as described in Chapter 2. On a physical basis, this is because, with high sputtering yield S, a very little amount of implanted atoms can stay in the material. Equation (5.8) will be discussed in greater detail in Section (5.5).

5.3 Evolution of the Implanted Concentration

In the previous section, the steady-state surface composition was considered. To see how the steady state is reached, one has to look into the depth profile of the implanted species. At high doses, the depth profiles will appear different than those of low dose implants, because of sputtering, atomic mixing and possible precipitate formation, etc. Some recent experiments have provided measurements of high-dose profiles [1-5].

In the present section, we shall again ignore the possibility of precipitation and consider a simple model for the dose dependence of the implanted concentration. We shall assume that atomic mixing is very efficient such that the implanted species spreads out rather uniformly over an effective width W, after an initial amount of implantation, say $\sim 10^{16} cm^{-2}$. After that, we assume the shape of the profile remains approximately unchanged, but with its amplitude increasing with further implantation. This is illustrated in Fig. 5.1. With such an idealization, the evolution of implanted concentration can be obtained by simple calculations. The basic ideas are very similar to the model developed in Section 4.1 for the sputtering of an alloy.

The conservation of atoms requires:

$$W \frac{dN_A}{dt} = J_i - J_A \tag{5.9}$$

where N_A is the atomic concentration of the implanted species, J_i is the flux of incident ions (of species A) and J_A is the flux of the sputtered A-atoms.

The relations between J_A, J_B and J_i are the same as given in the previous section (Eqs. (5.1) and (5.2)). If the implanted concentration is less than 30 atomic %, S should not change very significantly. (The data in Fig. 3.12 also indicate that $S = S_{Si} + S_{Pt}$ remains approximately constant for a change in composition from PtSi to Pt_2Si.) Therefore, we shall approximate S as a constant throughout the implantation process. Define the variable $x \equiv \frac{N_A}{N_B}$. Then, Eqs. (5.1) and (5.2) give

$$J_A = \frac{x}{r+x} S J_i \tag{5.10a}$$

$$J_B = \frac{r}{r+x} S J_i \tag{5.10b}$$

Substituting Eqs. (5.10a) into Eq. (5.9), we get

$$W \frac{d}{dt} \frac{x}{1+x} N_o = J_i - \frac{x}{r+x} S J_i \tag{5.11}$$

where again $N_o = N_A + N_B$. After some re-arrangement Eq. (5.11) becomes

$$\frac{r+x}{(1+x)^2 \left[r + (1-S) x \right]} dx = \frac{d\Phi_A}{N_o W} \tag{5.12}$$

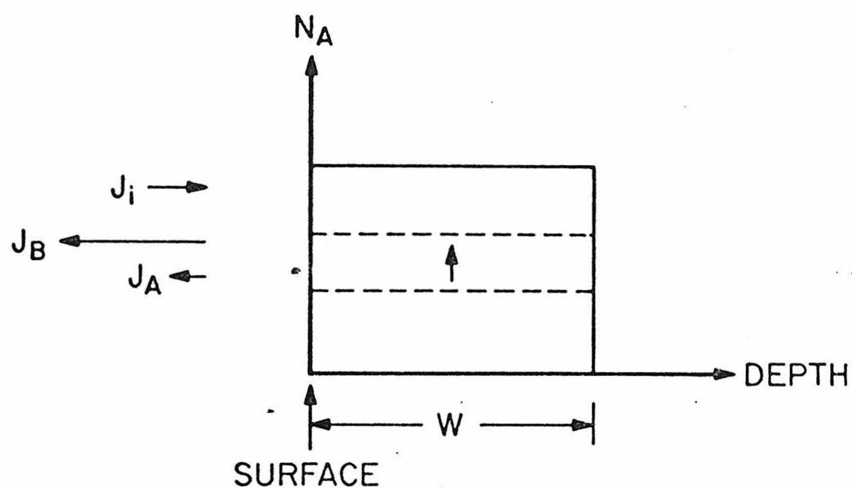

Figure 5.1 A model for the buildup of implanted concentration as a function of implantation dose. Assuming a very efficient atomic mixing, this model approximates the implanted profile as having a constant shape, but with an increasing applitude. The rate of increase of implanted concentration is due to the difference between the flux of incident ions of species A, J_i, and that of the sputtered particles of species A, J_A.

where $d\phi_A \equiv J_i dt$ = incremental ion dose. Equation (5.12) is a differential equation for $x(\phi_A)$, which can be solved by taking the partial fractions for the lefthand-side and integrating. The result is:

$$S\left[\frac{Ax}{1+x} + B\ln\frac{1+x}{1-\frac{x}{x(\infty)}}\right] = \frac{S\Phi_A}{N_o W} \qquad (5.13)$$

where $A \equiv \frac{r-1}{r-(1-S)}$, $B = \frac{Sr}{[(1-S)-r]^2}$ and $x(\infty) = r/(S-1)$.

Note that $\frac{S\phi_A}{N_o W}$ can be interpreted as the amount of material sputtered as measured by the thickness of the implanted layer.

An example of the calculated $x(\phi_A)$ is given in Fig. 5.2. The steady-state compositions are the same as predicted by Eq. (5.5), i.e., $\frac{N_A}{N_B} = r \cdot \frac{1}{S-1}$. Note that, for $r = 2$, it takes about twice as much sputtering to reach the steady-state composition. This can also be seen by the following derivation: Define

$$\Phi_o \equiv \frac{x(\infty)}{(dx/d\Phi_A)_{\Phi_A=0}} \qquad (5.14)$$

which is a measure of the dose required to reach steady-state. (See dashed lines in Fig. 5.2).

Equation (5.12) gives

$$\left.\frac{dx}{d\Phi_A}\right|_{\Phi_A=0} = \frac{1}{N_o W} \qquad (5.15)$$

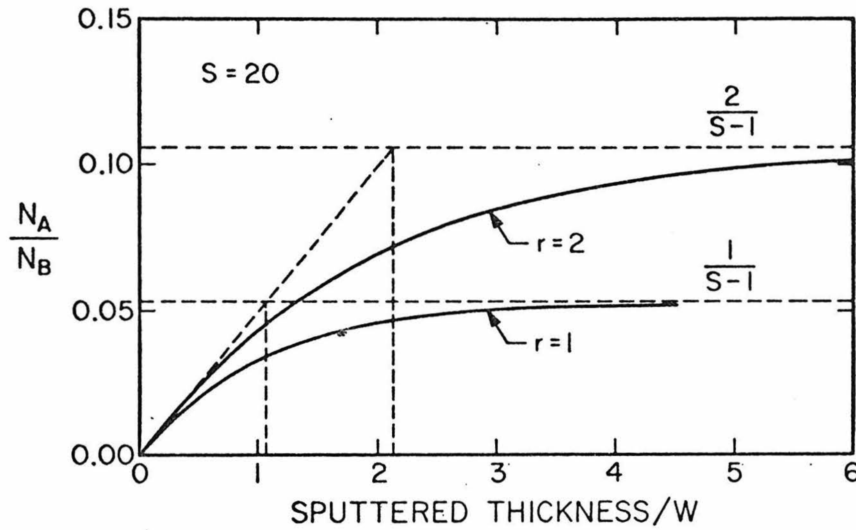

Figure 5.2 Buildup of implanted concentration calculated from the simple model of Fig. 5.1. To illustrate the effects, examples with $S = 20$ and $r = 1$ or 2 are considered. With a preferential sputtering of the target material ($r = 2$), a correspondingly higher implanted concentration can be achieved. The curves are calculated from Eq. (5.13).

Since $x(\infty) = r \cdot \frac{1}{S - 1}$, Eqs. (5.14) and (5.15) give

$$(S-1)\Phi_o = r \cdot N_o W \tag{5.16}$$

For $S \gg 1$, Eq. (5.16) becomes

$$\frac{S\Phi_o}{N_o W} \cong r \tag{5.17a}$$

This implies that one has to sputter an amount of material, which is r times the thickness W, to reach the steady state.

5.4 Examples

As examples of how the model can be applied, we show some experimental data. Figure 5.3 shows backscattering spectra of a Cu-film implanted with 150 keV Au [6]. The Au-profiles can be approximated as having a constant shape, but with amplitude increasing with dose. The effective width, W, is measured from the Au-profiles such that, (Au peak concentration) $\cdot$ W = (total amount of Au). In the present case, W is thus measured to be 414 Å. (Note that R_p and ΔR_p calculated from LSS theory [7] are 185 Å and 68 Å, respectively). The sputtering yield as measured from the data like those in Fig. 5.3 is S = 20. The preferential sputtering parameter r as obtained from alloy sputtering data (Table 2.1) is 1.1.

Figure 5.4 plots data points of surface composition versus

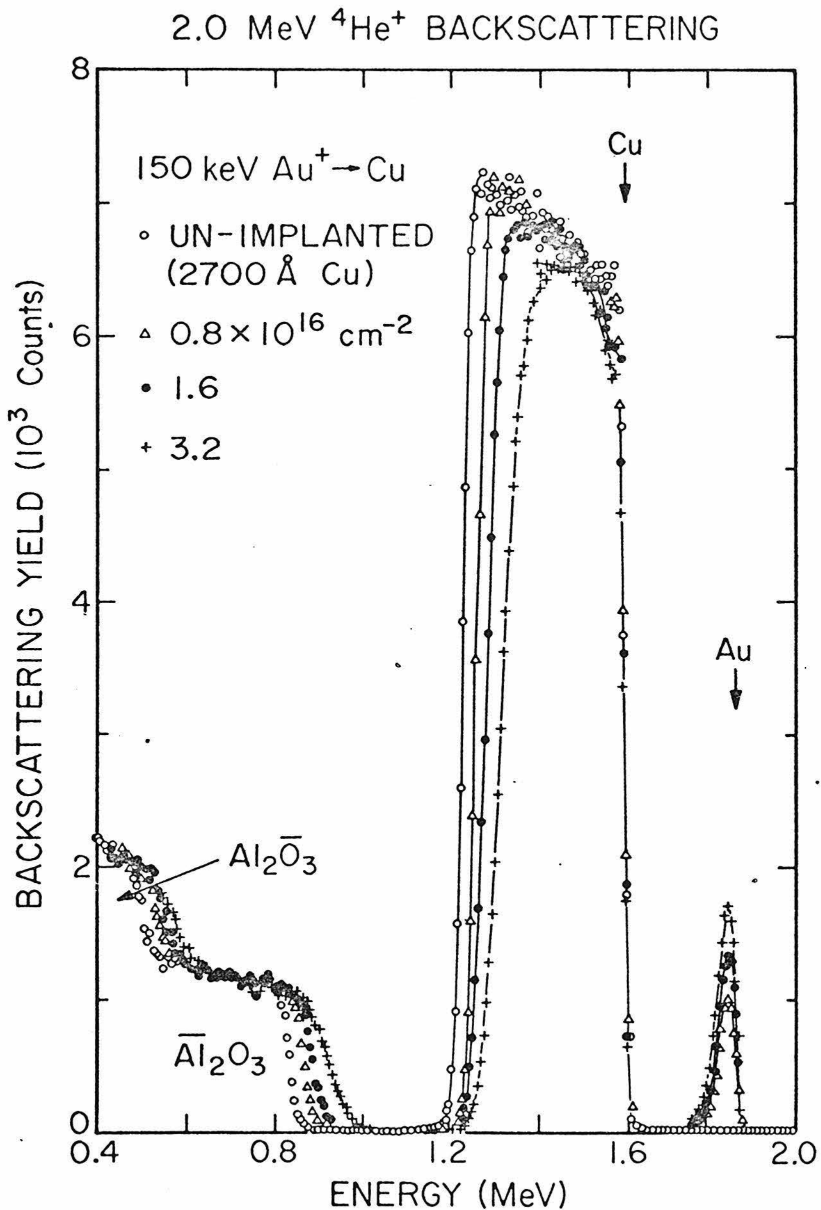

Figure 5.3 High-dose implantation of Au into a thin film of Cu. The backscattering spectra show that the Cu-film becomes thinner because of sputtering. Note that the buildup of the Au concentration is not linear with dose of Au ions.

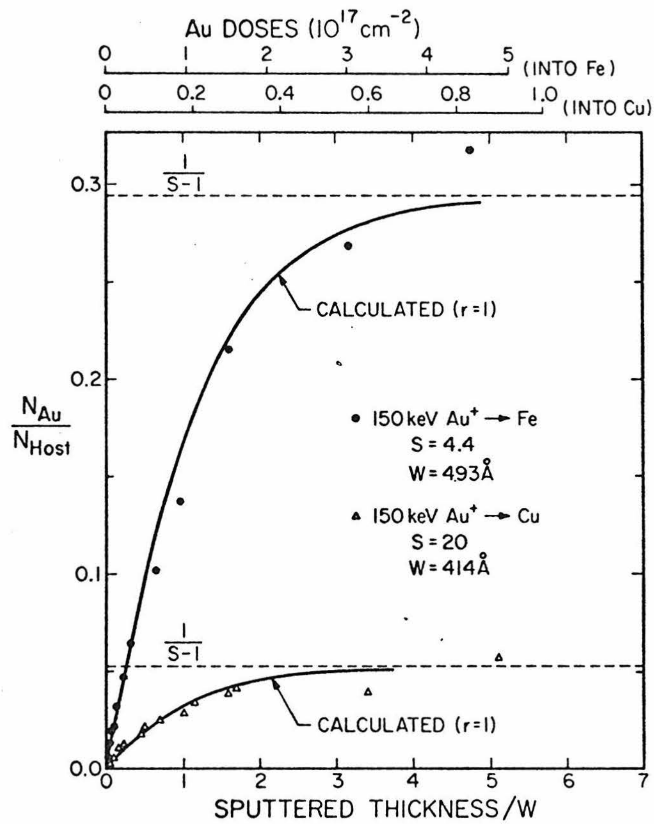

Figure 5.4 Buildup of Au concentrations in the high-dose implantation of Au into Cu and Fe. The Au-concentration in Cu shows a saturation which is much lower than that in Fe. This is because of higher sputtering yield of Cu. The curves are calculated from Eq. (5.13) by assuming $r = 1$.

sputtered thickness [8]. The solid line is calculated from the model. The agreement between experimental data and the calculation seems to be good.

The same Au-implantation was carried out on Fe thin-film samples [6]. Backscattering data give $S = 4.4$ and $W = 493$ Å. However, there are no data available for r. Since $r = 1.1$ for the Au-Cu system, we shall try $r = 1$ for the present case. Figure 5.4 shows the comparison between the calculation and the experimental results. Note that the maximum of N_{Au}/N_{Fe} is around 0.3. It is substantially higher than that of the Au-Cu system, where the maximum N_{Au}/N_{Cu} is ~0.05. This is mainly because of the difference in sputtering yields.

Figure 5.5 shows the results from Cu-films implanted with 150 keV Ta^+ [8]. These data show some peculiar features. First of all, the sputtering yield is around 13. This is different from the case of 150 keV Au^+ on Cu where $S = 20$. However, based on the collision cascade picture of sputtering, the effect of 150 keV Ta^+ should be nearly the same as that of 150 keV Au^+. (This is because there is only ~8% difference between the masses of Au and Ta.) The observed difference in sputtering yields seems significant. Secondly, the maximum N_{Ta}/N_{Cu} is as high as 0.25, which can be explained only with $r = 3$. Such an r value of preferential sputtering is higher than all other systems that have been studied. (See Table 2.1).

Another explanation for $r = 3$ is the formation of a thin oxide layer at sample surface during implantation. This thin oxide can

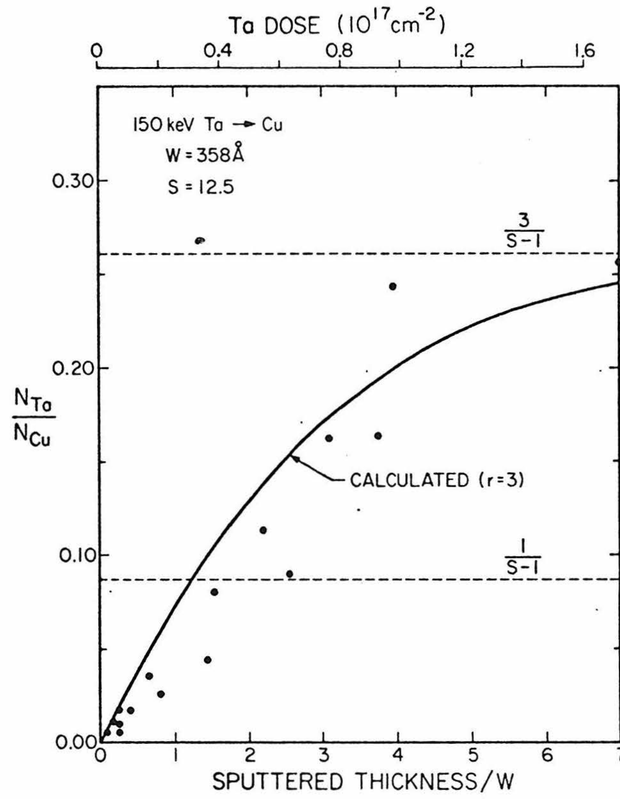

Figure 5.5 Buildup of Ta concentration in the high-dose implantation of Ta into Cu. The implanted Ta concentration is significantly higher than $\frac{1}{S}$ and corresponds to $r = 3$ when treated by the simple model (Eq. (5.13)).

lower the sputtering yield (due to change of surface binding energy). There can also be some segregation phenomenon [9], which may make the Ta-atoms preferentially stay away from the surface oxide layer. Therefore, fewer Ta atoms appear in the near surface region to be sputtered. This can effectively give rise to the observed value of r.

Since Ta showed very low solubility in Cu [10], high-dose implantation can possibly result in fine precipitates of Ta [11]. Because elemental Ta has very low sputtering yield, the precipitation of Ta can also lead to the high apparent value of r.

5.5 Prediction of Steady-State Concentrations

In the present section, examples will be presented to illustrate how the results of the previous sections can be used to predict maximum implant concentrations. Since the sputtering of Pt-Si system has been studied in great detail (Chapters 3 and 4), implantations in the Pt-Si system will be considered.

Consider a Si sample implanted with 45 keV Pt^+. While there is no direct measurement of the sputtering yield of this system, an approximate value can be obtained by some extrapolations. First of all, measurements of sputtering yields give S(45 keV Pt → Si)/S(45 keV Ar → Si) = 3.0 and S(45 keV Ar → Si) = 1.5 [12-14]. Therefore, S(45 keV Pt → Si) ≅ 1.5 x 3.0 = 4.5.

The parameter r is now defined by $\frac{J_{Si}}{J_{Pt}} = r\frac{N_{Si}}{N_{Pt}}$ (Eq. (5.1)), and has been measured to be $\simeq$ 2 in the Ar-sputtering of PtSi. With S $\simeq$ 4.5 and r $\simeq$ 2.0, Eq. (5.5) predicts the steady-state surface Pt concentration ratio to be $\frac{N_{Pt}}{N_{Si}} = 2 \cdot \frac{1}{4.5-1} = 0.57$, or, a Pt concentration of $\frac{N_{Pt}}{N_{Si} + N_{Pt}} = 26\%$.

To calculate the Pt dose required to reach this maximum concentration, the parameter W should be considered. The calculated R_p (projected range) and ΔR_p (projected standard deviation) of 45 keV Au in Si are 230 Å and 60 Å, respectively [7]. Since the mass of Pt is so close to that of Au, their ranges should also be very close. Furthermore, by approximating W as $R_p + \Delta R_p$, W is estimated to be 290 Å for 45 keV Pt in Si. To reach ~90% of the steady-state concentration, a thickness of ~4W, or 1160 Å, has to be sputtered. This thickness corresponds to 5.8×10^{17} atoms/cm^2 (based on an atomic density of $5.0 \times 10^{22} cm^{-3}$ for Si). With a sputtering yield of 4.5, a Pt-dose of $1.3 \times 10^{17} cm^2$ is required.

For an interesting comparison, the implantation of 45 keV Si into Pt is now considered. Again, the sputtering yield has to be obtained by extrapolation . First, the sputtering yield of Pt by 20 keV Ar^+ has been measured to be 4.1 [14]. The data presented in Ref. 13 gives S(45 keV Ar → Au)/S(20 keV Ar → Au) = 1.1. This energy dependence can be used to estimate S(45 keV Ar → Pt) to be + 4.5. (Because the masses of Au and Pt are very close, the collision cascades in Au and Pt should be approximately the same for the same ion

incidences. Therefore, the sputterings of Au and Pt should be the same except for the difference in the surface binding energies. In particular, for the same incident ion, the sputtering yields of Au and Pt should follow the same energy dependence.) On the other hand, Ref. 13 also gives S (45 keV Si $\rightarrow$ Au)/S(45 keV Ar $\rightarrow$ Au) = 0.67. Hence, the sputtering yield of Pt by 45 keV Si is estimated to be 4.5 x 0.67, or 3.0. (Here the similarity between the sputtering of Au and Pt has been applied once more.)

The parameter r is now defined by $\frac{J_{Pt}}{J_{Si}} = r\frac{N_{Pt}}{N_{Si}}$ and is approximately $\frac{1}{2}$. With S = 3.0 and r = $\frac{1}{2}$, Eq. (5.5) then predicts the maximum surface Si-concentration to be $\frac{N_{Si}}{N_{Pt}} = \frac{1}{2} \cdot \frac{1}{3.0 - 1} = 0.25$, or a Si concentration of $\frac{N_{Si}}{N_{Pt} + N_{Si}} = 20\%$.

To estimate the Si-dose required to reach the maximum concentration, again, $W \cong R_p + \Delta R_p$ is used. The calculated R_p and ΔR_p are 164 Å and 158 Å, respectively (for 45 keV Si in Au) [7]. To achieve 90% of the maximum Si concentration, a sputter-removal of a thickness W, or 322 Å, is required. This thickness corresponds to 2.1 x 10^{17} atoms/cm^2 (based on an atomic density of 6.6 x 10^{22}cm^{-3} for Pt). With a sputtering yield of 3.0, a Si-dose of 0.7 x 10^{17}cm^{-2} is necessary.

The discussions about the two implantations, (I) Pt $\rightarrow$ Si and (II) Si $\rightarrow$ Pt, are summarized in Table 5.1. It is interesting to briefly compare these two cases: The sputtering yield of Case I is higher than that of Case II. However, because of the difference in

TABLE 5.1

COMPARISON OF TWO ION-IMPLANTATIONS (45 keV)

	Pt → Si	Si → Pt
Sputtering yield, S	4.5	3.0
Preferential sputtering	2	$\frac{1}{2}$
Maximum implanted concentration	36 at. %	20 at. %
Implanted layer thickness, W	290 Å	322 Å
Material sputtered to reach ~90% of maximum concentration	1160 Å	322 Å
Dose required	$1.3 \times 10^{17}/cm^2$	$0.7 \times 10^{17}/cm^2$

r-values, Case I can achieve higher implanted concentration than Case II. For the same reason, it also takes much more sputtering for Case I to reach its maximum concentration.

As a final example in this section, the implantation of Si into PtSi is now considered. One might anticipate that implantation of Si could result in a Si-rich Pt-Si mixture. However, instead of increasing the Si-concentration, the Si-implantation may even decrease the Si-content in the PtSi sample, because of the preferential sputtering of Si. The composition in the implanted sample will be determined by a competition between implantation and sputtering.

The steady-state surface composition is given by Eq. (5.8), i.e., $\frac{N_{Si}}{N_{Pt}} = r \cdot \frac{S + 1}{S - 1}$, with $r \cong \frac{1}{2}$. The surface compsition is, therefore, dependent upon the total sputtering yield, S. This dependence is plotted in Fig. 5.6. For $S > 3$, the implanted PtSi sample becomes depleted of Si, because S is sufficiently large so that not enough implanted Si-atoms can stay in the sample to overcome the preferential sputtering of Si. For $S = 3$, the Si-implanted PtSi sample remains PtSi. For $S < 3$, more implanted Si-atoms stay in and the sample becomes Si-enriched.

Since the variation of S can be achieved experimentally, by varying the incident angle of the ion-beam in Si-implantation or by varying the Si beam energy, the prediction described in Fig. 5.6 can be tested experimentally.

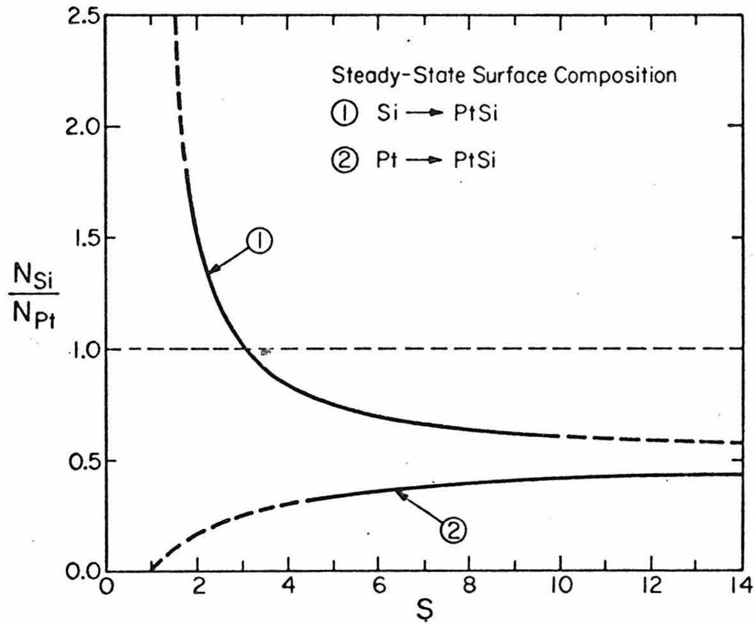

Figure 5.6 Predictions of high-dose implantations of Si and Pt into PtSi. Note that the implantation of Si into the PtSi sample will result in a depletion of Si, if the total sputtering yield, S, is higher than 3. This is because of preferential sputtering of Si. The composition is determined by a competition between implantation and sputtering (Eq. (5.8)).

5.6 <u>Other Effects Which Influence High-Dose Ion-Implantation</u>

Since the majority of sputtered atoms are of relatively low energies and emerge from the first few atomic layers near the surface, sputtering is sensitive to surface conditions. In fact, a thin layer of surface contaminants or oxide can effectively protect the material from being sputtered, and therefore, strongly affect the parameters S and r, which in turn determine the state of the immplanted materials.

The surface conditions are influenced by several factors, such as residual gas in the vacuum, target material and the current density of the incident ion beam. For example, it is well known that ion-implantation in a bad vacuum can cause the formation of a carbon layer on the sample surface. Formation of thin oxide layers are often encountered in the sputtering of easily-oxidized materials. Good vacuum and high ion-beam current (high sputtering rate) are often desirable to minimize surface oxidation.

Both carbon and oxide layers can greatly reduce the sputtering yield of the material. This can significantly increase the maximum implanted concentration. This effect has been experimentally demonstrated in the implantation of Cu into Al [15]. Anomalously high implanted Cu concentrations (comparable to that of Cu_2Al) were observed when low Cu^+ beam current densities were used or when oxygen was deliberately sprayed onto the sample during implantation. Such high concentrations were not observed when high current densities of

Cu^+ beam were used or when nitrogen was sprayed onto the sample.

The surface oxide layer can also affect the preferential sputtering parameter r, because of the segregation effects of oxides similar to those observed in SiO_2 [9]. This effect has already been discussed at the end of Section 5.4.

It might appear desirable to have surface oxide and carbon layers intentionally to enhance the implant concentration. However, because of atomic mixing, the surface oxygen and carbon can be mixed into the implanted layer after the prolonged implantation. Significant side-effects can be caused by these impurities. Effects of bombardment-induced oxygen incorporation have been demonstrated in a recent experiment, in which 20 keV Xe^+ implantation of Si was carried out at elevated oxygen pressure [16]. With oxygen pressures up to $\sim 1 \times 10^{-6}$ Torr, the sputtering yield can drop by as much as a factor of 5. After a Xe^+ dose of $\sim 10^{17} cm^2$, oxygen was observed in the sample over a depth comparable to the implanted Xe distribution. The oxygen concentrations were a few atomic %. The Xe-retention in the sample was also found to be related to the oxygen incorporation.

Sputtering can also give rise to surface roughness, which can possibly affect the high-dose implantation. The surface roughness has been found to be related to crystallographic orientation, impurities in the material, ion species and angles used for sputtering. It has been demonstrated that an extremely rough surface can reduce the sputtering yield by as much as two orders of magnitude [17].

Gas bubble formation and blistering effect have been widely observed in high-dose implantations of inert gas ions [18]. Back-scattering measurement of depth distributions often showed very low concentrations of implanted species in the near surface region [1,4,19]. This indicates that the inert gas atoms can escape from the material even without sputtering. In these cases, one cannot apply the simple model described in the previous sections.

5.7 Conclusion

Sputtering by inert gas ion generally induces composition changes in alloys and compounds. Based on these results, one can predict maximum attainable concentrations for high-dose ion-implantation. A rough estimate of the concentration ratio of implanted species to target atoms is given by r/S where r is the preferential sputtering parameter and S is the sputtering yield. With generally observed values of S and r, it is relatively easy to obtain impurity concentrations $\lesssim 10$ atomic % by ion-implantation. But, unless S is low, it is very hard to obtain concentrations higher than ~ 30 atomic %. As one alternative, one can start with a composition near that of the desired end product. In this case, implantation is used both to change the composition of a surface layer and also to introduce the atomic mixing and non-equilibrium conditions that are often desired when dealing with implantation metallurgy. As another alternative, one can deposit a layer of material A on substrate B. Then the atomic mixing that occurs during ion bombardment can lead to a mixture of A and B.

References

1. P. Blank, K. Wittmaack and F. Schulz, Nucl. Inst. Meth. 132, 387 (1976).

2. J. S. Williams, Phys. Letters, 51A, 85 (1975).

3. C. E. Christodoulides, W. A. Grant and J. S. Williams, Nucl. Inst. Meth. 149, 219 (1978).

4. K. Wittmaack and P. Blank, Appl. Phys. Lett. 31, 21 (1977).

5. R. E. J. Watkins and G. Dearnaley, (private communication).

6. J. K. Hirvonen, J. M. Poate, Z. L. Liau and J. W. Mayer, paper presented at International Conference of Ion Beam Material Modification, Budapest, Sept., 1978.

7. Z. L. Liau, J. W. Mayer, J. K. Hirvonen and J. M. Poate, (unpublished).

8. J. F. Gibbons, W. S. Johnson and S. W. Mylroie, "Projected Range Statistics", 2nd ed., (Halsted Press, 1975).

9. A. S. Grove, Physics and Technology of Semiconductor Devices, (Wiley, New York, 1967), p. 70.

10. M. Hansen, Constitution of Binary Alloys, 2nd ed. (McGraw-Hill, New York, 1958).

11. A. G. Cullis, J. A. Borders, J. K. Hirvonen and J. M. Poate, (to be published).

12. H. H. Andersen and H. L. Bay, Rad. Eff. 19, 139.

13. H. H. Andersen, in Physics of Ionized Gases, V. Vujnovic, ed., (Inst. of Phys., Univ. Zagreb, Yugoslavia, 1974).

14. J. M. Poate, W. L. Brown, R. Homer, W. M. Augustyniak, J. W. Mayer, K. N. Tu and W. F. van der Weg, Nucl. Inst. Meth. 132, 345 (1976).

15. E. Arminen, A. Fontell and V. K. Lindroos, Phys. Stat. Sol(a) 4, 663 (1971).

16. W. Wach and K. Wittmaack, Nucl. Inst. Meth. 149, 259 (1978).

17. J. F. Ziegler, J. J. Cuomo and J. Roth, Appl. Phys. Lett. 30, 268 (1977).

18. See, for example, G. Dearnaley, J. H. Freeman, R. S. Nelson and J. Stephen, Ion Implantation, (North-Holland Publishing Company, Amsterdam, 1973).

19. Z. L. Liau and T. T. Sheng, Appl. Phys. Lett. 32, 716 (1978).

Chapter 6

EVOLUTION OF SURFACE LAYERS DURING SPUTTER-ETCHING

6.1 Introduction

In Chapters 2 and 3, an ion-induced atomic mixing effect was introduced to account for the observed thicknesses of the altered surface layers in sputtered alloys and compounds. Based on this idea of atomic mixing over the ion range, one can predict many other interesting effects. For example, there will be some "impurity-dragging" in sputter-etching: Suppose there are some impurity atoms in a solid surface. As sputter-etching proceeds, the ion range will gradually reach deeper regions of the material. Consequently, the atomic mixing effect can also continuously mix the impurity atoms into those deeper regions (Fig. 6.1). Therefore, the impurity atoms can appear being "dragged" along with the marching front of the implanted ion profile. Because of this effect, the impurity atoms can never be completely cleaned by sputter-etching. Since there is sputtering at surface as well as atomic mixing over the ion range, the simple model developed in Chapter 4 can be used in the present case to calculate the evolution of the impurity concentration. The situation is illustrated in Fig. 6.1.

In this chapter, we report the experiments which have demonstrated this effect. The sample used for sputtering was a Pt-film

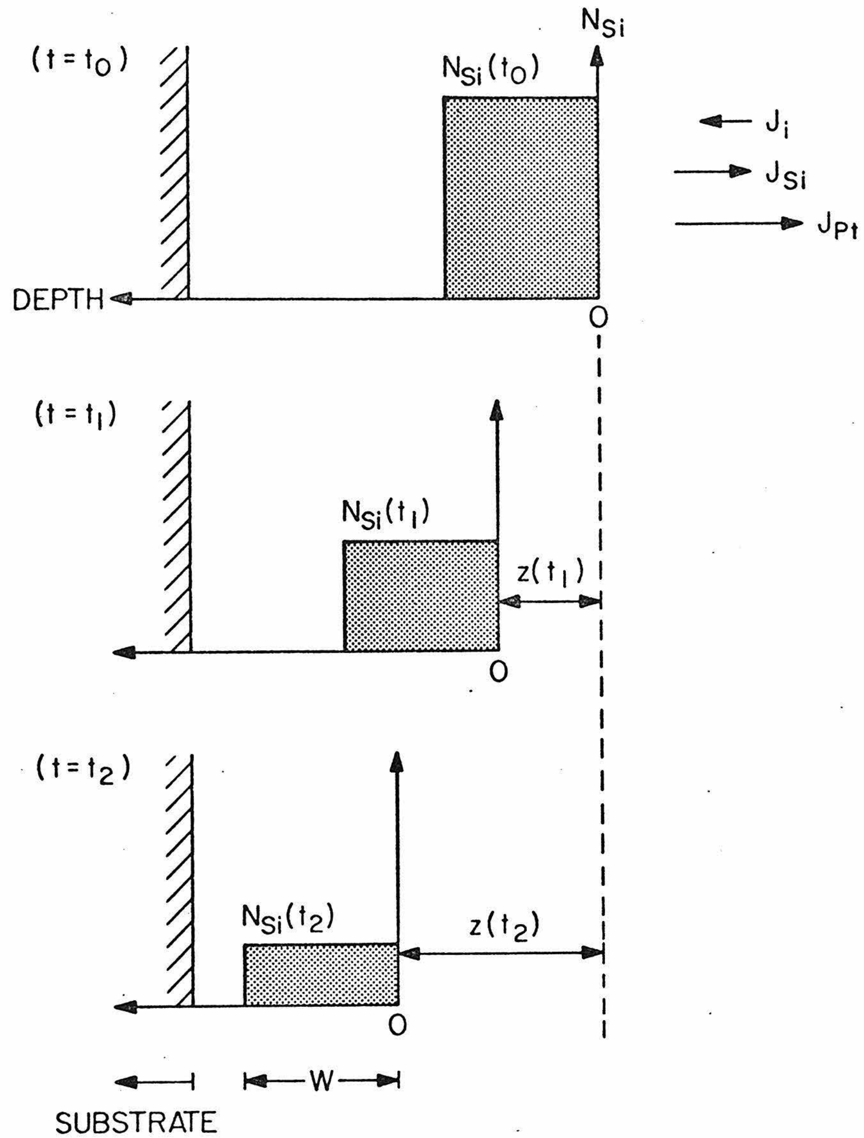

Figure 6.1 An illustration of the model for the evolution of surface Si-concentration during sputtering. The main idea is the sputter-removal of Si- and Pt-atoms at surface and the redistribution of the remaining Si-atoms over a constant depth.

which contains a surface layer of Pt-Si mixture. We observed that the surface layer maintained a constant thickness (instead of being thinned by sputtering), but with a decreasing Si-concentration. Similar phenomenon was also observed for an Au-Al surface layer on top of an Al-film. The measured Si-concentrations in the sputtered Pt-Si samples were in good agreement with the predictions of a model derived from the one in Section 4.1.

In fact, similar phenomena have also been reported by numerous investigators [1-4]. The present findings have interesting implications which will be discussed in Section 6.4. We also generalize the present model to calculate the influence of atomic mixing and preferential sputtering on sputter-depth-profiling techniques (Section 6.5).

6.2 Experimental Procedures

Thin-film structure with a Si layer (380 Å) sandwiched between an underlying Pt layer (1800 Å) and another surface layer of Pt (100 Å) was prepared by sequential depositions of Pt and Si onto a clean Si wafer. The depositions were carried out by using electron-gun evaporations at rates of ~30 Å/sec in a vacuum better than 1×10^{-6} Torr. Similar sample preparation was carried out for the Al-Au system.

The samples (originally of 1 cm x 1 cm) were then cut into smaller pieces, each of 2 mm x 4 mm, for ion-beam experiments.

Sputtering using rare-gas ions of 100-300 keV was carried out in an ion-implantation accelerator with an average beam current of ~5μA/cm^2 and a vacuum better than 6 x 10^{-7} Torr (during sputtering). Ion doses between 3 x 10^{15} and 2.2 x 10^{17} cm^{-2} were used. The samples were then analyzed with Rutherford backscattering technique using 2.0 MeV (or 1.5 MeV in some cases) $^4He^+$ beam from a van de Graaff accelerator. The beam spot was 1 mm x 1 mm.

6.3 Results

Figure 6.2 shows backscattering spectra of an unsputtered Pt-Si sample and two sputtered ones. Both sputtered samples show surface layers of Pt-Si mixtures of nearly the same thickness (~ 1000 Å). The (near) surface compositions as determined from the corresponding Pt and Si signal heights [(5)] are $PtSi_{0.66}$ and $PtSi_{0.29}$ for the low- and high-Xe^+-dose samples, respectively. The number of Pt- and Si-atoms in the samples are determined from the normalized integrated counts of the Pt- and Si-signals [(5)]. The amount of material that has been sputter-removed can thus be determined from the change in the numbers of Pt- and Si-atoms in the sputtered sample. This and the surface composition have been measured for each of the samples sputtered with 250 keV Xe^+ to doses between 3 and 20 x 10^{15}cm^{-2}. The results are shown as the data points in Fig. 6.3. The sputtered thicknesses are obtained by assuming a constant atomic concentration of 6 x 10^{22}cm^{-3} for all Pt-Si mixtures. The parameter W is defined as the effective

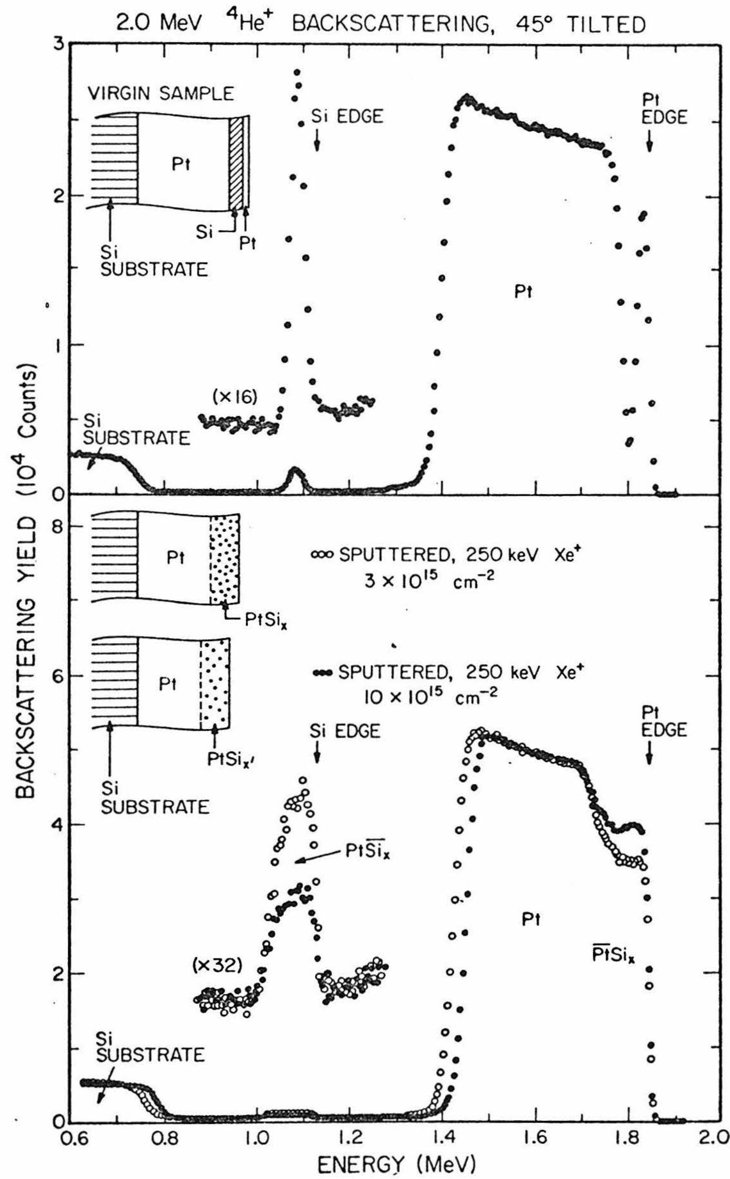

Figure 6.2 Backscattering spectra of unsputtered and sputtered Pt-Si samples which show the evolution of a surface layer during sputtering.

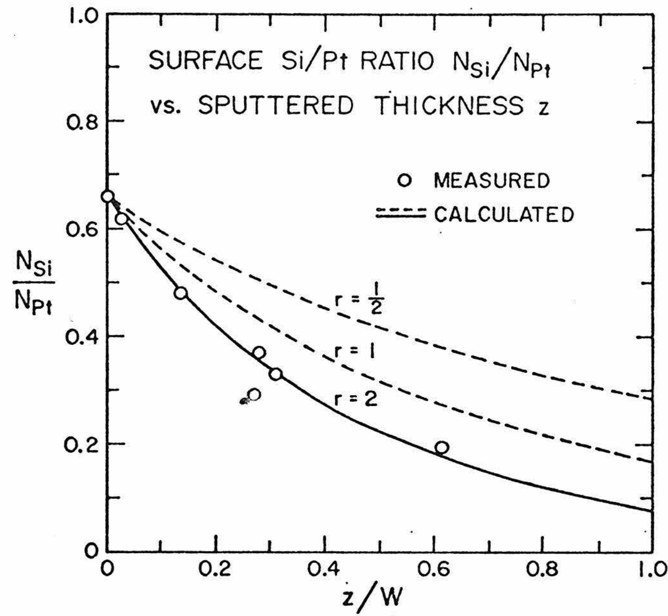

Figure 6.3 Surface Si/Pt concentration ratio as a function of the amount of material which has been sputter-removed. The curves are given by Eq. (6.6) which is derived from the model sketched in Fig. 6.1.

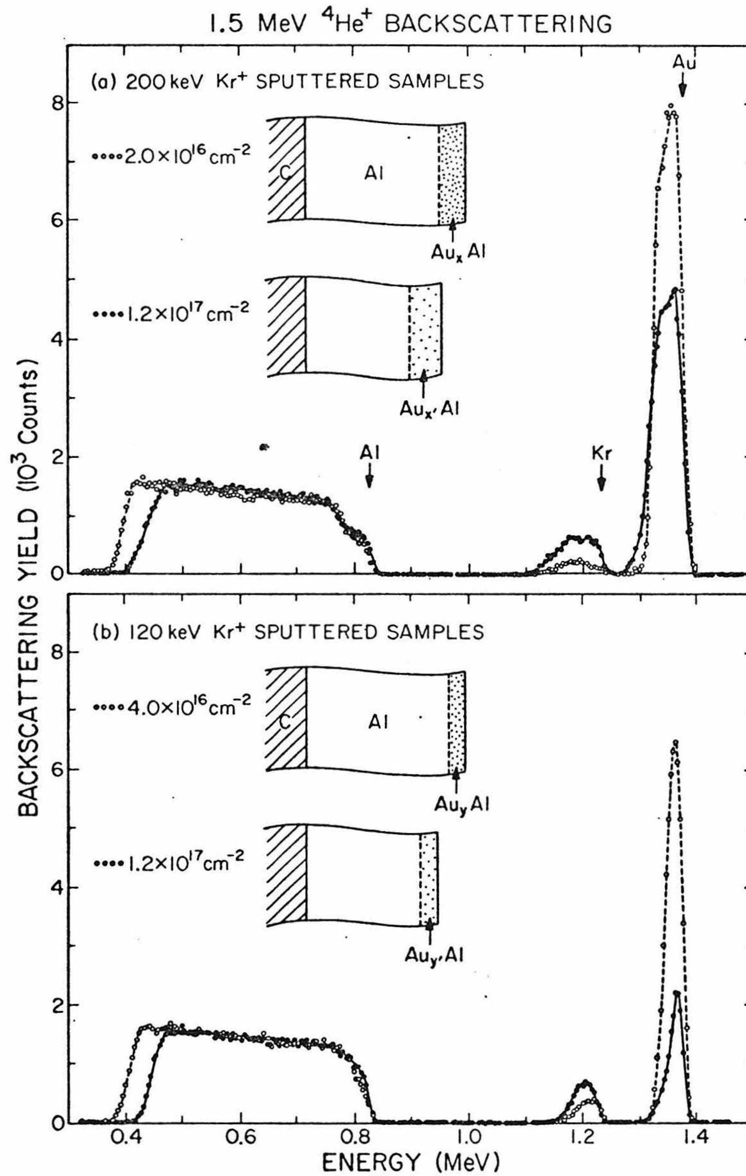

Figure 6.4 Backscattering spectra of sputtered Al-Au samples which show the evolution of surface layers during sputtering. For each Kr^+ energy, the surface Au-Al-intermixed layer maintains a nearly constant thickness, which is comparable to the implanted Kr distribution.

thickness of the surface layer, i.e., W ≡ (Total number of Si-atoms in the layer)/(Surface concentration of Si). The W's thus determined for all Xe^+-doses were nearly a constant and could be represented by W = 700 ± 30Å.

Results similar to those of Pt-Si samples were also obtained for Al-Au samples. Figure 6.4 shows two examples. In these cases, a Kr^+-dose of 3 x $10^{15}cm^{-2}$ was sufficient to produce a uniform surface layer of Al-Au mixture with a thickness comparable to the ion range. Appreciable amounts of sputtering were observed for doses of 10^{16} and $10^{17}cm^{-2}$. The Au-distribution was observed to extend to nearly a constant depth, while the Au-concentration decreased with the ion dose.

6.4 The Simple Model

The present results are interpreted as due to the sputter-removal of Pt- and Si-atoms (or Al- and Au-atoms) at surface and the redistribution of the remaining Si- (or Au-) atoms over a constant depth which is comparable to the ion range. This rather "efficient" redistribution is consistent with the observation that atomic mixing over the ion range was achieved at much lower ion doses than those required to sputter-remove the same thickness. Based on this interpretation, a simple model is developed to calculate the Si-concentration as a function of sputtering. This model takes into consideration the preferential sputtering of Si-atoms at surface and is quite similar to the one previously developed for the sputtering of PtSi [5].

Figure 6.1 illustrates the main idea of this model. The conservation of Si-atoms requires

$$W \cdot \frac{dN_{Si}}{dt} = -J_{Si} \tag{6.1}$$

where N_{Si} is the density of Si-atoms (per unit volume) in the surface layer, t is the sputtering time and J_{Si} is the magnitude of the flux of the sputtered Si-atoms. J_{Si} is related to the incident ion flux J_i and the total sputtering yield S, i.e.,

$$J_{Si} + J_{Pt} = SJ_i \tag{6.2}$$

where J_{Pt} is the flux of sputtered Pt-atoms. J_{Si} is also related to the surface Si-concentration N_{Si} and

$$\frac{J_{Si}}{J_{Pt}} = r \cdot \frac{N_{Si}}{N_{Pt}} \tag{6.3}$$

where N_{Pt} is the surface Pt-concentration and r is the preferential sputtering factor [5].

Equations (6.1), (6.2) and (6.3) can then be combined to obtain the evolution of N_{Si} during the sputtering process. For convenience, we define $x \equiv N_{Si}/N_{Pt}$ and $N_0 \equiv N_{Si} + N_{Pt}$, which then give $N_{Si} = N_0x/(1 + x)$. Equations (6.2) and (6.3) then yield $J_{Si}=SJ_i \cdot rx/(rx + 1)$. By using these new expressions for N_{Si} and J_{Si} and by assuming N_0 as a

constant, Eq. (6.1) becomes

$$N_0 W \frac{d}{dt}\left(\frac{x}{1+x}\right) = -\frac{rx}{rx+1} S J_i \qquad (6.4)$$

After some re-arrangements Eq. (6.4) becomes

$$\int_{x(0)}^{x(t)} \frac{(rx'+1)}{rx'(1+x')^2} dx' = \frac{1}{N_0 W}\int_0^t S J_i dt \qquad (6.5)$$

By assuming r as a constant, the integration on the lefthand-side of Eq. (6.5) can be carried out by taking the partial fractions of the integrand. The integral on the righthand-side of Eq. (6.5) represents the total amount of material sputtered per unit area, up to time t. Therefore, $\frac{1}{N_0}\int_0^t SJ_i dt$ is the sputtered thickness which will be denoted as z(t), as in Figs. 6.1 and 6.3. Equation (6.5) then becomes

$$\left[\frac{r-1}{x+1} + \ell n\left(\frac{x}{x+1}\right)\right]_{x(0)}^{x} = -\frac{z}{W/r} \qquad (6.6)$$

Equation (6.6) gives z(x), which yields x (z) upon inversion. The calculated x(z) for r = 1/2, 1 and 2 are plotted in Fig. 6.3, which shows that r = 2 yields better agreement with experiment. This is consistent with previous results (Chapters 3 and 4) on the sputtering of PtSi which showed a preferential sputtering of Si with $r \cong 2$.

For $x(0) << 1$, Eq. (6.6) can be simplified to be

$$x = x(0)\, e^{-z/(W/r)} \tag{6.7}$$

6.5 Discussions

In the present work, we have shown that the atomic mixing indeed occurs over depths comparable to the ion range (Fig. 6.4). Both types of samples showed the mixing process to be very "efficient", because relatively low ion doses were required. For example, Fig. 6.2 shows that a Xe^+-dose lower than $3 \times 10^{15} cm^{-2}$ was sufficient to mix $\sim 4 \times 10^{17} cm^{-2}$ of Pt- and Si-atoms. The fact that the interface between the Pt-film and Si-substrate stays sharp in Fig. 1 is consistent with the observation that atomic mixing occurs only over a depth comparable to the ion range. It is also an indication that no appreciable overall sample heating (due to ion-bombardment) was involved in the mixing process, because Pt_2Si formation occurs at $\sim 250^oC$ [6,7]. The atomic mixing phenomenon has implications in many related experiments. For example, thin-film materials of any desirable composition can possibly be produced by first depositing discrete layers of elemental materials followed by bombardment with a heavy ion beam of a suitable energy. We suggested that this method might have the capability of producing materials with compositions and structures unattainable by conventional metallurgical means [8]. In fact, this

has gained supporting evidences from recent experimental results [9].

Another consequence of this "efficient" atomic mixing process is the phenomenon depicted in this chapter. More precisely, since the ion doses needed to produce a uniformly mixed layer over a thickness comparable to the ion range were substantially lower than those required to sputter-etch the same thickness, one would expect substantial redistributions of alloying (or impurity) atoms during the sputtering process. The analyzing techniques used in the present experiments provide direct measurement of sputter-etching, which showed that Si (or Au) was indeed distributed over a nearly constant depth, regardless of the sputter-etching. Thus, with sputtering at surface and atomic mixing over the ion range, the alloying atoms will maintain a constant depth, but with a decreasing concentration. The agreement between the measured and calculated Si-concentrations seems to support the idea of the model which was first proposed for the formation kinetics of the sputter-induced composition changes [5].

The simple model in this paper predicts that the concentration of the impurity atoms will eventually die down exponentially with a decay length of W/r (Eq. (6.7)). This implies that surface impurities can never be completely cleaned, no matter how much sputter-etching has been done. Since W is comparable to the ion range, the impurity atoms can be more efficiently cleaned with a lower energy ion beam. Fig. 6.4 shows that W is indeed comparable to the implanted ion distribution and that Au-concentration decreases faster for smaller W.

The dependence of W on the ion energy has been clearly demonstrated for a wide range of ion energies in Chapter 3.

Besides sputter-cleaning, the same problems should be considered in depth-profiling techniques which employ sputtering for material sectioning. Because of atomic mixing, the depth profiles can appear different from the real ones. For example, an impurity distribution can appear broader and with an apparent long tail proportional to the ion energy used for sputtering. This has been demonstrated by previous investigators [3,4]. A similar situation has been found when sputtering through an interface of thin films.[10] We applied the ideas of the model developed in Section 6.4 to calculate the apparent depth profiles due to atomic mixing and preferential sputtering. (See Section 6.6). In that calculation we have ignored other effects [11,12] (such as sputter-induced surface roughening) which can also cause the apparent profile-broadening.

A further application of the present results is in the high-dose ion implantation for material modifications. To achieve implanted concentrations greater than a few atomic percent, ion doses higher than 10^{17} cm^{-2} are required. Therefore, atomic mixing and sputtering can affect the implanted ion distributions. We again applied the simple model to calculate the implanted concentration [8]. Preliminary experimental results [13] with 150 keV Au^+ implantations into Cu and Fe showed good agreements with the calculations [8].

Although similar phenomena were observed in both Pt-Si and Al-Au

systems used in the present work, we do not know whether the picture depicted in this chapter is indeed a universal phenomenon. Although there are other evidences which indicate that this phenomenon is quite general (Chapter 2), there may be some systems which are more "difficult" for ion-induced atomic mixing. For example, much less ion-induced interfacial reactions were observed with Mo- and Nb-films on Si than with Pd- and Pt-films on Si substrates [(14-17)]. Furthermore, the observation that W is nearly constant in the present Pt-Si system may not be as good an approximation in other systems. Since the composition of the surface layer is changing during sputtering, the ion range and the effectiveness of the ion-induced atomic mixing can have corresponding variations. The fact that Si was used as the diluted alloying element in Pt could have simplified the problem because of the fact that Si is much lighter than Pt. The Pt atoms would then be responsible for triggering most of the collisions in the cascade. Therefore, the changing Si-concentration would not significantly affect the ion range and atomic mixing. This may have helped in maintaining the constancy of W.

6.6 Influences of Atomic Mixing and Preferential Sputtering on Depth Profiling Techniques

In the present work, the experiment started with a very thin layer of Si on top of a thick Pt-film. We first demonstrated that Si-atoms were spread out to a depth comparable to the ion range due to ion-induced atomic mixing. Some Si-atoms could then survive a prolonged

sputtering, because of the continuing atomic mixing process. Although this phenomenon has important implications in the sputter-depth-profiling techniques (as discussed in Section 6.5), the situations are generally different in the depth-profiling analyses. Usually, the impurity profiles extend over depths much greater than the range (or W) of the ion used for sputtering, as illustrated in Fig. 6.5(A). To see the effect of atomic mixing and preferential sputtering on depth-profiling, the model developed in Section 6.4 can be generalized to relate the apparent and the true impurity profiles.

Similar assumptions to those in Section 6.4 are made in this calculation, i.e., that the impurity atoms influenced by ion-induced atomic mixing are always redistributed very "quickly" and uniformly over an effective thickness W, and that the rate of sputter-removal of impurity atoms is proportional to the surface impurity concentration multiplied by a constant preferential sputtering parameter r. The conservation of impurity atoms then requires

$$W \frac{dN_{imp}(z)}{dt} = -J_{imp} + N^{0}_{imp}(z+W) \cdot \frac{dz}{dt} \qquad (6.8)$$

where z is the sputtered thickness, $N_{imp}(z)$ is the concentration of impurity atoms in the surface layer, J_{imp} is the magnitude of the flux of sputtered impurity atoms and $N^0_{imp}(z + W)$ is the concentration of the original (true) impurity distribution at

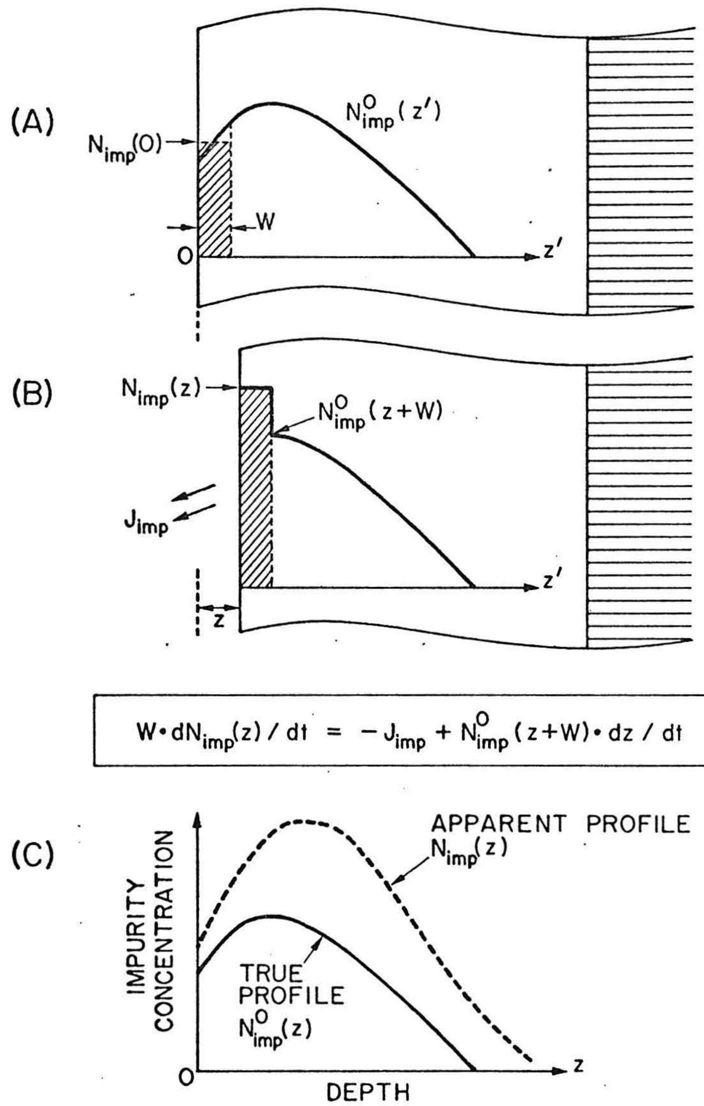

Figure 6.5 An illustration of the influence of atomic mixing and preferential sputtering on the sputter-depth-profiling analysis.

the depth of $z + W$ (See Fig. 6.5(B)). Since it is the surface concentration $N_{imp}(z)$ that is measured as a function of sputtered thickness z in the depth-profiling techniques, $N_{imp}(z)$ will become the measured (or "apparent") impurity depth profile (See Fig. 6.5(C)). Equation (6.8) is similar to Eq. (6.1) except for the term $N^0_{imp}(z + W) \cdot dz/dt$, which represents the supply of impurity atoms from the back-side of the surface layer due to the ion-induced atomic mixing effect. For simplicity, we consider first the cases of very low impurity concentrations, i.e., $x_0(z) \equiv N^0_{imp}(z)/N_0 << 1$. Equation (6.8) then becomes

$$W \frac{dx(z)}{dz} \cong -rx(z) + x_0(z+W) \tag{6.9}$$

where $x(z) \equiv N_{imp}(z)/N_0$. The relation $J_{imp} \cong rx(z)N_0 \frac{dz}{dt}$ has been used in obtaining Eq. (6.9). With constant r and W, Eq. (6.9) can be solved [18] to yield:

$$x(z) = \int_0^z e^{-r(z-z')/W} x_0(z'+W) \frac{dz'}{W} + e^{-rz/W} \frac{1}{W} \int_0^W x_0(z')\, dz' \tag{6.10}$$

Equation (6.10) relates the measured profile $x(z)$ to the true profile $x_0(z)$.

Equation (6.10) can be interpreted in physical terms. The

original true profit $x_0(z')$ can be considered as being composed of many infinitesimal sections each of thickness dz'. Equation (6.7) predicts that each infinitesimal section would generate an apparent profile of $\frac{x_0(z')dz}{W} e^{-r(z - z')/W}$ for $z > z'$. Therefore, the total apparent profile x(z) would be the superposition of contributions from all infinitesimal sections, i.e., $x(z) = \int_0^z e^{-r(z - z')/W} x_0(z')dz'/W$. However, this is still not the same as Eq. (6.10). The discrepancy is because of the assumption of the "very fast" atomic mixing over the thickness W. Consider, for example, the infinitesimal section at $z' = W^+$. As soon as this section gets in touch with the back-side of the surface layer, the atomic mixing effect will very quickly spread out all the impurity atoms in that infinitesimal section over the thickness W. Therefore, the infinitesimal section at $z'=W^+$ will contribute to x(z) as if it were at $z' = 0^+$. This accounts for $x_0(z' + W)$, instead of $x_0(z')$, in the first integral of Eq. (6.10). It also explains the necessity of the second integral in Eq. (6.10).

Equation (6.10) can be used to calculate the apparent profile x(z) for any given true profile $x_0(z)$. A few examples are shown in Figs. 6.6 and 6.7. Figure 6.6 illustrates the effect of preferential sputtering factor r, while Fig. 6.7 shows the influence of W on the depth-profiling analyses. For practical purposes, it is of interest to deduce $x_0(z)$ from known x(z), because $x_0(z)$ is the purpose of the measurement and x(z) is what is actually measured. With known x(z), Eq. (6.9) can be used to obtain $x_0(z)$ for $z > W$. However, it appears

impossible to know $x_0(z)$ for $0 < z < W$. Again, this is due to the "fast" atomic mixing process, which completely mixed up the surface layer before the measurements. Only the average value of the surface layer can be obtained, i.e., $x(0) = \frac{1}{W} \int_0^W x_0(z')dz'$. (See Fig. 6.5(A)).

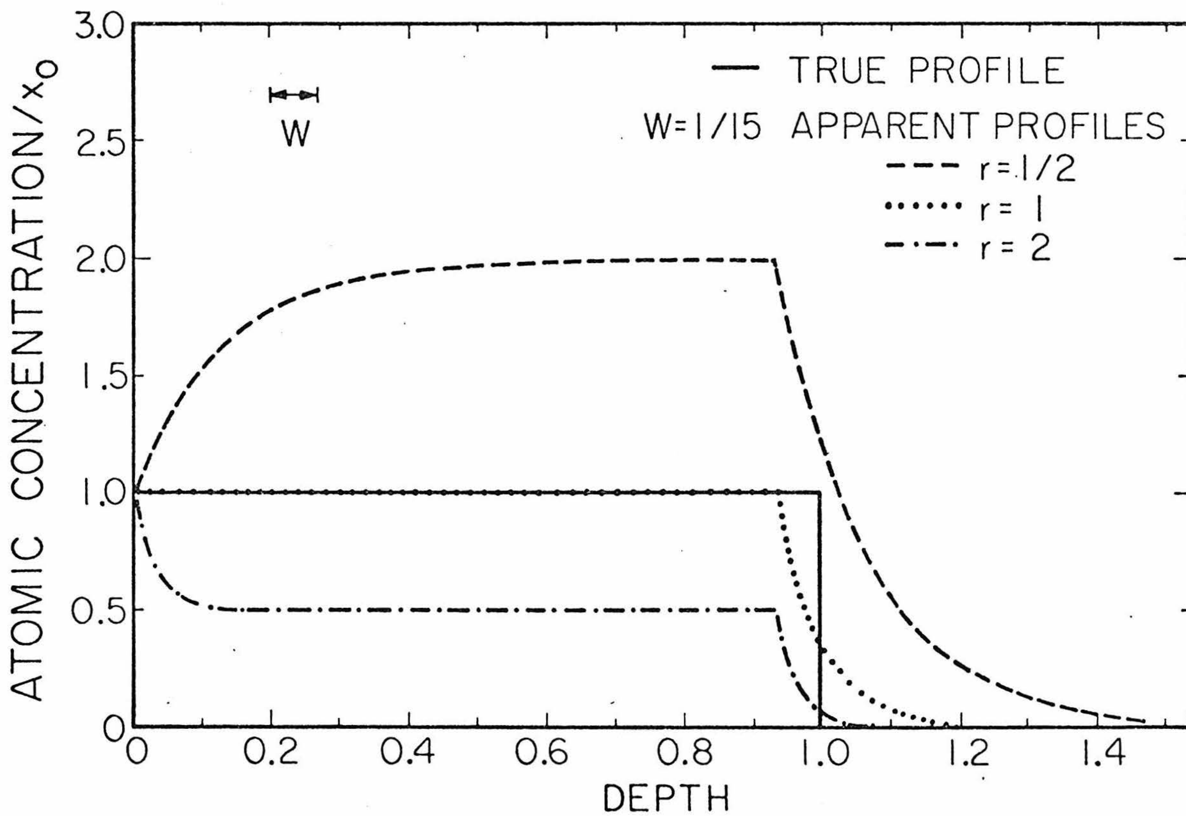

Figure 6.6 Calculated apparent profiles of a true profile of a square shape. With a constant W, the apparent profiles were calculated for various preferential sputtering conditions by using Eq. (10).

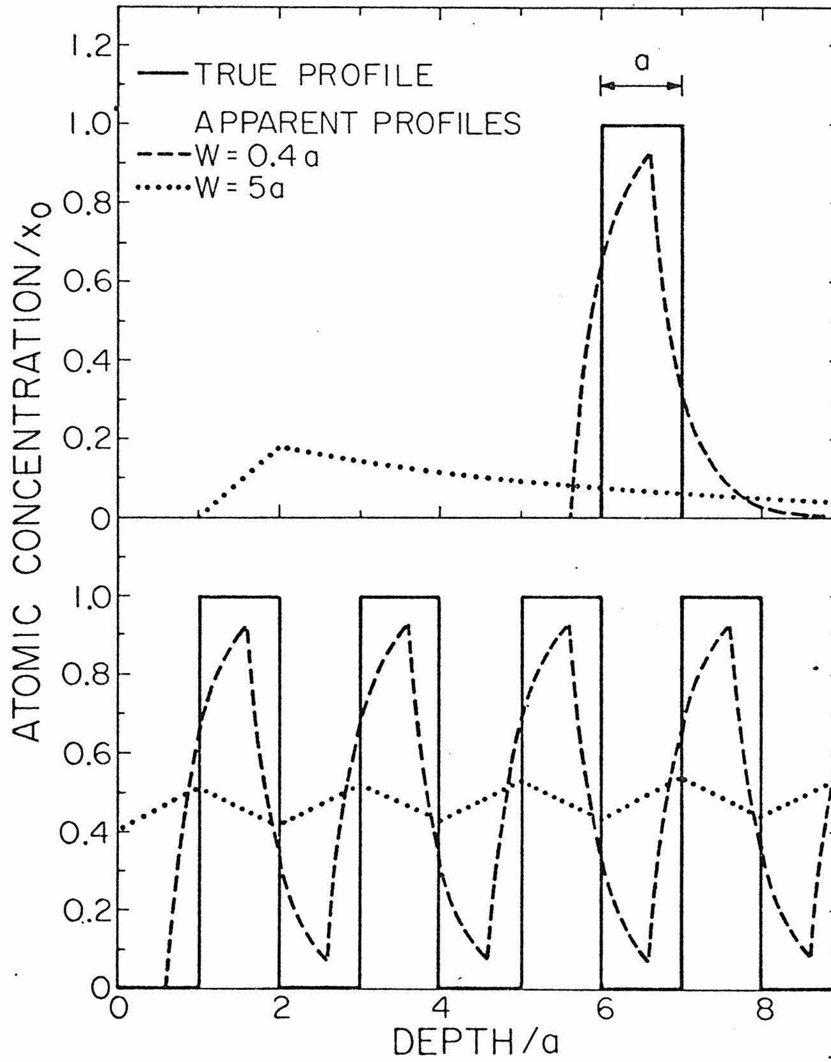

Figure 6.7 Further examples of calculated apparent profiles illustrating the effect of W in depth-profiling measurements. These calculations assumed no preferential sputtering (i.e., r = 1).

References

1. R. R. Hart, H. L. Dunlap and O. J. Marsh, J. Appl. Phys. 46, 277 (1975).

2. W. Wach and K. Wittmaack, Nucl. Inst. Meth. 149, 259 (1978).

3. J. A. McHugh, Rad. Eff., 21, 209 (1974).

4. F. Schulz, K. Wittmaack and J. Maul, Rad. Effects, 18, 211 (1973).

5. Z. L. Liau, J. W. Mayer, W. L. Brown and J. M. Poate, J. Appl. Phys. (in press).

6. J. M. Poate and T. C. Tisone, Appl. Phys. Lett. 24, 391 (1974).

7. C. Canali, C. Catellani, M. Prudenziati, W. H. Wadlin and C. A. Evans, Jr., Appl. Phys. Lett. 31, 43 (1977).

8. Z. L. Liau and J. W. Mayer, J. Vac. Sci. Tech. (in press).
   Z. L. Liau and J. W. Mayer, to be published in Treatise on Materials Science and Technology - Ion Implantation, J. K. Hirvonen, ed., (Academic Press, New York, 1978) Chap. 2.

9. B. Y. Tsaur, Z. L. Liau and J. W. Mayer, (to be published).

10. K. Wittmaack, paper presented at the 8th International Conference on X-Ray Optics and Microanalysis, Boston, Massachusetts, August, 1977.

11. P. S. Ho and J. E. Lewis, Surf. Sci. 55, 335 (1976).

12. K. Wittmaack and F. Schulz, Thin Solid Films (to be published).

13. J. K. Hirvonen, J. M. Poate, Z. L. Liau and J. W. Mayer Paper presented at the International Conference on Ion Beam Modification of Materials, Budapest, Hungary, September 1978.

14. W. F. van der Weg, D. Sigurd and J. W. Mayer, Applications of Ion Beams to Metals, S. T. Picraux, E. P. EerNisse and F. L. Vook, eds., (Plenum Press, New York, 1974) p. 209.

15. H. Nishi, T. Sakurai, T. Akamatsu and T. Furuya, Appl. Phys. Lett. 25, 337 (1974).

16. S. E. Matteson, J. Roth and M-A. Nicolet, paper presented at the International Conference on Ion Beam Modification of Materials, Budapest, Hungary, September, 1978.

17. B. Y. Tsaur, Z. L. Liau and J. W. Mayer, Appl. Phys. Lett. (to be published).

18. See, for example, F. B. Hildebrand, Advanced Calculus for Applications (Prentice-Hall, New York, 1962) Chap. 1.

Chapter 7

FURTHER EXPERIMENTS AND CONCLUSION

7.1 Introduction

While this thesis research has come to a finishing stage, more interesting progress in this area is taking place at this moment. This is due to collaboration among my colleagues, B. Y. Tsaur, J. W. Mayer and myself.

We first investigated the interfacial silicide formation due to ion-induced atomic mixing using various ion species and metal-silicon combinations. Then, with special sample configurations, the depth-dependence of the atomic mixing effect was experimentally measured. We also observed an interesting phenomenon that the implanted inert gas atoms tend to aggregate to the metal-silicon interface and form gas bubbles there. Finally, combined with post thermal annealing, new Si-rich metal-silicide phases were produced by using ion-induced atomic mixing.

7.2 Ion-Induced Silicide Formation

In Chapter 2, an ion-induced atomic mixing effect was invoked to explain the observed thicknesses of the altered surface layers in the sputtered alloys and compounds. This effect was further demonstrated in Chapter 5, where we first showed the mixing of discrete surface layers over the ion range. Then, the evolution of the mixed layers during sputter-etching was also explained by the same atomic mixing

effect.

Perhaps one of the most interesting and earliest demonstrations of atomic mixing is "ion-induced interfacial reactions" [1,2]. When an incident ion penetrates through an interface between a thin film (of species A) and a substrate (of species B), ion-induced atomic mixing may result in an intermixed region (which contains both A and B) near the interface. This intermixed region may contain definite compound phases. Therefore, it can be called an ion-induced interfacial reaction.

Such a phenomenon was first observed experimentally for samples with Pd-films deposited on Si substrates [1]. Briefly, Pd-Si intermixed regions (of several hundred angstroms thick) were observed after the samples had been bombarded by Ar ions of 40-400 keV to doses of $\sim 10^{16} cm^{-2}$ at room temperature. Experiments were carried out to rule out the possibility of temperature rise (due to ion bombardment) as the origin of mixing. Furthermore, the effect was observed only when the ion range was long enough to reach the Pd-Si interface. Because the number of atoms in the intermixed region was an order of magnitude greater than that of the Ar dose, it seems that the effect could not be fully accounted for by recoil implantation.

Similar experiments were then carried out for Pt [2,3], Mo [4] and Nb [5] films on Si substrates. Intermixing effects very similar to those found in Pd-films were observed for Pt films, but not for Nb and Mo films bombarded at room temperature. Since Pd and Pt form silicides at much lower temperatures than Mo or Nb [6], these results

seem to suggest that atomic mixing depends not only on ion bombardment, but also on some intrinsic diffusion properties of the target material. We recently observed that, with heavy ions (Xe^+), intermixing of Pt and Si occurred for ion doses lower than $10^{14}cm^{-2}$. This suggests that the effect is related to the density of collisions in the cascade.

Theoretical considerations have been given to relate the interfacial diffusion to the nuclear stopping power of the incident ion[7,8]. In an attempt to understand the kinetics of the interfacial reaction, we conjectured that the process might be composed of many "localized" elemental processes each triggered by one incident ion. This is illustrated in Fig. 7.1. The size of each reacted region (Fig.7.1a) would depend on both the intrinsic diffusion property of the material and the collision cascade. As more and more ions come in, the reacted regions tend to cover the whole interface and some of them begin to overlap (Fig. 7.1b). In the overlapped region, the reaction would be promoted further. At high ion doses, the reacted layer becomes thicker (Fig.7.1c). Because of the statistical nature of ion incidences, there would be some roughness in the reaction front. Under idealized conditions, the kinetics can be described by Poisson statistics.

If this picture is correct, and if the thickness of the reacted regions (ℓ in Fig. 7.1(a)) is sufficiently large, one should be able to measure ℓ and σ by using Rutherford backscattering. The preliminary result showed that with 300 keV Xe^+ on the Pt/Si system, σ was larger

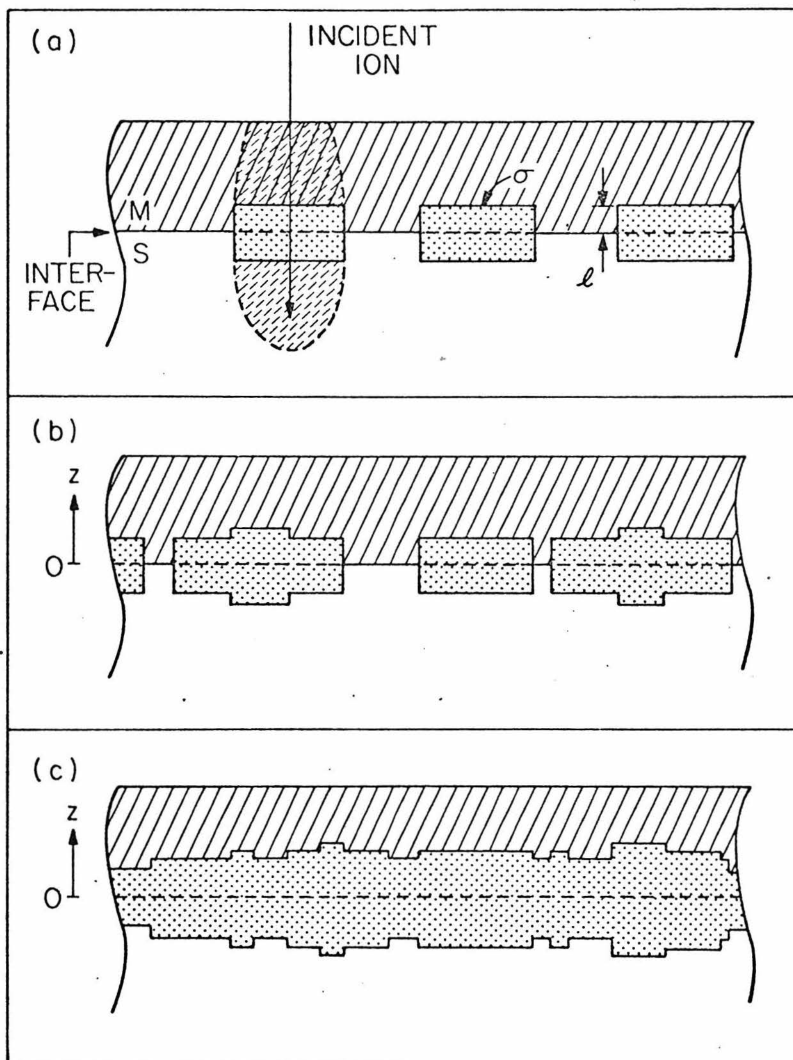

Figure 7.1 A simple model for the kinetics of ion-induced interfacial reactions. Each incident heavy ion initiates a collision cascade in a volume surrounding the ion track (Fig.7.1(a)). There is some atomic mobility within that volume for a short period of time, which then results in an intermixed region near the interface. Thus, the interfacial reaction is considered as being composed of many localized elemental processes. Under prolonged bombardment, there is overlap of the localized regions (b) and for higher doses a continuous layer is formed (c).

than 10^4 Å^2, and ℓ was no greater than 40 Å. It seems that ℓ is so small that it cannot be easily measured with the present technique.

Experiments [3] with Pt-, Ni- and Hf-films (100-400 Å) bombarded with rare-gases (Xe^+, Kr^+, Ar^+ and Ne^+) of 100-300 keV showed phenomena similar to that shown in Fig. 7.1(c). Both Rutherford backscattering and glancing angle x-ray diffraction showed phase formations in the intermixed layers. For Pt on Si, $1 \times 10^{14} cm^{-2}$ of 300 keV Xe^+ resulted in a Pt_2Si layer of ~200 Å near the interface. The average thickness of the Pt_2Si layer was proportional to the square root of Xe^+-dose. Similar square-root dependences were found for other ions. Heavier ions showed higher efficiency in causing atomic mixing. For 300 keV Ar^+, a dose of ~10 times that of 300 keV Xe^+ was required to produce the same amount of Pt_2Si formation. This suggests that ion-induced atomic mixing is related to the density of collision cascade. This is consistent with the observation that, with identical 300 keV Xe^+ implantations, less Ni_2Si than Pt_2Si formation was observed. Because Ni is much lighter than Pt, the collision cascade in Ni should be less dense than that in Pt. On the other hand, Hf has an atomic mass close to that of Pt (less than 10% difference) but showed lower intermixing rate than Pt, under identical implantation conditions. Since the silicide formation temperature of Hf (550-700°C for HfSi) is higher than that of Pt (200-500°C for Pt_2Si) [6], one concludes that the amount of atomic mixing is also related to the intrinsic diffusion property of the materials. This is consistent

than 10^4 Å^2, and ℓ was no greater than 40 Å. It seems that ℓ is so small that it cannot be easily measured with the present technique.

Experiments [3] with Pt-, Ni- and Hf-films (100-400 Å) bombarded with rare-gases (Xe^+, Kr^+, Ar^+ and Ne^+) of 100-300 keV showed phenomena similar to that shown in Fig. 7.1(c). Both Rutherford backscattering and glancing angle x-ray diffraction showed phase formations in the intermixed layers. For Pt on Si, $1 \times 10^{14} cm^{-2}$ of 300 keV Xe^+ resulted in a Pt_2Si layer of ~200 Å near the interface. The average thickness of the Pt_2Si layer was proportional to the square root of Xe^+-dose. Similar square-root dependences were found for other ions. Heavier ions showed higher efficiency in causing atomic mixing. For 300 keV Ar^+, a dose of ~10 times that of 300 keV Xe^+ was required to produce the same amount of Pt_2Si formation. This suggests that ion-induced atomic mixing is related to the density of collision cascade. This is consistent with the observation that, with identical 300 keV Xe^+ implantations, less Ni_2Si than Pt_2Si formation was observed. Because Ni is much lighter than Pt, the collision cascade in Ni should be less dense than that in Pt. On the other hand, Hf has an atomic mass close to that of Pt (less than 10% difference) but showed lower intermixing rate than Pt, under identical implantation conditions. Since the silicide formation temperature of Hf (550-700°C for HfSi) is higher than that of Pt (200-500°C for Pt_2Si) [6], one concludes that the amount of atomic mixing is also related to the intrinsic diffusion property of the materials. This is consistent

with earlier observations on Mo-Si [4] and Nb-Si [5] systems. Similar phenomena were also observed in other systems such as Pd-Si, Cr-Si and V-Si.

7.3 Depth-Dependence of Ion-Induced Atomic Mixing

There have been ample experimental evidences which show that ion-induced atomic mixing occurs only within a depth comparable to the ion range. An example has been shown in Fig. 6.2, where complete mixing of the surface layer was observed with the underlying Pt/Si interface undisturbed. A measurement of the depth-dependence of ion-induced atomic mixing may also provide insights into the mixing mechanism.

For this purpose, we prepared samples of ~1000 Å amorphous Si with very thin layers (~30 Å) of Pt buried at various depths (only one Pt layer in each sample). After being implanted under identical conditions, these samples were analyzed by backscattering techniques. The spreading of Pt-atoms was observed to be dependent upon the depth of the original thin Pt-layer. The depth dependence seemed to follow a similar trend as the demage profile. For example, with 300 Å Xe^+, the width of Pt-spreading was nearly constant down to a depth of ~800 Å and then it dropped down almost linearly to zero at a depth of ~2400 Å. The implanted Xe-profile was close to a Gaussian distribution with a peak position at 1300 Å and a FWHM of 1200 Å.

The similarity between the depth-dependence of atomic mixing and demage profile seems to be consistent with the observation (Section 7.2) that ion-induced atomic mixing was related to the density of

cascade. This result may prove useful in further applications of ion-induced atomic mixing. This type of experiment may also provide further understanding of the mechanism of ion-induced atomic mixing. For example, one can do the implantations on heated samples and see how the depth-dependence of atomic mixing varies with temperature.

7.4 Gas Bubble Formation at Interfaces

In Section 3.4, we reported experimental observations of Ar-bubbles in the sputtering of PtSi. We argued that, if the implanted rare-gas atoms condense to form large bubbles, the backscattering signal of the implanted species will be substantially sharpened up, because dE/dx (for $^4He^+$ to travel through) in the gas atmosphere is much smaller than that in the solid (Fig. 3.15). In recent experiments for ion-induced atomic mixing, we also observed sharp peaks in the implanted Xe-distributions.

These observations show other interesting features. First, the position of the sharp peak correlated very well with the position of the interface between the surface layer and the Si-substrate, indicating that the interface is a favorite site for gas atoms. This correlation was observed regardless of the variations of incident ion energy and the thickness of the surface layer (so long as the ions could penetrate through the interface). Furthermore, this phenomenon was found to be general for various thin-film systems and rare gases.

There were also other evidences of bubble formation at the interface. For increasing Xe^+-dose on 500 Å V on Si, almost the whole

surface layer disappeared suddenly after a Xe^+-dose of $4x10^{16}cm^{-2}$. We interpret this as a sudden peeling-off of the layer because of either the high pressures in the bubbles or the large number of bubbles that tend to cover a major portion of the interfacial area. Cross-sectional TEM study has also shown evidence of bubbles at the interfaces.

It has been inferred that implanted gas atoms form bubbles that prefer to nucleate at dislocation lines. The present case of bubble formation at the interface is probably due to a similar reason. However, we still do not know why the interface is a favorite site for gas atoms.

7.5 Formation of Metastable Phases Using Ion-Implantation and Post Thermal Annealing

In Section 7.2, we mentioned ion-induced silicide formation at metal-silicon interface, for ion-doses of 10^{14}-$10^{15}cm^{-2}$. Higher ion doses resulted in more incorporation of Si into the surface layer. Si-contents higher than $\sim PtSi_2$ was obtained for doses of $\sim 10^{16}cm^{-2}$. This is of interest, because the most Si-rich Pt-silicide phase that can be obtained by using thermal annealing has been PtSi [6,9]. However, x-ray analysis showed no structure (likely amorphous) in these Si-rich surface layers produced by ion-induced atomic mixing. Annealing of these samples at 500^oC for 20 min. resulted in formation of phases which could not be identified with known Pt-Si phases [6,9] or polycrystalline Si precipitation.

Backscattering data showed that the first phase corresponded to a

composition of ~Pt_2Si_3. For higher Si-content, a second phase (close to Pt_3Si_7) began to form. When the two phases coexisted, they formed distinctive layers as indicated by well-defined steps in backscattering spectra.

Isochronal thermal annealing (for 15 min.) showed that the first phase began to form at ~$400^{o}C$. For temperatures higher than ~$550^{o}C$, the phase began to decompose and the surface layer became a mixture of PtSi and polycrystalline-Si precipates. This indicates that the phase is metastable.

These results suggest a potential method of forming new materials of interesting physcal properties. For example, it may produce a series of metastable silicides which may show interesting electrical properties such as Schottky barrier heights and superconductivity. There are also possibilities of forming metastable metal-metal alloys.

To promote the applicability of the atomic mixing effect, we further proposed several techniques. First, multi-layers can be used to lower the required ion doses. The idea is to prepare a periodic structure of very thin layers of the requisite elements and to ion-mix the structure. The relative thicknesses of the alternative layers should be adjusted for the desired composition, while the total thickness of the structure should be designed in accordance with the ion species and energy. The advantage is that the ion-mixing will not have to transfer atoms for "long" distances to achieve the mixing of a thick layer. Therefore, according to the results described in Section 7.2, one can lower the required ion dose more than one order

of magnitude. Of course, the precise ion dose will depend on the thicknesses of the thin layers. Thus, the present technique is to first mix the system to a great extent using conventional methods (i.e., thin-film deposition techniques) and then to use ion beam to just promote the mixing to an atomic scale. Parallel to the lower required ion-doses, this technique has other appealing features. For example, it may prove useful for those systems which have been more "difficult" for atomic mixing (e.g., Nb-Si and Mo-Si as mentioned in Section 7.2). Similarly, it also offers the possibility of using lighter ions which were shown to be less efficient for mixing. (The availability of light ions, such as the use of Si-ions to mix the metal-Si systems, can eliminate the possible impurity effects due to the implantation of the foreign species, such as Xe.) Furthermore, it also provides a better chance of obtaining a thick mixed layer of a uniform composition.

Besides the multi-layer technique, there are other alternatives such as using co-deposition of requisite elements using electron-gun evaporation. There are questions concerning the similarity between an ion-mixed layer and a layer prepared by co-deposition and the possibility of obtaining the metastable phases from the co-deposited samples.

7.6 Conclusion

In this work, we first investigated the sputter-induced surface-

layer composition changes in binary alloys and compounds. We found that this phenomenon is a quite general one. Two rules seem to apply to all cases: First, the heavier components become enriched in the surface; second, the composition changes extend to depths comparable to the ion range. Although qualitative ideas and phenomenological models have been proposed to explain the phenomena, a theory based on atomic collisions has not been worked out to make quantitative predictions.

On the other hand, the ideas obtained from these studies (i.e., preferential sputtering at surface and atomic mixing over the ion range) have proven useful in other related experiments. The phenomenological model has been generalized to describe the high-dose ion-implantation phenomena and to describe the evolution of surface layers during sputter-etching. Preliminary experimental results showed good agreement with the predictions. The model has also been used to predict the effect of atomic mixing and preferential sputtering in sputter-depth-profiling techniques. We obtained a simple equation which related the apparent and true impurity profiles.

Finally, the ion-induced atomic mixing effect has shown its capability of producing thin-film materials of desirable compositions, especially metastable alloys unachievable by conventional metallurgical means. More work is being conducted in this promising area.

References

1. W. F. van der Weg, D. Sigurd and J. W. Mayer, in Applications of Ion Beams to Metals, S. T. Picraux, E. P. EerNisse and F. L. Vook, eds., (Plenum Press, New York, 1974) p. 209.
2. J. M. Poate and T. C. Tisone, Appl. Phys. Lett. 24, 391 (1974).
3. B. Y. Tsaur, Z. L. Liau and J. W. Mayer, Appl. Phys. Lett. (to be published).
4. H. Nishi, T. Sakurai, T. Akamatsu and T. Furuya, Appl. Phys. Lett. 25, 337 (1974).
5. S. E. Mattesion, J. Roth and M-A. Nicolet, paper presented at International Conference on Ion-beam Materials Modification, Budapest, September 1978.
6. K. N. Tu and J. W. Mayer, in Thin Films-Interdiffusions and Reactions, J. M. Poate, J. W. Mayer and K. N. Tu, eds., (Wiley, New York, 1978).
7. T. Ishitani and R. Shimizu, Appl. Phys. 6, 241 (1975).
8. P. K. Haff and Z. E. Switkowski, J. Appl. Phys. 48, 3383 (1977).
9. M. Hansen, Constitution of Binary Alloys, 2nd ed. (McGraw-Hill, New York, 1958).

APPENDIX A. DERIVATION OF THE EQUATION FOR g(t)

Equation (4.19) gives

$$n(0,t) = \int_0^t g(t') \frac{e^{-\frac{v^2}{4D}(t-t')}}{2\sqrt{\pi D(t-t')}} dt' \tag{A-1}$$

$$= \int_0^t g(t-u) \frac{e^{-\frac{v^2}{4D}u}}{2\sqrt{\pi D u}} du$$

where $u \equiv t-t'$

Therefore,

$$\frac{d}{dt} n(0,t) = \lim_{\varepsilon \to 0} \frac{n(0,t+\varepsilon) - n(0,t)}{\varepsilon}$$

$$= \lim_{\varepsilon \to 0} \frac{1}{\varepsilon}\left[\int_0^t g(t-u+\varepsilon) \frac{e^{-\frac{v^2}{4D}u}}{2\sqrt{\pi D u}} du + \int_t^{t+\varepsilon} g(t-u+\varepsilon) \frac{e^{-\frac{v^2}{4D}u}}{2\sqrt{\pi D u}} du - \int_0^t g(t-u) \frac{e^{-\frac{v^2}{4D}u}}{2\sqrt{\pi D u}} du \right]$$

$$= \lim_{\varepsilon \to 0} \int_0^t \frac{g(t-u+\varepsilon) - g(t-u)}{\varepsilon} \frac{e^{-\frac{v^2}{4D}u}}{2\sqrt{\pi D u}} du + g(0) \frac{e^{-\frac{v^2}{4D}t}}{2\sqrt{\pi D t}}$$

$$= \int_0^t g'(t') \frac{e^{-\frac{v^2}{4D}(t-t')}}{2\sqrt{\pi D(t-t')}} dt' + g(0) \frac{e^{-\frac{v^2}{4D}t}}{2\sqrt{\pi D t}} \tag{A-2}$$

On the other hand, Eq. (4.19) also gives

$$\frac{\partial}{\partial x} n(x,t) = \int_0^t g(t') \frac{-[x+v(t-t')]}{2D(t-t')} \frac{e^{-[x+v(t-t')]^2/4D(t-t')}}{2\sqrt{\pi D(t-t')}} dt'$$

$$= -\frac{v}{2D} n(x,t) - \frac{e^{-\frac{v}{2D}x}}{2\sqrt{\pi} D} \int_{x/\sqrt{Dt}}^{\infty} g(t - \frac{x^2}{Dq^2}) \, e^{-q^2/4} \, e^{-v^2x^2/4D^2q^2} \, dq$$

where $q \equiv x/\sqrt{\pi D(t-t')}$. Therefore,

$$\left.\frac{\partial}{\partial x} n(x,t)\right|_{x=0^+} = -\frac{v}{2D} n(0,t) - \lim_{x\to 0} \frac{e^{-\frac{v}{2D}x}}{2\sqrt{\pi} D} \int_{x/\sqrt{Dt}}^{\infty} g(t - \frac{x^2}{Dq^2}) \, e^{-q^2/4} \, e^{-v^2x^2/4D^2q^2} \, dq$$

$$= -\frac{v}{2D} n(0,t) - \frac{1}{2\sqrt{\pi} D} g(t) \int_0^{\infty} e^{-q^2/4} \, dq$$

The definite integral can be evaluated to yield $\sqrt{\pi}$. Hence,

$$\left.\frac{\partial}{\partial x} n(x,t)\right|_{x=0^+} = -\frac{v}{2D} n(0,t) - \frac{1}{2D} g(t) \qquad \text{(A-3)}$$

Substituting Eq. (A-1), (A-2) and (A-3) into the boundary condition (Eq. (4.9b)), the equation for g(t) (i.e., Eq. (4.20)) is obtained.

APPENDIX B. SOLUTION OF EQ. (4.20) FOR g(t)

The Laplace transform of Eq. (4.20) gives

$$\mathcal{L}\{g'(t)+Rg(t)\}\,\mathcal{L}\left\{\frac{e^{-\frac{V^2}{4D}t}}{2\sqrt{\pi D t}}\right\}+\frac{A}{2D}\mathcal{L}\{g(t)\} = g(0)\mathcal{L}\left\{\frac{e^{-\frac{V^2}{4D}t}}{2\sqrt{\pi D t}}\right\}+\frac{C}{s} \qquad \text{(B-1)}$$

where the convolution theorem and $\mathcal{L}\{1\}=\int_0^\infty e^{-st}dt = \frac{1}{s}$

have been applied [8]. To simplify Eq. (B-1), the following relations are used.

$$\mathcal{L}\{g'(t)\} = s\cdot\mathcal{L}\{g(t)\} - g(0) \qquad \text{(B-2)}$$

$$\mathcal{L}\{g'(t)\} = \frac{1}{\sqrt{D}}\frac{1}{\sqrt{s+\frac{V^2}{4D}}} \qquad \text{(B-3)}$$

Equation (B-2) is a general theorem of Laplace transform [8]. Equation (B-3) is available in mathematical tables [9].

Using Eqs. (B-2) and (B-3), Eq. (B-1) gives, after some re-arrangement

$$\mathcal{L}\{g(t)\} = \frac{C\sqrt{D}\sqrt{s+\frac{V^2}{4D}}}{s\left(s+R+\frac{A}{\sqrt{D}}\sqrt{s+\frac{V^2}{4D}}\right)} \qquad \text{(B-4)}$$

This is the Laplace transform of g(t). To solve for g(t), the inverse transform must be carried out. For this purpose, the fraction in Eq. (B-4) is re-arranged:

$$\mathcal{L}\{g(t)\} = \frac{P\sqrt{s+\frac{v^2}{4D}}}{s} + \frac{Q}{s} + \frac{K_1}{\sqrt{s+\frac{v^2}{4D}} + \alpha_1} + \frac{K_2}{\sqrt{s+\frac{v^2}{4D}} + \alpha_2} \qquad \text{(B-4a)}$$

where $P \equiv \frac{2r}{r+1} n_0\sqrt{D}$, $Q \equiv -\frac{n_0 v}{(r+1)}$,

$K_1 \equiv \frac{n_0 v}{(r+1)\alpha_1} A_1$, $K_2 \equiv \frac{n_0 v}{(r+1)\alpha_2} A_2$,

and α_1, α_2, A_1 and A_2 are defined as in the text.

The inverse Laplace transform of each term on the righthand side of Eq. (B-4a) can be carried out using the following relation [9]:

$$\mathcal{L}^{-1}\left\{\frac{\sqrt{s+(v^2/4D)}}{s}\right\} = \frac{e^{-\frac{v^2}{4D}t}}{\sqrt{\pi t}} + \sqrt{\frac{v^2}{4D}}\,\mathrm{erf}\sqrt{\frac{v^2 t}{4D}}$$

$$\mathcal{L}^{-1}\left\{\frac{1}{\sqrt{s+\frac{v^2}{4D}} + \alpha}\right\} = e^{-\frac{v^2}{4D}t}\left(-\frac{1}{\sqrt{\pi t}} - \alpha e^{\alpha^2 t}\,\mathrm{erfc}\sqrt{\alpha^2 t}\right)$$

and $\mathcal{L}^{-1}\left\{\frac{1}{s}\right\} = 1$. A solution for g(t) is thus obtained:

$$g(t) = \frac{n_0 v}{r+1}\left[r\cdot\mathrm{erf}\sqrt{\frac{v^2 t}{4D}} - 1 - e^{-\frac{v^2 t}{4D}}\left(A_1 e^{\alpha_1 t}\,\mathrm{erfc}\sqrt{\alpha_1 t} + A_2 e^{\alpha_2 t}\,\mathrm{erfc}\sqrt{\alpha_2 t}\right)\right]$$

This is Eq. (4.21) as given in the text.